Cellular Automaton and Markov Chains: A Study of Earthquake Dynamics

by

Edouard Kravchinsky

A thesis submitted in partial fulfillment of the requirements for the degree of

Master of Science

in

Geophysics

Department of Physics
University of Alberta

Abstract

Many models exist to study earthquake fault systems to gain a fundamental understanding of the dynamic processes that occur during an earthquake. We study cellular automata (CA) models to replicate a simple earthquake fault model. We find that the dynamics of a CA model can be simplified to a statistical Markov process. This offers a new insight into how an earthquake sequence may develop and suggests that some underlying processes are more probable than others. We compare the Markov model to the CA model and find that they are in good agreement. Lastly, we implement heterogeneities into the CA model as varied structures which complicate model dynamics. We find heterogeneities generate swarm events and temporal clustering visible within their time series. Therefore, the overall shape and slope of the frequency-size relation is modified. This suggests that scaling depends on the underlying spatial distribution of heterogeneities. A fundamental understanding of the basic processes can help predict the behavior of more complex mixed systems, which is the ultimate goal of this project.

Acknowledgments

First and foremost, I would like to thank my supervisor, Dr. Mirko van der Baan, without whom this thesis would not be possible. The subject matter and the pursuit of answering the question why has made this research project very unique and interesting. I would also like to thank Javad Kazemian for providing the first version of the cellular automaton source code which has helped jump start the project. As well, I am very grateful of my colleagues in our research group and the Microseismic Industry Consortium for their advice and valuable suggestions. Additionally, I wish to acknowledge my committee members for providing valuable feedback during my thesis research. Finally, I would like to thank my family and friends for their never-ending support and encouragement.

Contents

1 Introduction **1**

1.1 Motivation and contribution 1

1.1.1 Questions to answer 2

1.2 Thesis structure 2

2 Background **4**

2.1 Introduction 4

2.2 Universal Scaling Law 5

2.3 Earthquake Fault Models 6

2.3.1 Burridge-Knopoff (BK) Model 6

2.3.2 Chain-reaction Source Model 10

2.3.3 Rundle, Jackson and Brown (RJB) Model 11

2.3.4 Olami, Feder and Christensen (OFC) Model 14

2.4 The BK, RJB and OFC models 16

2.5 Model Ingredients 18

2.6 Modern Model Variations 19

3 Cellular Automaton Theory **24**

3.1 Cellular Automaton 24

3.1.1 Homogeneous Model 24

3.1.2 Inhomogeneous Model 29

3.1.3 Plate update time and physical time 32

3.1.4 Hexagonal grid versus square grid 34
3.1.5 Back-of-the-envelope Calculations 35
3.1.6 Fractal dimension 38

4 Markov Chain Theory 39

4.1 Predictive Model 39
4.1.1 Building a Transition Matrix 39
4.1.2 Markov Chain 43
4.1.3 Absorbing Markov Chain 45
4.2 Application of Markov Chains 46
4.2.1 Example 47
4.3 Frequency-Size Probability Distribution 50
4.3.1 Predicting Homogeneous Models 50
4.3.2 Predicting Mixed Models 52
4.4 Markov Chain Monte Carlo 54

5 Cellular Automaton Homogeneous Results 57

5.1 Homogeneous Model 57
5.1.1 Time Series 58
5.1.2 Frequency-Size Distribution 59
5.2 System details 63
5.2.1 Internal Stress Distribution 63
5.2.2 Avalanche Sequences 66
5.2.3 Model Expectancies 70

6 Markov Chain Results 73

6.1 Transition Matrices 73
6.2 Markov Chain Monte Carlo 74
6.2.1 Time Series 74
6.2.2 Frequency-Size Distribution 77

6.2.3 Avalanche Sequences 80

7 Cellular Automaton Inhomogeneous Results 83
7.1 Inhomogeneous Block Models 84
7.1.1 Time Series 85
7.1.2 Frequency-Size Distribution 87
7.2 System details 91
7.2.1 Internal Stress Distribution 91
7.2.2 Avalanche Sequences 92
7.2.3 Model Expectancies 99
7.3 Inhomogeneous Structure Models 102
7.3.1 Time Series 103
7.3.2 Frequency-Size Distribution 105
7.4 System details 107
7.4.1 Internal Stress Distribution 108
7.4.2 Avalanche Sequences 110
7.4.3 Model Expectancies 115

8 Discussion 118
8.1 Homogeneous Models 118
8.1.1 Cellular Automaton 118
8.1.2 Markov chain Monte Carlo 121
8.2 Inhomogeneous Models 122
8.2.1 Block Models 123
8.2.2 Role of structure 124
8.2.3 Low noise and asperities 127

9 Conclusion 129
9.1 Conclusions 129
9.2 Suggested future research 131

List of Tables

5.1 Plate update and physical time for homogeneous CA models . . 60
5.2 Cumulative number of individual cell failures for homogeneous CA models 72

6.1 Plate update and physical time for homogeneous MCMC models 77

7.1 Plate update and physical time for inhomogeneous CA block models 87
7.2 Cumulative number of individual cell failures for inhomogeneous CA block models 99
7.3 Plate update and physical time for inhomogeneous CA structure models 104
7.4 Cumulative number of individual cell failures for inhomogeneous CA structure models 115

List of Figures

2.1 Burridge-Knopoff laboratory model 7
2.2 Burridge-Knopoff model potential energy as a function of time and frequency-energy diagram 8
2.3 Burridge-Knopoff numerical model 8
2.4 Burridge-Knopoff 2-D numerical model 10
2.5 Chain-reaction source model 11
2.6 Rundle and Brown macroscopic block 13
2.7 Olami, Feder and Christensen simulated results 16

3.1 An individual cellular automaton lattice cell 25
3.2 Hexagonal lattice grid 25
3.3 Flowchart Cellular Automaton 28
3.4 Lattice system basic dynamics 30
3.5 Inner plate update to plate update 31
3.6 Normal cell compared to an asperity cell 31
3.7 Plate update time to physical time 33
3.8 Physical time cutoff 33
3.9 Hexagonal grid and square grid 35
3.10 Conceptual model for total cell failures 37

4.1 A directed graph of Markov transition matrix 49
4.2 Absorbing Markov Chains Example 50
4.3 Absorbing Markov Chains Example 2 51

4.4 Flowchart Markov Chain Monte Carlo Algorithm 56

5.1 Physical time series for homogeneous CA models 59
5.2 Non-cumulative frequency-size for homogeneous CA models . . . 60
5.3 Interevent physical time for homogeneous CA models 62
5.4 Internal stress distribution snapshot for homogeneous CA models 64
5.5 Cumulative internal stress histogram for homogeneous CA models 65
5.6 Avalanche sequences for homogeneous CA models 68
5.7 Spatial distribution of avalanches for homogeneous CA models . 69
5.8 Correlation integrals of avalanche sequences for homogeneous CA models 71

6.1 Transition matrices for MC models 75
6.2 Physical time series from MCMC models 76
6.3 Non-cumulative frequency-size from MCMC models 78
6.4 Interevent physical time for MCMC models 79
6.5 Avalanche sequences for MCMC models 81

7.1 Inhomogeneous block model configurations 85
7.2 Physical time series for inhomogeneous CA block models 86
7.3 Non-cumulative frequency-size for inhomogeneous CA block models 89
7.4 Interevent physical time for inhomogeneous CA block models . . 90
7.5 Internal stress distribution snapshot for inhomogeneous CA block models 93
7.6 Cumulative internal stress histogram for inhomogeneous CA block models 94
7.7 Avalanche sequences for inhomogeneous CA block models 95
7.8 Spatial distribution of avalanches for inhomogeneous CA block models 97

7.9 Correlation integrals of avalanche sequences for inhomogeneous CA block models . . . 98
7.10 Cumulative number of failures for inhomogeneous CA block models 100
7.11 Inhomogeneous structure model configurations . . . 102
7.12 Physical time series for inhomogeneous CA structure models . . 104
7.13 Non-cumulative frequency-size for inhomogeneous CA structure models . . . 106
7.14 Interevent physical time for inhomogeneous CA structure models 107
7.15 Internal stress distribution snapshot for inhomogeneous CA structure models . . . 109
7.16 Cumulative internal stress histogram for inhomogeneous CA structure models . . . 110
7.17 Avalanche sequences for inhomogeneous CA structure models . . 112
7.18 Spatial distribution of avalanches for inhomogeneous CA structure models . . . 113
7.19 Correlation integrals of avalanche sequences for inhomogeneous CA structure models . . . 114
7.20 Cumulative number of failures for inhomogeneous CA structure models . . . 116

List of Abbreviations

CA	Cellular Automaton
GR	Gutenberg-Richter
SOC	Self-organized criticality
BK	Burridge and Knopoff
RJK	Rundle, Jackson and Brown
OFC	Olami, Feder and Christensen
MC	Markov Chain
MCMC	Markov Chain Monte Carlo

Chapter 1

Introduction

1.1 Motivation and contribution

This thesis aims to study earthquake dynamics through a numerical model that can help link qualitative features of earthquakes observed in nature to underlying governing physics. Studying the interconnected fields of cellular automata, self-organized criticality, and critical phenomena can greatly aid our understanding of complex processes such as earthquakes. A large body of information can be obtained from lattice models for earthquakes such as the universal Gutenberg-Richter scaling, the generation of foreshocks and aftershocks, and the effect of heterogeneous structures.

One of the main contributions of this thesis is the development of a predictive statistical model that captures the fundamental processes that occur within the cellular automaton earthquake fault model. This requires an in-depth analysis into how a cellular automaton evolves. We further contribute with a comprehensive analysis of the dynamics that originate from the implementation of heterogeneities. Beyond the numerical model, we discuss the implications of our results. These include the origin of spatiotemporal clustering within the time series, changes in the scaling of the frequency-size distributions, the dynamics of the internal stress distribution, how avalanche sequences develop and lastly the spatial clustering of events.

1.1.1 Questions to answer

The questions we aim to answer are as follows. 1) How are magnitude-frequency distributions influenced within a cellular automaton model? 2) When do swarms of events and spatial clustering occur? 3) Under what circumstances do we see classic foreshock-mainshock-aftershock sequences in the resulting time series? 4) What is the likelihood of small-scale failure leading to large magnitude seismicity? 5) What does the slip history look like for the largest events? 6) Can we predict, and therefore understand, the behavior of our model based on our initial parameters?

Answering these questions provides insight into the (un)predictability of small-scale events triggering larger magnitude seismicity, thus identifying diagnostic patterns for successful mitigation.

1.2 Thesis structure

This thesis is organized as follows. Chapter 2 reviews the background literature of the slider-block earthquake fault model. Thereafter, the purpose is to describe the transition from a Newtonian mechanics fault model into a simplified automaton fault model. Chapter 3 describes the theory of the cellular automaton model, the implementation of inhomogeneities and the relation between plate update time (simulation time) and physical time (time proxy). We briefly describe the implementation of the hexagonal grid within our model. A back-of-the-envelope model statistic is derived, along with a review on how to calculate the fractal dimension in order to study spatial correlations. Chapter 4 formulates a new proposed Markov model to statistically replicate the process of the cellular automaton model. We demonstrate how an analytical probability distribution can be calculated from the transition matrix for both homogeneous and inhomogeneous cellular automaton models. Lastly, we present a Markov chain Monte Carlo algorithm. Chapter 5 focuses on the examining the results of the homogeneous cellular automaton model, along with analyses of the internal system details. Chapter 6 provides the results of the alternative Markov model, and compares the results to the homogeneous cellular automaton model.

Chapter 7 is a in depth analyses of the results obtained from the inhomogeneous cellular automaton models. In particular, two distinct inhomogeneous models are studied: i) the inhomogeneous block model, and ii) the inhomogeneous structure model. These are compared to the proposed Markov model as well. Chapter 8 is an in-depth discussion of the results and their implications towards earthquake dynamics. Lastly, Chapter 9 summarizes the thesis and proposes some future work.

Chapter 2

Background

2.1 Introduction

The topic of industrial activity possibly inducing earthquakes remains an active research subject. It is unclear how greatly natural seismicity can be influenced by inhomogeneities and underlying structures. It is probable that the likelihood for induced seismicity depends on many formation conditions such as the in-situ stress, mechanical properties, treatment conditions and other heterogeneous reservoir factors (Warpinski et al., 2001). Modeling techniques exist that vary in their underlining physics and spatial scales. We employ the cellular automata (CA) model to study the effects of variously distributed inhomogeneities on a system with long range stress interaction with emphasis on fault network and system scales.

This discrete model is simple, yet capable of producing complex patterns also observed in earthquakes (Rundle and Klein, 1993). The proposed CA model is a self-organized criticality (SOC) many-body system that evolves towards an attractor in form of a critical point (Bak et al., 1987, 1988; Olami et al., 1992). The rationale behind this study is that the dynamic system exhibits behavior much like real earthquakes.

2.2 Universal Scaling Law

In seismology, the Gutenberg-Richter (GR) empirical law recognized that seismicity is statistically self-similar in a wide range of scales worldwide (Gutenberg and Richter, 1954). The Richter magnitude M_L, unitless, is a measure of the magnitude of an earthquake determined from the logarithm of the maximum amplitude recorded by a seismograph after accounting for amplitude attenuation due to the distance between the source (earthquake) to the receiver (seismograph) (Richter, 1935). This power law relation between earthquake magnitude and frequency is expressed as

$$log_{10} N_{M_L} = a - bM_L \tag{2.1}$$

or

$$N_{M_L} = 10^{a-bM_L}, \tag{2.2}$$

where N_{M_L} is the number of earthquakes having Richter magnitude greater or equal to M_L, and a and b are constants (Gutenberg and Richter, 1954). The a value indicates the total seismicity of the region, whereas the constant b is a measure of the proportions of large and small earthquakes. A larger b value will have a greater proportion of small earthquakes, whereas a smaller b value will have a lower proportion of small earthquakes. Generally, the constant $b \approx 1$ observed worldwide suggests self-similarity (Gutenberg and Richter, 1954), although variations in the b constant have been noted for shallow and deep earthquakes due to underlining stress regimes (Pacheco et al., 1992; Frohlich and Davis, 1993).

The use of the Richter magnitude M_L was replaced by the moment magnitude scale M_w as a more physically accurate method for describing the magnitude of events. The moment magnitude scale M_w, dimensionless, can be expressed in terms of the scalar seismic moment M_0, N·m, as

$$M_w = \frac{2}{3} log_{10}(M_0) - 10.7, \text{where } M_0 = \mu AD, \tag{2.3}$$

and μ is the shear modulus, A is the area of the fault rupture, and D is the average displacement (Kanamori, 1978). The moment magnitude M_w is magnitude scale that is converted from the scalar seismic moment M_0, where M_0 is a physical measure proportional to the total energy released in an earthquake. The seismic moment M_0 is obtained from observed seismograms once the effect of propagation, attenuation, and geometry of the fault are removed (Kanamori, 1978). Therefore, the moment magnitude M_w (Eq. 2.3) provides estimates of the earthquake size that is valid over a wider range of magnitudes, but in agreement with older previous magnitude scales such as the Richter magnitude M_L.

Combining Equations 2.2 and 2.3, the Gutenberg-Richter relation can be re-expressed as a power law proportional to the moment M_0 as

$$N_{M_0} \sim N_T M_0^{-2/3b}, \text{where } N_T = 10^a, \tag{2.4}$$

and N_{M_0} is the total number of events with a moment greater or equal to M_0, and N_T is the total seismicity of the region (Serino et al., 2011). The universal scaling relation of Equation 2.4 has been the study of various models, including the original spring-block model of Burridge and Knopoff (1967).

2.3 Earthquake Fault Models

2.3.1 Burridge-Knopoff (BK) Model

Studying earthquake fault models was introduced by Burridge and Knopoff (1967) and their laboratory experiments of earthquake sequences. Originally, the spring-block model consisted of a leading spring pulling a one-dimensional spring-block system that would produce a series of impulsive motion of varying magnitudes in between quiet intervals, as shown in Figure 2.1. The system consisted of blocks of equal mass m connected with identical springs K_c.

The displacement of every block after every event was recorded; thereafter using Hooke's law the potential energy released from all springs at each event was calculated. Given that the driving motor pulls at a constant velocity v, the rate of displacement from a reference point is proportional to time. This allowed for the system to be stopped after a shock to note the coordinates of all masses. Thus, the potential energy is expressed as a function of the coordinates

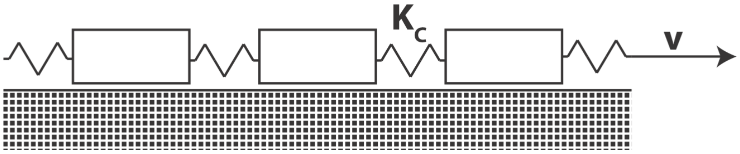

Figure 2.1: A schematic diagram of Burridge and Knopoff (1967) laboratory spring-block model. The front block is pulled at a constant velocity v on a rough surface, which effectively charges the system creating shocks of varying magnitudes in between quiet periods. All blocks have identical masses m and spring constants K_c.

of the system and not time.

The model demonstrated that small shocks would sometimes trigger a cascade of slippage that resulted in major shocks at a quasi-periodic occurrence. Furthermore, using the Gutenberg-Richter relation (Eq. 2.1) and the general energy-magnitude relation of

$$M = \alpha + \frac{2}{3} log_{10} E, \tag{2.5}$$

both equations combine to give

$$log_{10} N/N_0 \sim -\frac{2}{3} b \, log_{10} E, \tag{2.6}$$

where $log_{10} N/N_0$ is the logarithm of the number of shocks with potential energy release greater than E against the logarithm of E (Gutenberg and Richter, 1955; Burridge and Knopoff, 1967). The frequency-energy diagram exhibits a power-law distribution from the stick-slip behavior of the system, as shown in Figure 2.2.

To further examine the role of friction along a fault, the equations of motion and velocity-weakening friction law of the BK model were implemented into a numerical model. The equation of motions of the blocks of the generalized model is expressed as

$$m_i \ddot{x}_i = K_c(x_{i+1} - 2x_i - x_{i-1}) + K_L(x_i + vt) + f_i, \tag{2.7}$$

where m_i is the mass of the ith block, x is the displacement of the ith block, K_c the coupling spring constant, K_L the loading plate spring constant, v is the

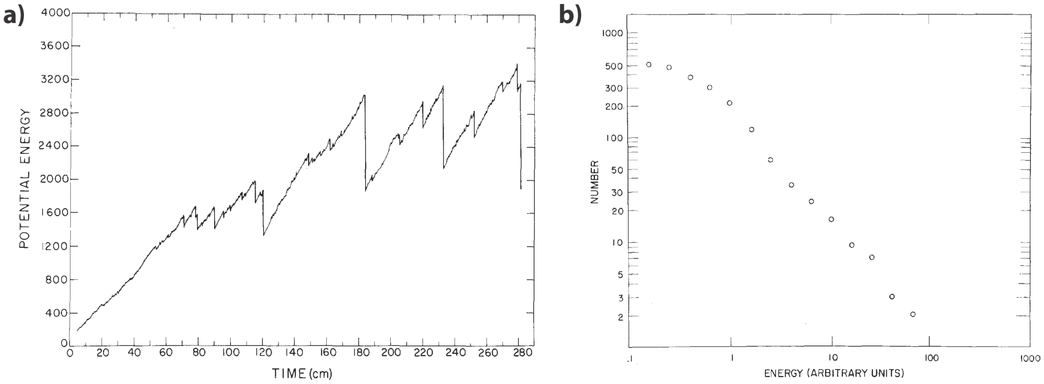

Figure 2.2: Burridge-Knopoff model results of potential energy as a function of time (left) and frequency-energy diagram (right) for their system with all springs equal. Modified Figures 4 and 5 of the BK model (Burridge and Knopoff, 1967).

loader plate constant velocity multiplied by a time t, and where f_i includes the frictional forces, radiative effects and viscosity for the ith block (Burridge and Knopoff, 1967). Typically, $K_L \ll K_c$ with a ratio of $K_L/K_c = 0.01$ used in the numerical simulations at slow loading velocities. The schematic diagram of the generalized BK model is shown in Figure 2.3.

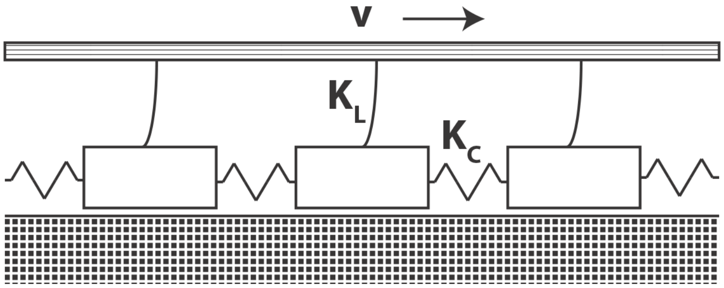

Figure 2.3: Schematic diagram of the BK numerical model (Burridge and Knopoff, 1967). A one-dimensional system of springs and blocks on a rough surface with a loader plate acting on all blocks via a loading spring K_L. All blocks are interconnected with identical spring constants K_c with the loading plate being pulled at a constant velocity v. The loader plate acts on every block of the system creating shocks of varying magnitudes in between quiet periods.

The nonlinear differential equations were numerically integrated using the Runge-Kutta procedure. The computed results showed a generalized process of the laboratory model described earlier, but allowed Burridge and Knopoff

(1967) to examine a more complex fault with a viscous region that acted as a time delay barrier to the transmission of the shock. The model statistics such as potential energy, total energy, block coordinates, velocities and accelerations were also computed. Lastly, Burridge and Knopoff (1967) results showed that the introduction of a time-delaying viscous region into the model produced the occurrence of aftershocks that take place following a major shock. The viscous region divided a group of blocks that form a chain analogous to a strongly seismic fault and a second group of blocks that represent a weaker seismic fault. The aftershock quake would correspond to the continuation of the mainshock motion through the viscous material to the other fault blocks.

Since then, many variations of the original BK model have been proposed to replicate the self-similarity in observed seismicity, along with other seismic phenomena such as spatiotemporal clustering, scaling of average slip and stress release, foreshock and aftershock sequences, heterogeneities of fault surface or a system of faults.

Carlson and Langer (1989) examined a deterministic one-dimensional spring-block system similar to the original BK model and observed complex and chaotic system behavior. The homogeneous model showed that it was capable of replicating the Gutenberg-Richter scaling law under nonlinear velocity-weakening friction. Carlson et al. (1991) further examined the BK model of a fault and highlight the distinction between smaller localized events and the larger delocalized events, where small events primarily smooth the system's elastic-energy density and larger events roughen it.

Nakanishi (1990, 1991) introduced a cellular automaton version of the BK model that simplifies the mechanical model into a simpler threshold based model, where slip occurs if the force on a block exceeds a predefined threshold. A cellular automaton is a simplified mathematical model used to investigate self-organization or an emerging pattern between blocks interactions (Wolfram, 1983). Only one block is allowed to move at any given time with all other blocks assumed to be stuck. Afterwards, part of the force of the slip is redistributed to the neighboring blocks that may iteratively slip in turn. This approach allows for a simulation of the numerical BK model to be less computationally intensive and allows to investigate a larger array of blocks. Nakanishi (1990, 1991) found similar results to those of Carlson and Langer (1989); although both models are completely homogeneous, they both exhibit spatial and temporally inhomogeneous behavior with a power-law distribution of event sizes.

2.3.2 Chain-reaction Source Model

Otsuka (1972b) was one of the first to propose a two-dimensional version of the BK model, as shown in Figure 2.4, where each block has four neighbouring blocks and slip or block motion occurs parallel to the direction of loading. Not only did this increase the number of elements, but it also allowed to simulate spatial slip patterns. The numerical simulation consisted of a total of 2000 blocks with 100 blocks crosswise and 20 blocks lengthwise. It was noted that slippage of small clusters occurred more frequently than the larger ones. A less computationally expensive probabilistic model was proposed as an alternative to the BK model; this probabilistic approach bears resemblance to the Markov chain model we propose in Chapter 4.1.

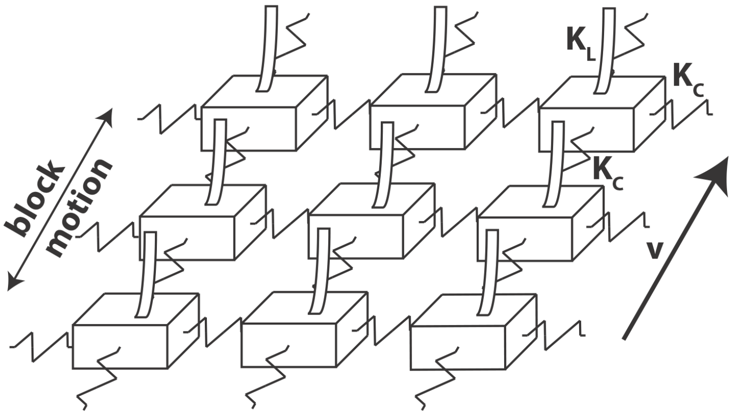

Figure 2.4: A two-dimensional implementation of the BK model (Otsuka, 1972b). Blocks are interconnected with identical spring constants K_c and to the loading plate via a loading spring K_L. The loading plate is being pulled at a constant velocity v relative to the frictional surface with block motion occurring parallel to the direction of loading plate.

The alternative model is a chain-reaction source model that conceptualized the magnitude-frequency relation as a probability controlled phenomenon (Otsuka, 1972a). A chain reaction starts with a single slip which can propagate into new slips of neighboring blocks each with a probability of p. This process is repeated until all rupture progression has halted with the resulting number of slips being the total number of successes from all steps; Figure 2.5 illustrates this stochastic concept model for two nearest neighbors. The author suggests that the extent of the focal region and the amount of energy liberated during a seismic event is a result of probability controlled fracture formation.

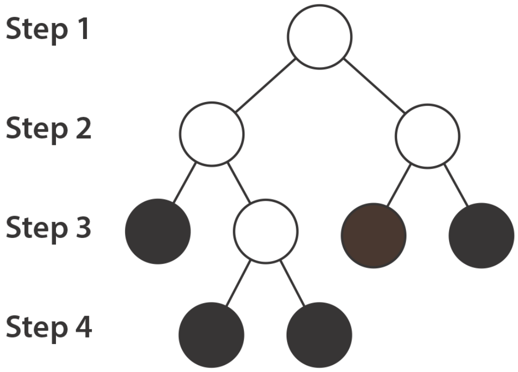

Figure 2.5: Chain-reaction source model that simulates the progression of slips of the spring-block model through a stochastic process (Otsuka, 1972a). In step 1, the model starts with a single failure (white circle) which may induce two new slips each with a probability p. This process is repeated until all rupture chains have halted (black circle). In this case the resulting number of slips is 4 (1+2+1).

2.3.3 Rundle, Jackson and Brown (RJB) Model

Dieterich (1972b,a) examined the role of time-dependent friction as a possible mechanism for aftershocks from a numerical model based on the BK model. Later, Rundle and Jackson (1977) implemented a slider block model with massless blocks based on the models of Dieterich (1972a) and Burridge and Knopoff (1967) to simulate earthquake sequences of a fault. The model parameters where chosen to replicate faulting of a granitic rock along a frictional surface with model dimensions with displacement in cm, time in years, plate velocity in cm/year and stress in kbar. The seismic behavior of the model was fairly representative of reality, although the stress drops and average magnitudes did not agree as well.

The idea of utilizing cellular automaton models to replicate complex systems through the dynamics of simple interaction is easier to implement and very effective at simulating macroscopic physical systems (Von Neumann and Burks, 1996). The CA model is a conceptual 2-D model with each block having certain states that respond to inputs in a predefined set of rules. It is possible to represent classical mathematical processes through the many body interactions of a CA model.

Bak et al. (1988) examined self-organized criticality (SOC) in which a sandpile model evolves into critical states while remaining robust to varied initial conditions, system parameters, and under the presence of quenched randomness. The authors argue that studying the general behavior of the system based on discrete cellular automata offers the advantage of being much easier to implement and analyse than system based on continuous partial differential equations. These generalized systems can evolve towards a self-organized critical state with spatial and temporal power-law scaling behavior with possible application to earthquakes (Bak et al., 1988; Bak and Tang, 1989).

Rundle and Brown (1991) presented a simplified cellular automaton model based on previous spring-block models (Rundle and Jackson, 1977; Dieterich, 1972a; Burridge and Knopoff, 1967). This model idealized the contact surfaces of a block as massless microscopic contact points that fail and slip relative to each other in a stick-slip process. Each microblock is an asperity, or rough stuck surface, on the underside of the macroscopic block, as shown in Figure 2.6. A microblock is frictionally stuck to the surface until local forces become large enough to break the contact and cause the block to jump laterally to a new local equilibrium position plus a random overshoot. The RJB automaton model replaces the details of the microscopic cohesion-decohesion of a block with a simple jump rule, which is appropriate for small loading plate velocities v. Increases in velocities produce a decrease in frictional resistance, otherwise known as velocity weakening. Therefore, an increase in plate velocity v produces an excess number of lattice clusters for a brief duration allowing slip on the lattice to catch up. The bottom of the macroscopic block, see Figure 2.6, becomes divided into an $L \times L$ lattice of joining microscopic squares as shown in Figure 2.4.

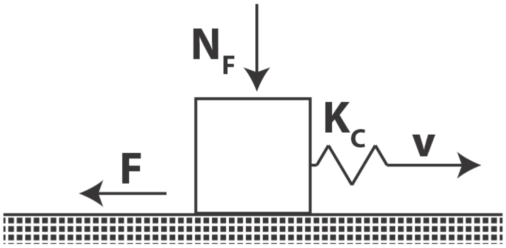

Figure 2.6: Rundle and Brown (1991) macroscopic block being dragged over a contacting surface at a velocity v by a ram-piston K_c at a normal force of N_F.

The force σ_i of the ith square is calculated as

$$\sigma_i(t) = p_i(t) + \sum_j T_{ij}\phi_j(t), \text{ where } \phi_j(t) = s_j - vt, \tag{2.8}$$

and p_i is the externally applied force and T_{ij} is an interaction between the squares neighbors' (Green's function). The parameter ϕ is the slip deficit with s_j being the total distance block j has slipped relative to the loading plate translating at a velocity v at a time t; in other words, the amount the block lags behind the driving fixture (Brown et al., 1991). Block slip is parallel to the direction of motion of the loading plate.

The system is evolved by incrementing t by δt producing a force of $\delta\sigma_i = -\sum_j T_{ij}V\delta t > 0$ at all sites. Each block is assigned a failure envelope σ_i^F with slip occurring if $\sigma_i > \sigma_i^F$. If slip occurs, the amount of slip is $s_i = (\sigma^D - \sigma_i)/T_s$, where σ^D is the dynamic frictional strength and T_s is the self-interaction term.

The RJB automaton model evolves following the rules of:

1. Begin with random initial conditions $s_i(0)$, set $p_i(0)$.
2. Increment time t by δt.
3. Calculate local stress σ_i.
4. (a) Fix time t, locate all active sites ($\sigma_i > \sigma_i^F$).
   (b) Adjust slip of all such sites as $s_i \rightarrow s_i + \delta s_i$, set $\sigma_i \rightarrow \sigma^D$.
5. Repeat step 4 until no active sites remain.
6. Repeat step 2-5 until t reaches set end time.

The model contains two timescales Γ and Δ, where Γ is the average time for a microblock to fail upon sufficient shear force and Δ is the average time interval between successive application of shear forces. The model of Rundle and Brown (1991) matches macroscopic laboratory observations in the limit of $\Delta \gg \Gamma$ meaning that the loading plate does not move while an event is occurring. As an aside, the order of slip adjustments should not matter as time is fixed while adjustments to the slip are made for all failed sites.

2.3.4 Olami, Feder and Christensen (OFC) Model

Olami et al. (1992) presented a nonconservative cellular automaton that displays self-organized criticality equivalent to the two-dimensional Burridge-Knopoff spring-block model. The system is mapped onto a square $L \times L$ array of blocks. The blocks are driven by the relative motion of the loading plate, where the total force on a block $F_{i,j}$ is expressed as

$$F_{i,j} = K_c[4dx_{i,j} - dx_{i-1,j} - dx_{i+1,j} - dx_{i,j-1} - dx_{i,j+1}] + K_L dx_{i,j}, \qquad (2.9)$$

where $dx_{i,j}$ is the relaxed position of block (i, j) with elastic constants K_c and K_L (Olami et al., 1992). When a site reaches a threshold value ($F_{i,j} \geq F_{thr}$) an earthquake is triggered and the process of relaxation begins. For Olami et al. (1992) model, the redistribution of strain after a local slip at a position (i, j) is given by

$$\begin{aligned} F_{i\pm1,j} &\to F_{i\pm1,j} + \delta F_{i\pm1,j}, \\ F_{i,j\pm1} &\to F_{i,j\pm1} + \delta F_{i,j\pm1}, \qquad (2.10) \\ F_{i,j} &\to 0, \end{aligned}$$

where the increases in nearest-neighboring force are

$$\delta F_{i\pm1,j} = \frac{K_c}{4K_c + K_L} F_{i,j} = \alpha F_{i,j},$$

$$\delta F_{i,j\pm1} = \frac{K_c}{4K_c + K_L} F_{i,j} = \alpha F_{i,j}, \tag{2.11}$$

where α is the elastic ratio. The Olami et al. (1992) model evolves using the following algorithm:

1. Set all sites to a random initial force $F_{i,j}$
2. If there are any active site ($F_{i,j} \geq F_{thr}$) then redistribute the force $F_{i,j}$ to neighbors according to the rules
    (a) $F_{n,n} \rightarrow F_{n,n} + \alpha F_{i,j}$,
    (b) $F_{i,j} \rightarrow 0$,

    where $F_{n,n}$ are the strains for the four-nearest neighbors.
3. Repeat step 2 until no active sites remain.
4. Locate site with the block closest to slip $max(F_{thr} - F_{i,j})$ and add the difference to all sites and return to step 2.

The total number of relaxations in the evolution of the earthquake is proportional to the energy E released during an earthquake (Eq. 2.6), from which a power law distribution can be plotted of the number of observed earthquakes with energy greater than E.

Olami et al. (1992) noted that the continuous, non-conservative cellular automaton exhibits SOC behaviour for a wide range of elastic ratios α under varied system size L and external noise. As the lattice size is varied for L =15, 25, 35, and 50, the exponent of the power law remains constant for a fixed elastic ratio α, while the maximum possible earthquake energy scales with the system size as $L^{2.2}$. Olami et al. (1992) simulated results for an 35×35 block system with varied elastic constants α are shown in Figure 2.7; the variance observed in the scaling exponent, or slope, depends on the elastic constant α. As the elastic constant α is lowered the movement of the blocks becomes increasingly uncorrelated due to the decrease in block interactions.

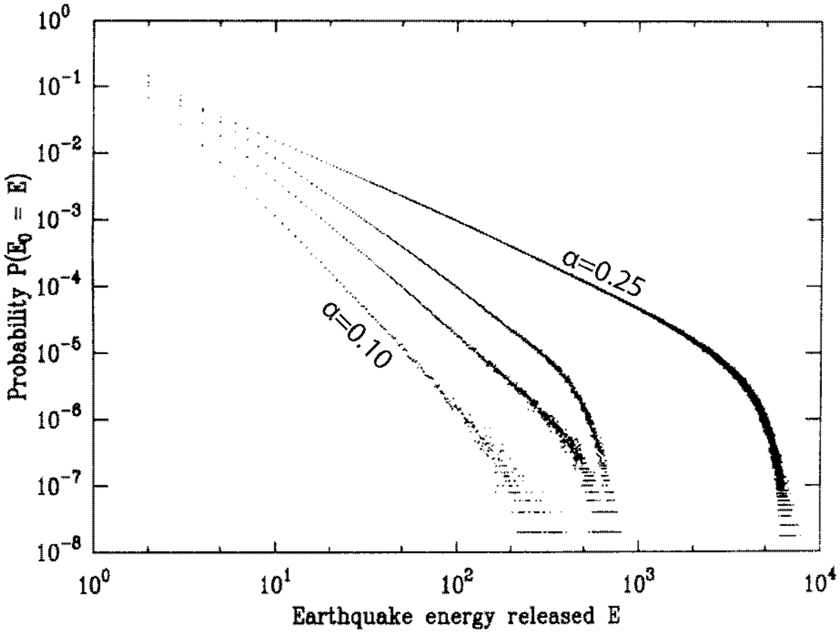

Figure 2.7: Simulated results for the probability density of having an earthquake of energy E as a function of E. The curves correspond to models with an elastic constant of $\alpha = 0.10, 0.15, 0.20, \text{and } 0.25$, from left to right. Modified Figure 2a from Olami et al. (1992).

2.4 The BK, RJB and OFC models

The BK model consists of blocks of mass m interconnected by springs of constant K_c resting on a surface with a velocity dependent friction force. These blocks are connected by springs K_L to a loader plate moving at constant velocity v (Burridge and Knopoff, 1967). Numerically solving the BK model is computationally difficult, therefore a simpler formulation was implemented in the form of the RJB model.

The RJB model simplifies the friction force of the block into a stick-slip model where individual blocks are assigned a failure threshold σ_F and a residual threshold σ_R (Rundle and Jackson, 1977; Rundle and Brown, 1991). An initial position is assigned to the blocks, along with an internal stress that incorporates the forces due to the coupling springs K_c and the loading springs K_L. In simplification, when a block fails its displacement Δx is given as

$$\Delta x = \frac{\sigma_i - \sigma_R}{K_L + qK_c}, \tag{2.12}$$

where q is the number of neighbors of a block (Rundle and Jackson, 1977; Klein et al., 2017). The blocks are assumed to have zero mass to neglect inertial forces in the motion of the blocks, therefore the extent of motion is underestimated (Rundle and Jackson, 1977). Rundle and Jackson (1977) note that this simplification should mainly affect the generation of seismic waves and should not affect the model statistics greatly.

In earthquakes the stress transfer occurs over long range, therefore the number of interconnected neighboring blocks q tend to be much greater than the four nearest neighbors of $q = 4$ of a two-dimensional system (Klein et al., 1997, 2000). Within the RJB model, when a block is moved a distance Δx the amount of stress dissipated is given as $\Delta\sigma_{diss,\,RJB} = K_L \Delta x$ (Klein et al., 2017). Therefore, the amount of stress dissipated $\Delta\sigma_{diss,\,RJB}$ when a block is moved is given by

$$\Delta\sigma_{diss,\,RJB} = K_L[\frac{\sigma_i - \sigma_R}{K_L + qK_c}], \tag{2.13}$$

for the RJB model (Klein et al., 2017). Within the OFC model, the amount of stress dissipated is given as

$$\Delta\sigma_{diss,\,OFC} = \alpha(\sigma_i - \sigma_R), \tag{2.14}$$

where the fraction α represents the amount of stress lost and not redistributed to the neighboring blocks (Klein et al., 2017). Hence, the amount of stress lost after a failure can be made identical for the RJB and OFC models by setting Equations 2.13 and 2.14 equal to each other, which simplifies to

$$\alpha = \frac{K_L}{K_L + qK_c}. \tag{2.15}$$

After dissipation, if both the RJB and OFC models have identical lattice systems and number of neighboring cells q than the amount of stress left to be transferred to neighboring blocks is identical (Klein et al., 2017). Therefore, in terms of stress on each block the RJB and OFC models can be made equal.

It should be noted that the RJB model has a natural definition of energy, namely the energy stored in the springs, whereas the OFC model has no natural definition of energy (Klein et al., 2017). In simplification, the fraction 1-α

represents the elastic ratios that governs the stress transfer to neighboring blocks after a block's failure, whereas σ_i represents the internal stress of a given block that incorporates the sum forces from the coupling springs K_c and the loading springs K_L.

2.5 Model Ingredients

Simulations of the BK model require solving Newton's equation of motion which is very time consuming, thus CA models have been proposed as an alternative. These CA models ignore the mass of the blocks, therefore neglecting the inertia of the blocks, and simplify the motion of the blocks by using a jump or transition rule (Rundle and Klein, 1993; Xia et al., 2008). Rundle and Klein (1995) argue that inertia is less important than other entropic and internal energies as seismic radiation loss during an earthquake is less than $5-10\%$ (Kanamori and Anderson, 1975). Likewise, a jump rule friction law is utilized to create a stick-slip block motion of the blocks identical to a Mohr-Coulomb law where failure σ_F and residual σ_R thresholds are specified to create a failure mechanic (Olami et al., 1992; Rundle and Brown, 1991; Rundle and Klein, 1995); equivalently, the slip (failure) of the block on the frictional surface can be thought to occur when $\mu_s > \mu_d$ where μ_s and μ_d are static and sliding coefficients of friction, respectively, of the rough surface.

This allows to simulate systems that are much larger and extend to two-dimensions or three-dimensions compared to the one-dimensional Burridge-Knopoff models (Bak et al., 1988). Bak et al. (1988) note that both two and three dimensional systems can evolve towards a power law scaling behavior with an universal exponent. Systems in the near mean-field limit (infinite range) that exhibit mean-field critical points require long range stress transfer and a large enough lattice to overcome the finite size effect (Bak and Tang, 1989; Klein et al., 1997, 2000, 2007).

A certain amount of randomness, or noise, is also required such that the evolution of the system does not synchronize. These may be a certain amount of disorder set at initial model conditions, a randomness introduced into the failure threshold (static friction) over time, or simply choosing a site at random to additionally add stress onto (Turcotte, 1999; Pelletier, 2000; Castellaro and Mulargia, 2001).

Furthermore, it is necessary that the systems be dissipative (energy released) either across the lattice or at the boundaries with energy fed into the system in bulk or through the boundaries (Bak and Tang, 1989). The flux of energy occurs in two timescales, being the very slow loading time (energy given) and the fast block rupture time (energy released). The loading rate can be considered as a slow tectonic buildup, whereas the rate of elastic rebound is much greater. In order to ensure that the rate of loading is always much less than the rate of rupture, tectonic loading may only occur as long as all blocks are stable (Bak et al., 1988; Rundle and Brown, 1991; Gabrielov et al., 1994; Pelletier, 2000). In real cases of earthquakes tectonic loading may be in the order of a century, whereas the largest earthquake may be as long a couple of minutes (Gabrielov et al., 1994). In our CA model, the slow time scale is called plate update time t_{pu} with the fast development of the avalanche called the inner plate update time t_{in}.

2.6 Modern Model Variations

The cellular automaton version of the BK model has been the subject of considerable interest in seismology, along with the concept of self-organized criticality and seismicity. A self-organized system is one that naturally evolves to critical states without detailed specification of the initial conditions, while remaining robust with respect to variations of parameters and the presence of quenched randomness (Bak et al., 1988). Janosi and Kertesz (1993) concluded that various amounts of conservation (dissipation) and randomness both affect critical behavior and scaling; furthermore, the characteristic avalanche sizes for any non-conservative system is restricted to being smaller than the system size.

When blocks are only connected to nearest-neighbouring springs the number of earthquakes n_s with s slipped blocks exhibit a power-law dependence on s as $n_s \sim s^{-x}$, with $x \approx 2$ (Xia et al., 2005). A generalized version of the CA models has been formulated to include more realistic long range stress transfer ($R \gg 1$) rather than just the nearest-neighbors ($R = 1$), where R is the radius from a given block to the surrounding blocks (Rundle and Klein, 1993). This way, each block is connected to many other blocks, thus generating a mean-field behavior, cluster structure and spinodal nucleation; the spinodal corresponds to the limit of metastable states with fluctuation about a critical point responsible for the observed scaling of avalanche sizes (Rundle and Klein, 1995; Klein et al., 1997, 2000, 2007). These CA models with long-range stress transfer, $R \to \infty$, have been shown to exhibit clustering scaling that can be described by the Fisher droplet model distribution (nucleation process) as

$$n_s = n_0 \frac{exp(-\Delta h s)}{s^{\tau}}, \tag{2.16}$$

where n_s is the non-cumulative count of failed cells with size s (Fisher, 1967; Klein et al., 2000, 2007). As such, n_0 is a measure of the seismicity, whereas Δh is the limit of stability (spinodal), and $\tau = 3/2$ (mean-field exponent) for systems with long range stress transfer (Klein et al., 2000, 2007). Therefore, constants n_0 and Δh of Equation 2.16 are analogues to constants N_T and b of Equation 2.4.

Gabrielov et al. (1994) examined different fast time dynamics, where fast time is associated with the fracture event for two broad classes; a series and a parallel model. In a series model, an instantaneous release of stress at a failed site is followed by a transfer of some fraction of the stress to the neighbouring sites. If the amount of stress released is reduced to zero (residual threshold), then the model displays a $1/f$ size-frequency law for low dissipation parameters termed periodic chaos. If the amount of stress released is reduced by a fixed amount a periodic behavior appears, but to a lesser degree. In a parallel model, there is a relatively slow release of stress at a failed site with instantaneous transfer of stress to neighboring cells. Theses models converge to a power law, but with an exponential cutoff that depends on the dissipation parameter of the system.

Ramos et al. (2006) observed nontrivial quasiperiodic behavior in their variation of the OFC model with the period of large avalanches proportional to the degree of dissipation. When noise is added, as either variations in the dissipation parameters or the failure thresholds of blocks, the periodicity diminishes while the system remains showing the avalanche size distribution that follows a power law.

Xia et al. (2005, 2008) simulate the BK model with variable range stress transfer and found that a system with long range stress transfer $R \gg 1$ and high dynamic friction force $\alpha \leq 1$ (damped motion) is consistent with the behavior of long range CA models. The scaling regime for a BK model with $\alpha \to 0$ and $R \gg 1$ was found to be consistent with an equilibrium spinodal critical point and a mean-field exponent of $\tau = 3/2$ as described by Klein et al. (2000). For low dynamic friction force $\alpha \geq 1$ and large R the system becomes nonergodic (spatial and temporal averages are not constant over time and space) due to quadiperiodic behavior of stress.

Tiampo et al. (2003, 2007) employ the Thirumulai-Mountain fluctuation metric (Thirumalai and Mountain, 1993) to seismic data and the slider block model to evaluate effective ergodicity or rather if stationarity and equilibrium states exists in earthquake fault models. The authors suggest that equilibrium in fault systems exists between large events that drive the system out of equilibrium for some time after which a quasiequilibrium state is re-established; these fault systems display some dynamics of driven mean-field systems seen in numerical simulations such as the slider block models.

Other studies have utilized the CA model to examine earthquake dynamics such as magnitude and scaling, clustering, spatial heterogeneities or damage, foreshocks and aftershocks (De Rubeis et al., 1996; Castellaro and Mulargia, 2001; Serino et al., 2010; Dominguez et al., 2013; Kazemian et al., 2015). De Rubeis et al. (1996) proposed an alternative model that examined the critical behavior generated by a pre-existing fractal geometry of the fault. Their study suggests that roughness of the fault is related to the earthquake statistics, and thus observed scaling relations. Castellaro and Mulargia (2001) considered different loading such as time-dependent loading (one initiating failure), and random loading of individual lattice sites (numerous initiating failures). As a greater number of random initiating failures are introduced the system becomes more dissipative with the frequency-size distribution of all events becoming bell-shape as small sized events tend to disappear.

Serino et al. (2010) examined the role of damage with two variants; the first is where a site has several lives prior to becoming dead after which it no longer interacts with the system, and the second being where the dead site dissipates all received stress. The first variant effectively decreases the simulated system to a smaller size, whereas the second increases the system's dissipation. Incorporating damage into the CA models has been shown to change scaling with the idea that variations in the scaling exponent b is affected by underlying fault systems, which may vary from one tectonic region to another (Serino et al., 2010). Dominguez et al. (2013) examined the influence of spatial inhomogeneities due to damage and inhomogeneous stress dissipation; spatial distributions of inhomogeneities affect scaling even if system dissipations are equivalent. Kazemian et al. (2015) incorporated heterogeneities in the form of strong cells that have higher failure thresholds ($\sigma_{F_{asp}}$) than the surrounding cells (σ_F). The introduction of these heterogeneities produced foreshock and aftershock sequences similar to the spatial and temporal clustering observed in natural seismicity.

Serino et al. (2011) propose that various amounts of damage (stress sink) occurring in the fault system can be incorporated into a modified GR scaling (Eq. 2.16) in the form of

$$n_s = \frac{N}{1-q}\frac{exp(-q^2 s)}{s^{\tau}}, \tag{2.17}$$

where n_s is the non-cumulative count of failed cells with size s, q is the amount of damage sites and N is the average seismic activity on an undamaged system ($q = 0$). In real fault systems the varying levels of damage can be caused by different levels of fracture or gouge; as the amount of damage q increases the occurrence of large events decreases, while the occurrence of small events increases. Serino et al. (2011) suggest that the underlying GR scaling is dependent on the degree of damage over the entirety of the fault system.

A detailed sensitivity analysis of the OFC model and influence of asperities with low noise has been studied by Gu (2016), where noise η is the fraction randomness added to a cell's residue stress after failure $\sigma_R(1 \pm \eta)$. In general, the OFC model's system stress evolves into a periodic state with very low noise ($0\% < \eta < 0.1\%$) with the system behavior becoming quasiperiodic with moderate noise ($10\% < \eta < 30\%$). For high noise ($\eta > 30\%$), there is no apparent periodic behavior.

Gu (2016) attributes this periodicity due to the system's memory of previous events; as noise increases the system's mixing time decreases along with a decrease of the period. Likewise, a system's memory decreases as the system size L and long range interaction R increases, although to a much lesser impact than increasing noise. The behavior of a single asperity significantly improved scaling while introducing periodicity to the lattice if the failure threshold is significantly higher than surrounding cells (Gu, 2016).

As a summary, the BK and RJB models aimed to construct a numerical model to explore the role of friction along a two-dimensional fault and to investigate the underlying seismology (earthquakes) (Burridge and Knopoff, 1967; Rundle and Jackson, 1977; Rundle and Brown, 1991). The OFC model simplified the dynamics of earthquakes and suggested association to a nucleation phenomenon (Klein et al., 2000, 2007). As the model grew in size, the cellular automaton models have taken the role of simulating fault systems consisting of multiple single faults (Serino et al., 2011, 2010; Dominguez et al., 2013). Conceptually, these models went from modeling single faults (dozen kilometers) to fault systems (hundred kilometers). Within this study we conceptualize the CA model as the latter with our implementation of asperities (inhomogeneities) representing faults within a larger system.

In the next chapters, we describe the CA model implementation in more detail, then derive a theoretical model to predict its behavior based on absorbing Markov chains. This is followed by an in-depth numerical and analytical analysis of the effect of heterogeneities on failure patterns.

Chapter 3

Cellular Automaton Theory

3.1 Cellular Automaton

The cellular automaton model discussed is an extension of the OFC model, see previous chapter, but with the redistribution of stress considered over a much longer range than the four nearest neighbors. Likewise, the amount of stress dissipated is dependent on a dissipation parameter that effectively incorporates the elastic ratios. The failure of a block is no longer a function of a velocity dependent friction law, but rather a simplified threshold implementation. The stresses acting on a block due to the springs have also been simplified into a single unitless internal stress value. Nonetheless, the CA model remains the easiest way to simulate and modify a simple earthquake fault model.

3.1.1 Homogeneous Model

The 2-D cellular automaton is composed of cells that form in a general square grid. In our case, the model's coordinate system is arranged into a hexagonal grid through offset coordinates created by J. Kazemian (unpublished). The circularity of a hexagonal grid makes it the preferred method for modelling fluid movement and connectivity (Birch et al., 2007). The lattice grid has L by L hexagonal cells with periodic boundaries. Within the lattice, each cell is assigned a residual threshold σ_R (stuck) and a failure threshold σ_F (slip). As a note, the model uses a single failure threshold σ_F to determine the failure

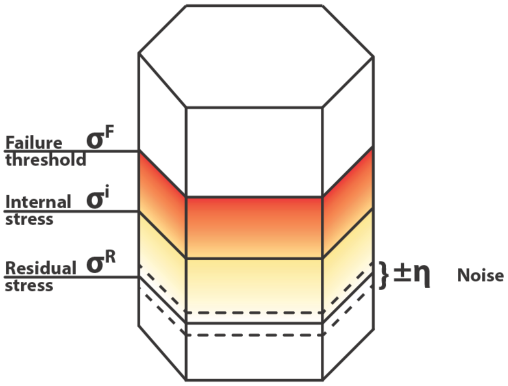

Figure 3.1: An individual hexagonal lattice cell. Each cell is assigned a residual threshold ($\sigma_R \pm \eta$), an internal stress (σ_i) and a failure threshold (σ_F).

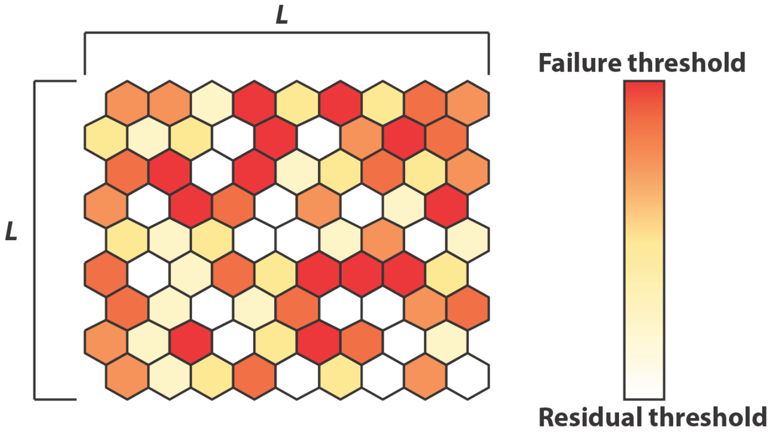

Figure 3.2: A lattice grid containing L by L hexagonal cells. Each individual cell within the lattice has an internal stress σ_i that lies between the residual threshold and failure threshold, as shown with the colorbar.

of a cell rather than two or three principal stresses. We impose randomness on the residual threshold $\sigma_R \pm \eta$, where η is uniformly distributed noise. Each cell is assigned a random internal stress σ_i such that $\sigma_R < \sigma_i < \sigma_F$, as shown in Figure 3.1. After initialization, the lattice will have a uniformly distributed internal stress distribution, as shown in Figure 3.2. To further remove the dependence of initial conditions the model is left to run for an extended period prior to collecting any statistics.

To initiate a failure event the entire lattice is searched for a cell closest to failure or in other words having the least stress difference of $min(\sigma_F - \sigma_i)$. This minimum stress difference of $min(\sigma_F - \sigma_i)$ is added to each cell of the entire lattice. The process of inducing a single initiating failure within the lattice is known as a plate update time t_{pu}. At this point, a minimum of one failure must occur within the system.

Consequently, the initiating failure has a stored potential stress of $\sigma_F - \sigma_R$. The internal stress σ_i of the failed cell is lowered to its residual threshold $\sigma_i = \sigma_R \pm \eta$; conceptually, after a failure the strain on the cell is set to its relaxed position plus or minus some random overshoot. A fraction of the stress, given by $(1 - \alpha)[\sigma_F - \sigma_R]$, is equally redistributed among neighboring cells within a cell radius of R as long range stress transfer. The fraction α is a dissipation parameter that lies in between $0 < \alpha \leq 1$. Another portion of the released stress, given by $\alpha[\sigma_F - \sigma_R]$, is permanently lost. If no stress dissipation existed, that is $\alpha = 0$, the total system stress would quickly increase such that a never-ending chain reaction of cell failures would occur.

Physically, the long range stress transfer R represents the coupling between a cell and it's surrounding neighboring cells; it is analogous to Green's function of the earth. It has been suggested that a more appropriate interaction range should follow a $1/R^3$ decay, but for simplicity we have assumed a uniform stress redistribution (Klein et al., 2000). Within a given plate update time there might be subsequent cell failures that occur due to the long range stress redistribution; these are referred to as inner plate update times t_{in}.

The lattice is searched to flag any additional cell failures $\sigma_i \geq \sigma_F$ that are due to occur after the redistribution of stress from previously failed cell(s). If so, the flagged cell(s) are iteratively failed and the process of stress redistribution $(1 - \alpha)[\sigma_i - \sigma_R]$ within a range of R is repeated at their coordinates, where σ_i may be larger than σ_F. Therefore, the cells involved within the range R are slightly different between each inner plate update time t_{in}. Additionally, the amount of stress released $\sigma_i - \sigma_R$ during subsequent cell failures is not constant and may vary depending on the given internal stress σ_i of the failing cell. Once a cell fails, their internal stress is set to $\sigma_i = \sigma_R \pm \eta$, where η is a random overshoot. Within any given inner plate update time, any one cell may only fail once.

The end of an inner plate update time t_{in} is when all flagged cells have failed. The total number of cells failures m that occurred during that inner plate update time t_{in} is recorded in a failure sequence $\{1, \ldots, m\}$. Afterwards, the inner plate update time is increased $t_{in} = t_{in}+1$ and the lattice is iteratively searched to flag any additional cell failures $\sigma_i \geq \sigma_F$ that are due to occur after the most recent redistribution of stress. If so, the process of cell failures and stress redistribution is repeated. Potentially, any one cell may fail once more at the next inner plate update time.

Once all subsequent cell failures and stress redistribution have occurred, in other words $\sigma_i < \sigma_F$ for all cells, the failure sequence has come to a halt $\{1, \ldots, 0\}$. At a given plate update time t_{pu}, the final size of the event is the sum of the failure sequence $\{1, \ldots, 0\}$ across all inner plate updates t_{in}; this is how we simulate our time series of the total cumulative cell failures S_{cum} per plate update time t_{pu}. During the inner plate update times t_{in}, or development of the failure sequence, time is fixed. In other words, the avalanche sequences occur instantaneously compared to the loading rate of the system. Each cell failure is counted as having generated an earthquake of magnitude one, where the sum of all cell failures in a plate update t_{pu} is considered as the total magnitude of that event.

Finally, the plate update time step is increased by one $t_{pu} = t_{pu} + 1$. At the next plate update time, the entire described process is repeated and the lattice is searched once again for a new $min(\sigma_F - \sigma_R)$ to induce one failure. Shown in Figure 3.3 is a flowchart of the process outlined above.

Shown in Figure 3.4 is a top down view that demonstrates the basic dynamics of the model. Starting with Figure 3.4a, the center cell (orange) represents a cell closest to failure. The model's redistribution range is $R = 2$. Prior to a plate update no cell failures have occurred. In Figure 3.4b, the minimum stress difference of $min(\sigma_F - \sigma_R)$ is added to the entire lattice to initiate one failure. At the first inner plate update there is always one cell failure.

In Figure 3.4c, the center cell has subsequently failed and redistributes a fraction of its internal stress to the surrounding cells within the range of R. After failure, the center cell's internal stress σ_i is lowered to the residual threshold σ_R. Due to the redistribution of stress, the two surrounding cells have their internal stress σ_i above their failure threshold $\sigma_i \geq \sigma_F$. At the second inner plate update time two cell failures have occurred.

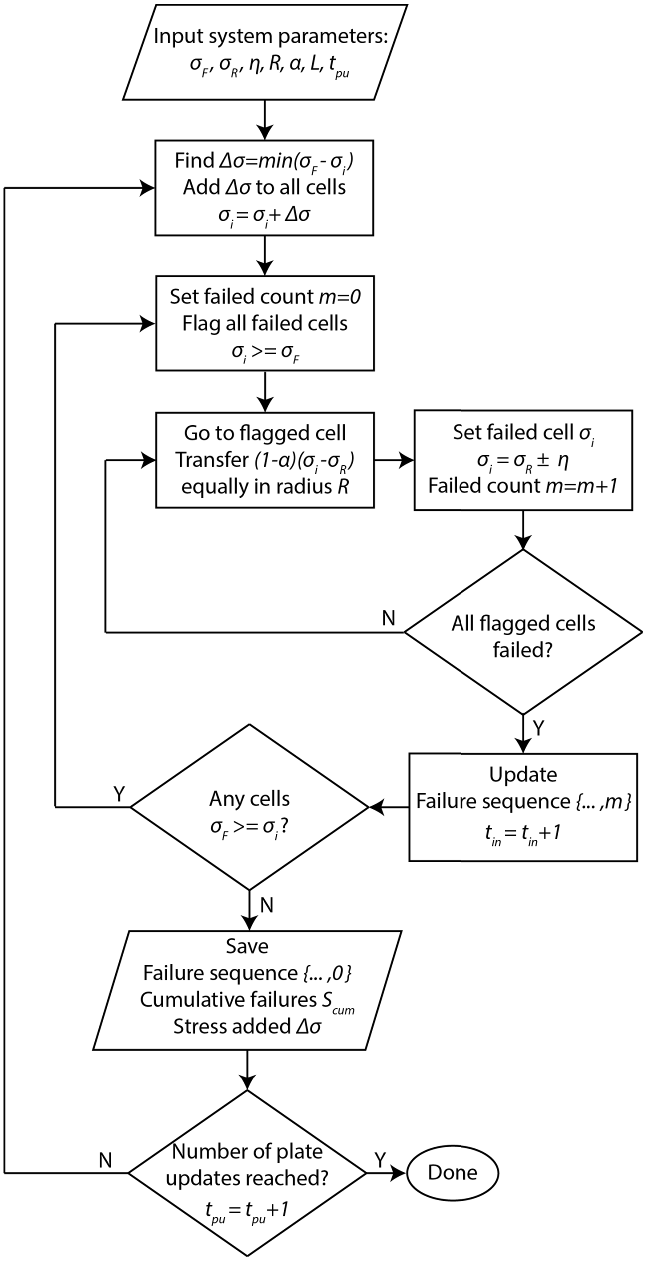

Figure 3.3: Flowchart of the Cellular Automaton. The failure sequence $\{1, ..., 0\}$ is built by inducing the failure of the most critically stress cell $min(\sigma_F - \sigma_i)$ and propagating the avalanche sequence at each inner plate update time t_{in} until all due cells have failed. This process is repeated for a predefined number of plate update times t_{pu}.

Subsequently, in Figure 3.4d, two outer edge cells have redistributed a fraction of their stress to their respective surrounding cells. Their internal stresses σ_i are lowered to the residual threshold σ_R. Since there are no longer any cells with $\sigma_i \geq \sigma_F$ the avalanche process has come to a halt. At the end of this plate update time the cumulative number of failures is three, with one failure occurring at the first inner plate update time and two failures occurring at the second inner plate update time, as shown in Figure 3.5.

Afterwards, the next plate update time $t_{pu} = t_{pu} + 1$ takes place; the minimum stress difference of $min(\sigma_F - \sigma_i)$ is added to each cell of the entire lattice to initiate a cell failure and the process is repeated.

At the very beginning, the lattice is initialized with uniform randomly distributed internal stresses σ_i such that $\sigma_R - \eta < \sigma_i < \sigma_F$. Prior to collecting data from the model, a burn-in period is ran to remove any transient effects prior to recording data. As a reference, in Castellaro and Mulargia (2001) OFC model stationarity is achieved when the net stress input is roughly equal to the net stress output in roughly 10^6 plate updates, whereas Serino et al. (2011) utilize a 4×10^6 plate updates burn-in period.

3.1.2 Inhomogeneous Model

A cellular automaton model with inhomogeneities better represents a fault system with varying degrees of damage present as a collection of faults or microcracks (Serino et al., 2010;Serino et al., 2011;Dominguez et al., 2013;Kazemian, 2013;Kazemian et al., 2015). In our model, inhomogeneities are incorporated as asperities with an increased failure threshold $\sigma_{F_{asp}}$ compared to a normal cell, as shown in Figure 3.6. Therefore, an asperity has a greater capacity to store and release stress back into the system. The addition of inhomogeneities, along with their spatial distributions, greatly affects the statistical distribution of earthquakes (Dominguez et al., 2013;Kazemian et al., 2015;Klein et al., 2017). A modified Gutenberg-Richter scaling approach suggested by Serino et al. (2011) incorporates different levels of damage found in a lattice system. Yet, exactly how various inhomogeneous structures further change frequency-magnitude scaling is still under study.

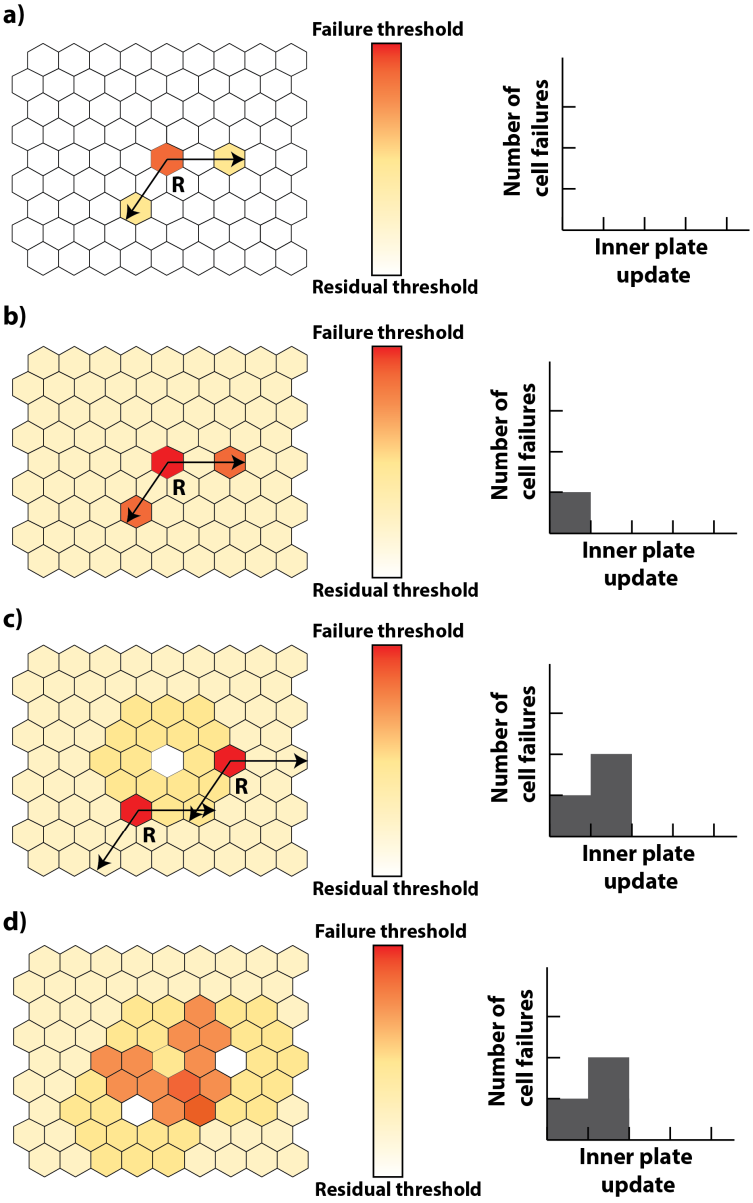

Figure 3.4: Top down view of a lattice system demonstrating the basic dynamics of the system. a) The center cell (orange) is closest to failure with the model's redistribution range set to $R = 2$. Prior to a plate update no cell failures have occurred. b) The minimum stress difference has been added to the entire lattice to initiate one failure (red). The center cell will redistribute a fraction of its stress within a stress transfer range of $R = 2$ prior to the next inner plate update time. c) Note that the previously failed cell has its internal stress lowered to the residual threshold (white). Due to the previous failure, two additional cells with the range R are brought to failure (red). At the second inner plate update time two cell failures have occurred. d) The two previously failed cells have redistributed a fraction of their stress to their respective surrounding cells. Their internal stresses are lowered to their residual thresholds (white). There are no longer any cells to fail, therefore the avalanche process has come to a halt.

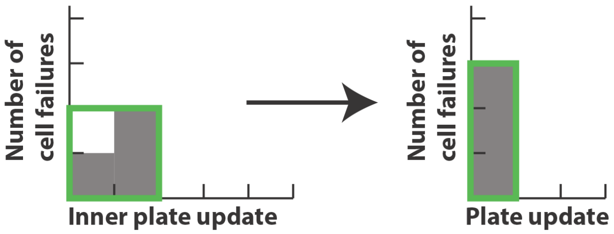

Figure 3.5: Inner plate update to plate update. At the end of this plate update the cumulative number of failures is three, with one failure occurring at the first inner plate update and two failures occurring at the second inner plate update.

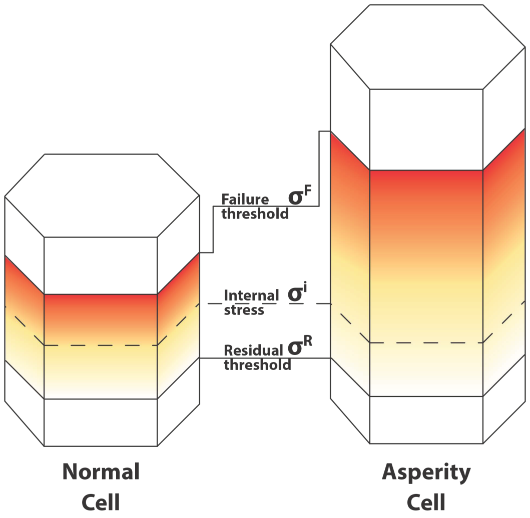

Figure 3.6: A normal cell (left) compared to an asperity cell (right) that has an increased failure threshold σ_F. An asperity acts as a stress sink until failure occurs and a greater amount of stress is released back into the system.

3.1.3 Plate update time and physical time

Our model has two time scales, which are called plate update time t_{pu} and physical time t_{phys}. Traditionally, the Burridge and Knopoff (1967) model uses a rigid driving plate to load stress unto the spring-blocks via the loading springs K_L. These blocks are driven by a loading rate much lower than the rate of elastic rebound of the slipped block (Pelletier, 2000). Yet, in computer modeling the motion takes place in discrete jumps otherwise known as a plate update. To ensure that the loading rate is always much less than the slip event of the blocks loading may only occur while all blocks are stable. During a slip event, or inner plate update time t_{in}, time is frozen and no loading occurs.

In our case, a plate update time t_{pu} is an iterative step in our model that adds the minimum stress $min(\sigma_F - \sigma_i)$ to all lattice cells required to fail a single cell closest to the failure threshold. This assures that in most cases a single unstable block initiates an avalanche effect while increasing computational efficiency.

In classical mechanics, the loading plate exerts a force uniformly onto the lattice equivalent to $L^2 K_L V \Delta t$, where L^2 is the total system cells, V the plate velocity and Δt a discrete time step (Burridge and Knopoff, 1967;Olami et al., 1992). In the CA models, we add $\Delta\sigma = min(\sigma_F - \sigma_i)$ units of stress to each cell, therefore increasing the total system stress by $L^2\Delta\sigma$. Therefore, both formulas can be equated and solved for time Δt, which we refer to as a time proxy t_{phys} that can be considered as the tectonic time scale of the model. We can relate physical time steps t_{phys}, dimensionless proxy to time, to the added stress $\Delta\sigma$, dimensionless, at a given plate update time steps through

$$t_{phys} = \frac{\Delta\sigma}{K_L V} = c\Delta\sigma, \tag{3.1}$$

where c is a constant depending on a fixed driving plate velocity V and spring constant K_L (Kazemian and van der Baan, 2015). Therefore, the cumulative amount of stress added $\sum\Delta\sigma$ at each plate update time t_{pu} is proportional to the physical time t_{phys}. This allows us to relate plate update time t_{pu} to physical time t_{phys} and examine recurrence times between events in proportional steps, as shown in Figure 3.7. Conceptually, loading the model occurs at tectonic time

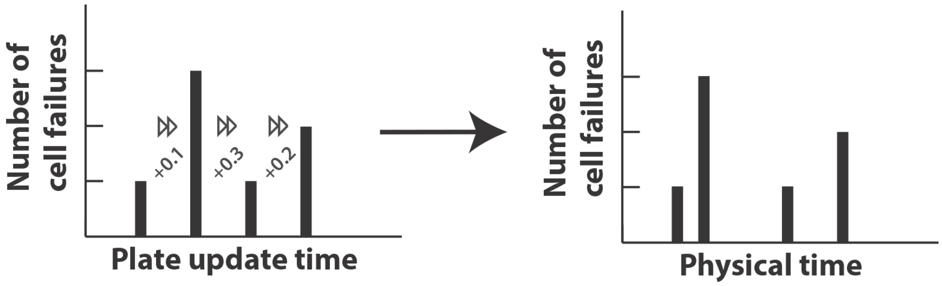

Figure 3.7: The number of cell failures as a function of plate update time t_{pu} (left) and physical time t_{phys} (right). Knowing the amount of stress $\Delta\sigma$ added at a given plate update time the events can be proportionally spaced in physical time.

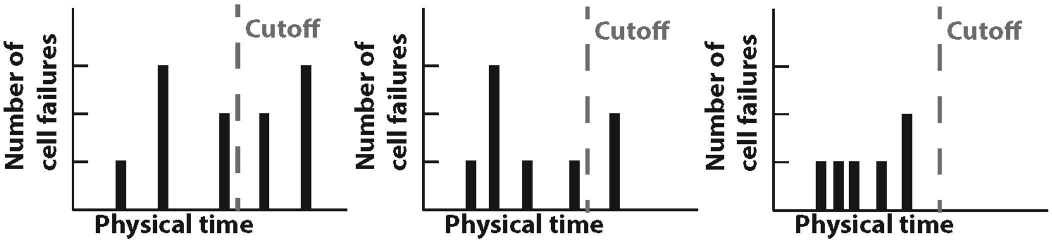

Figure 3.8: The number of cell failures as a function of physical time for three different model time series. An identical stress cutoff, dashed line, is assigned for all models so that the data is representative of identical physical time frames. Although all three models have a total of five plate updates the physical time in which they complete all plate updates is different.

scales (years), whereas the failure sequence is said to occur instantaneously (fixed time).

Furthermore, a physical time cutoff can be set between various CA models such that the data collected are representative of identical physical time rather than identical plate update times. As shown in Figure 3.8, all three models have a total of five plate updates, yet the physical time in which they complete all plate updates may differ. Assigning a physical time cutoff for all models is important in the study of seismic hazard which requires models to have a time datum.

3.1.4 Hexagonal grid versus square grid

Generally, the CA models are implemented in a square grid for simplicity as it uses the cartesian coordinates (x, y) with both axes orthogonal to each other. In our case, the model's coordinate system is arranged into a hexagonal grid through offset coordinates implemented by J. Kazemian (unpublished). Time series characteristic and time-frequency distributions are unaffected, which has been validated by running comparison tests with a square grid implementation. The advantage of using a hexagonal grid is when movement paths and connectivity are important, as the hexagonal lattice is the most compact arrangement of many equal circles (Birch et al., 2007; Patel, 2018). The arrangement of hexagonal grids can either be in vertical columns (flat topped) or horizontal rows (pointy topped) with the main difference being orientation (Patel, 2018).

For a hexagonal grid the total number of surrounding cells at a radius R is calculated as

$$N_{hex} = 3R(R+1) = 3R^2 + 3R, \tag{3.2}$$

and for a square grid as

$$N_{sqr} = (2R+1)(2R+1) - 1 = 4R^2 + 4R. \tag{3.3}$$

The square grid encompasses a greater number of surrounding cells when compared to the hexagonal grid at equal radii. Shown in Figure 3.9, is a hexagonal grid and square grid with the outline of three radii's of $R = 1, 2, 3$. The total number of surrounding cells can be made equal between both grids by increasing the radius R for the hexagonal grid. The CA scaling statistics in a square coordinate system do not significantly change for a large enough radius $R > 10$ (Gu, 2016). We also find that time-series characteristics and frequency-magnitude distributions remain unaffected between square and hexagonal grid implementations; yet the hexagonal coordinate storage leads to additional space left at the four corners of the square lattice.

At the time of writing a bug exists within the implementations of the hexagonal grid regarding the periodic boundaries. Corresponding to the center of the map, there should be six mirror boundaries rather than the four currently

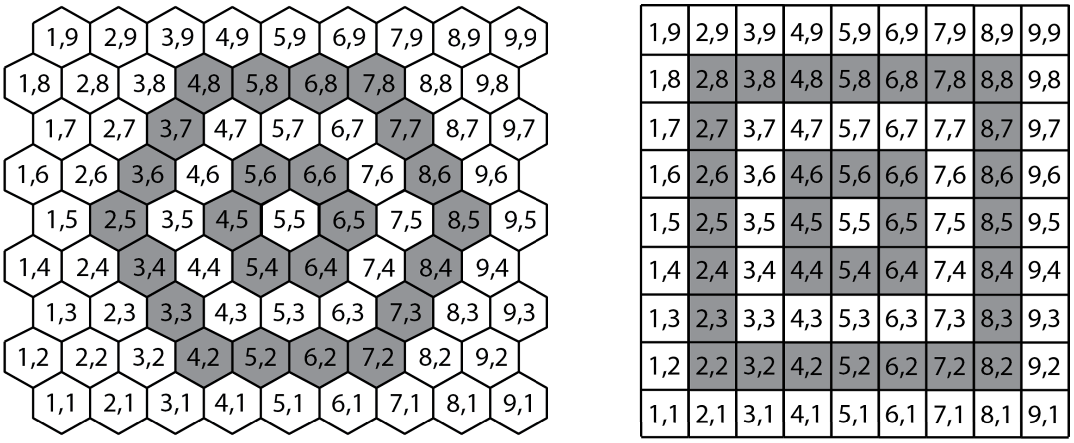

Hexagonal Grid

Square Grid

Figure 3.9: A hexagonal grid (left) and square grid (right). From the center cell (5,5) three radii's of $R = 1, 2, 3$ are outlined for both grids. The square grid encompasses a greater number of surrounding cells compared to the hexagonal grid for equal radii.

present in the square map. Therefore, the areas in questions are the corners of the square mapping used to store the coordinates of the hexagonal grid. Given that the radius R is significantly less than the length of the lattice L we expect the influence to be insignificant; this has been validated through by running comparison tests between implementations of square and hexagonal coordinate systems.

3.1.5 Back-of-the-envelope Calculations

A conceptual model can be constructed for the total number of failures $n_{tot\,cell}$ expected from a single cell interacting with itself as a function of applied external stress $\Delta\sigma$. The internal stress σ_i of an individual cell would depend on the residual threshold σ_R, failure threshold σ_F, and the stress dissipation parameter α. To initiate failure within the single cell the minimum stress difference of $\sigma_F - \sigma_i$ is added. Consequently, the single cell fails and releases its total potential stress of $\sigma_F - \sigma_R$. A fraction of the stress, given by $\alpha[\sigma_F - \sigma_R]$, is dissipated or lost. The remaining released stress, given by $(1 - \alpha)[\sigma_F - \sigma_R]$, is returned to the cell itself. Therefore, the single cell concept model does not have the dynamic interaction between neighboring cells of the CA model.

Within the CA model, the internal stress σ_i of a failed cell would be lowered to the residual threshold σ_R with the remaining stress distributed to surrounding cells.

Shown in Figure 3.10 are three single cell systems with dissipation parameters of a) $\alpha = 1.00$, b) $\alpha = 0.50$, and c) $\alpha = 0.25$. Let all three systems have residual thresholds of $\sigma_R = 0.00$ and failure thresholds of $\sigma_F = 1.00$ with the evolution of physical time t_{phys} given by the sum of the applied external stress of $\sum \Delta\sigma$. At a physical time $t_{phys} = 0$ the internal stress for the cell of each system begin at their residual thresholds $\sigma_i = \sigma_R$. At a physical time $t_{phys} = 1.00$ the cells internal stress would reach their failure threshold $\sigma_i = \sigma_F$.

Subsequently, part of the internal stress is permanently lost given by $\alpha[\sigma_F - \sigma_R]$ from the cell, shown as grey bars and arrow. The rest of the internal stress is given back to the cell. After a failure, the internal stress of a cell with a stress dissipation of $\alpha = 1.00$ always starts at the residual threshold (100% empty). Likewise, the internal stresses of cells with stress dissipation of $\alpha = 0.50$ and 0.25 start 50% and 25% empty after failure, respectively. At a physical time of $t_{phys} = 2.00$ the total number of failures for systems a) $\alpha = 1.00$ is 2, b) $\alpha = 0.50$ is 3, and c) $\alpha = 0.25$ is 5.

From Figure 3.10, once each system has reached steady state at $t_{phys} = 1.00$ the three systems follow a recursive pattern. Hence forth, the total number of failures after the external stress of $\Delta\sigma = 1.00$ for systems a) $\alpha = 1.00$ is 1, b) $\alpha = 0.50$ is 2, and c) $\alpha = 0.25$ is 4. From the conceptual model, the total number of failures $n_{tot\,cell}$ at a physical time t_{phys} is given as

$$n_{tot\,cell} = \frac{t_{phys}}{(\sigma_F - \sigma_R)\alpha}, \tag{3.4}$$

where t_{phys} is the cumulative amount of stress added, dimensionless, into the system $\sum \Delta\sigma$, α is the dissipation parameter, and σ_F and σ_R are the failure and residual thresholds, respectively. It follows that as the physical time t_{phys} increases so does the total number of cell failures $n_{tot\,cell}$, while increasing $(\sigma_F - \sigma_R)$ and dissipation parameter α decreases the total number of cell failures. In extension, the total cumulative number of failures n_{tot} over L^2 identical cells becomes

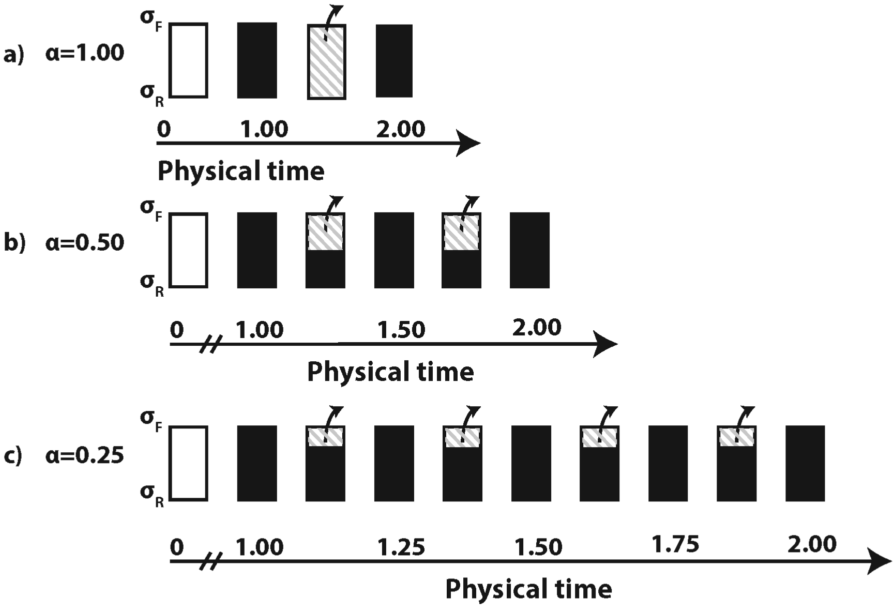

Figure 3.10: Evolution of single cell as a function of physical time, where each cell starts empty (white). Once the internal stress reaches the failure threshold σ_F part of the internal stress is permanently lost, shown as grey bars and arrow, with a part of the internal stress retained (black). If $\sigma_R = 0.00$ and $\sigma_F = 1.00$, the total number of failures after physical time $t_{phys} = 2.00$ for system a) $\alpha = 1.00$ is 1, b) $\alpha = 0.50$ is 2, and c) $\alpha = 0.25$ is 4.

$$n_{tot} = \frac{t_{phys} L^2}{(\sigma_F - \sigma_R)\alpha}. \tag{3.5}$$

The total cumulative number of failures $n_{tot\,cell}$ and n_{tot} are non-dimensional counts of the number of times cell(s) are expected to fail as a function of added stress t_{phys} or time proxy given their relative stress capacity $\sigma_F - \sigma_R$, dissipation α, and model size L^2. This sort of back-of-the-envelope calculations gives some idea of the statistics expected from the CA model.

3.1.6 Fractal dimension

The correlation integral is a measure of spatial correlation, from which the correlation exponent is a kind of fractal dimension (Grassberger and Procaccia, 1983). To quantitatively study the spatial distribution of seismic events the correlation integral $C(r)$ is calculated as

$$C(r) = \frac{2}{N(N-1)} N_r(R < r), \tag{3.6}$$

where $N_r(R < r)$ is the number of pairs whose distance R is less than r, and N is the total number of events (Hirata et al., 1987). If the distribution has a fractal structure, $C(r)$ is expressed by

$$C(r) \propto r^D, \tag{3.7}$$

where D is a kind of fractal dimension called the correlation exponent for small r and a sufficiently large number of points ($N > 100$) (Grassberger and Procaccia, 1983; Hirata et al., 1987). If the events are distributed randomly in two dimensions the fractal dimension is defined as $D = 2$ with any lesser fractal dimension indicative of clustering of events along a lineation ($D = 1$) or point ($D = 0$). We will use the D value to analyse spatial characteristics in failure patterns for both homogeneous and inhomogeneous CA models.

Chapter 4

Markov Chain Theory

4.1 Predictive Model

Understanding natural phenomena of complex systems is one of the biggest challenges as nature consists of many interacting processes in a cause-effect relationship. A set of simple rules can constitute a physical system that poses as a mystery when considered as a whole. Generally speaking, the forward process of examining model outcomes has been emphasized rather than theoretical analysis. We find that the results of a homogeneous CA model can be replicated by modeling a stochastic process with an appropriate underlying stress distribution for the system.

4.1.1 Building a Transition Matrix

Assuming that the internal stress σ_i of all cells within the lattice is uniformly distributed between the failure threshold σ_F and the residual threshold σ_R the probability density function $P(\sigma_i)$ and cumulative distribution function $D(\sigma_i)$ (Beyer, 1987) are given as

$$P(\sigma_i) = \begin{cases} 0 \text{ for } \sigma_i < \sigma_R \\ \frac{1}{\sigma_F - \sigma_R} \text{ for } \sigma_R \leq \sigma_i \leq \sigma_F \\ 0 \text{ for } \sigma_i \geq \sigma_F \end{cases} \tag{4.1}$$

$$D(\sigma_i) = \begin{cases} 0 \text{ for } \sigma_i < \sigma_R \\ \frac{\sigma_i - \sigma_R}{\sigma_F - \sigma_R} \text{ for } \sigma_R \leq \sigma_i \leq \sigma_F \\ 1 \text{ for } \sigma_i \geq \sigma_F. \end{cases} \tag{4.2}$$

The probability that the internal stress σ_i is greater than $\sigma_F - \epsilon$ is

$$P(\sigma_i > \sigma_F - \epsilon) = D(\sigma_F) - D(\sigma_F - \epsilon), \tag{4.3}$$

where ϵ is a predefined threshold. Combining Equations 4.3 and 4.2 gives

$$P(\sigma_i > \sigma_F - \epsilon) = 1 - \frac{(\sigma_F - \epsilon) - \sigma_R}{\sigma_F - \sigma_R} = \frac{\epsilon}{\sigma_F - \sigma_R}, \tag{4.4}$$

which is the probability that an internal stress σ_i is greater than $\sigma_F - \epsilon$. From the binomial distribution it is possible to determine the discrete probability distribution of having an n number of cells with internal stress of $\sigma_i > \sigma_F - \epsilon$ out of a total of N Bernoulli trials of success or failure (Papoulis and Pillai, 2002). The total number of Bernoulli trials N depends on the total number of surrounding cells within a radius R calculated as

$$N = 3R(R+1) \tag{4.5}$$

for a hexagonal lattice. The binomial distribution gives the discrete probability distribution $P_p(n|N)$ of obtaining n successes (failed cells) out of N Bernoulli trials (total surrounding cells) at a probability of success of p calculated as

$$P_p(n|N) = \frac{N!}{n!(N-n)!} p^n (1-p)^{N-n}, \text{ where } n = 0, 1..., N. \tag{4.6}$$

The probability of success p for the Bernoulli trial is determined as $p = P(\sigma_i > \sigma_F - \epsilon)$ from Equation 4.4. Essentially, the binomial distribution gives the probability that n number of cells will fail from the redistribution of ϵ units of stress to the surrounding N neighboring cells. For a single cell failure, the amount of stress uniformly redistributed to neighboring cells can be calculated as

$$\epsilon = \frac{(\sigma_F - \sigma_R)(1-\alpha)}{N} = \frac{(\sigma_F - \sigma_R)(1-\alpha)}{3R(R+1)}, \tag{4.7}$$

where σ_F, σ_R, α and R are constant predefined system parameters. But, the success probability p is not constant for each inner plate update time as it depends on the number of m cells that failed at the previous inner plate update time during an avalanche sequence. Therefore, the variable ϵ_m is the amount of stress uniformly redistributed to each neighboring cell after m number of cell failures calculated as

$$\epsilon_m = \epsilon\, m = \frac{(\sigma_F - \sigma_R)(1-\alpha)}{3R(R+1)} m, \text{ with } m = 0, 1, ..., N. \tag{4.8}$$

It is implied that no overshoot ($\sigma_i > \sigma_F$) occurs meaning that the stress released from any one cell failure is always consistent. This is a simplification of the CA model as a single cell can accumulate an internal stress larger than its failure threshold. Furthermore, within the CA model, the cells involved within the range R are slightly different between each inner plate update time t_{in}, but still overlap due to the intersection of the redistribution radii R. Additionally, the calculations for ϵ_m amount of stress uniformly redistributed given m number of cell failures assumes that the surrounding cells within the radius R do not change, thus further simplifying the CA model statistics.

The success probability depends on the amount of stress released ϵ_m at a given inner plate update time. At a given inner plate update time, the number of cell failures can range from $m = 0, .., N$, and therefore the amount of stress to be redistributed given by ϵ_m. Combining Equations 4.4 and 4.8, the probability p_m that an internal stress σ_i is greater than $\sigma_F - \epsilon_m$ becomes

$$\begin{aligned} p_m = P(\sigma_i > \sigma_F - \epsilon_m) = \frac{\epsilon_m}{\sigma_F - \sigma_R} = \\ = \frac{(1-\alpha)m}{3R(R+1)}, \text{ where } m = 0, 1, ..., N. \end{aligned} \tag{4.9}$$

Likewise, the binomial distribution of Equation 4.6 becomes

$$P_{p_m}(n|N) = \frac{N!}{n!(N-n)!} p_m^n (1-p_m)^{N-n}, \tag{4.10}$$

$$\text{where } m = 0, 1..., N \text{ and } n = 0, 1, ..., N.$$

The binomial distribution gives the discrete probability distribution $P_{p_m}(n|N)$ of obtaining n successes (failed cells) out of N Bernoulli trials (surrounding cells) at a probability of success of p_m, where p_m (Eq. 4.9) varies depending on the number of cell failures m at that given inner plate update time. Effectively, the probability of success p_m depends on the dissipation parameter α and the total number of surrounding cells within a radius R, and not the failure σ_F and residual σ_R thresholds of the system.

We can construct an $(N+1) \times (N+1)$ square transition matrix $\boldsymbol{M}$ from the binomial distributions $P_{p_m}(n|N)$ (Kemeny and Snell, 1960). Therefore, each row of the transition matrix is the discrete probability of obtaining a varied n number of failures out of a total of N trials given a fixed probability of success p_m; each column of the transition matrix is the discrete probability of obtaining a fixed n number of failures out of a total of N trials given a varied probability of success p_m.

Each i-th row and j-th column entry in the transition matrix $\boldsymbol{M}$ is calculated as

$$M_{ij} = P_{p_{i-1}}(j-1|N) = P_{p_m}(n|N), \tag{4.11}$$

$$\text{where } i = m+1 \text{ and } j = n+1,$$

and where $P_{p_m}(n|N)$ is the binomial distribution from Equation 4.10. In matrix form, the transition matrix $\boldsymbol{M}$ is given as

$$\mathbf{M} = \begin{bmatrix} P_{p_0}(0|N) & P_{p_0}(1|N) & \dots & P_{p_0}(N|N) \\ P_{p_1}(0|N) & P_{p_1}(1|N) & \dots & P_{p_1}(N|N) \\ \vdots & \vdots & \ddots & \vdots \\ P_{p_N}(0|N) & P_{p_N}(1|N) & \dots & P_{p_N}(N|N) \end{bmatrix}. \tag{4.12}$$

Each element of the transition matrix $\boldsymbol{M}$ is non-negative and each row adds to unity $\sum_j M_{ij} = 1$, being a property of the binomial distribution (Papoulis and Pillai, 2002). The transition matrix $\boldsymbol{M}$ is used to describe the transitions of a stochastic process where a process moves from state to state. If at any inner plate update time t_{in} the process is in state S_m, then on the next inner plate update time it may move to state S_n with a probability $M_{(m+1)(n+1)} = M_{ij}$.

4.1.2 Markov Chain

Let's consider a discrete-time random process $\{X_{t_{in}}, t_{in} = 0, 1, ...\}$ at an inner plate update time t_{in} within a system with a finite set of states $S_m = \{S_0, S_1, ..., S_N\}$. Therefore, each state S_m corresponds to the number of cell failures $m = 0, ..., N$ at a given plate update time. If $X_{t_{in}} = S_{m_{t_{in}}}$ then the system is in state S_m at an inner plate update time t_{in}. The functions $X_{t_{in}}$ are said to be *outcome functions* with the set of functions $\{X_{t_{in}}, t_{in} = 0, 1, ...\}$ called a *stochastic process* (Kemeny and Snell, 1960). Furthermore, if the number of states are finite in a stochastic process, then the process is called a *finite stochastic process* (Kemeny and Snell, 1960).

A *finite Markov process* is a finite stochastic process if the transition probabilities of moving to the next outcome function $X_{t_{in}+1}$ only depend on the present outcome function $X_{t_{in}}$ and not on the previous outcome functions $X_{t_{in-1}}, \ldots, X_0$ (Kemeny and Snell, 1960). This condition is referred to as the *Markov property* given a

$$\begin{aligned} Pr(X_{t_{in}+1} = S_n | X_{t_{in}} = S_m, X_{t_{in}-1} = S_{m_{t_{in}-1}}, \ldots, X_0 = S_{m_0}) = \\ = Pr(X_{t_{in}+1} = S_n | X_{t_{in}} = S_m), \end{aligned} \tag{4.13}$$

where $Pr(X_{t_{in}+1} = S_n | X_{t_{in}} = S_m)$ is the transition probability $M_{(m+1)(n+1)}(t_{in}) = M_{ij}(t_{in})$ at an inner plate update time t_{in} (Kemeny and Snell, 1960; Pishro-Nik, 2014). In other words, a Markov process only depends on the outcome of the immediate present to predict the future.

A *finite Markov chain* is a finite Markov process such that the transition probabilities $M_{ij}(t_{in})$ do not depend on the inner plate update time t_{in}, and therefore denoted by M_{ij} (Kemeny and Snell, 1960). Therefore, it is assumed that the transition matrix $\boldsymbol{M}$ is fixed and does not change with the inner plate update time, but we may choose to vary the initial probability distribution at the very first outcome function X_0 at $t_{in} = 0$.

Considering the Markov chain $\{X_{t_{in}}, t_{in} = 0, 1, ...\}$, where $X_{t_{in}} \in S = \{0, 1, ..., N\}$, and where the initial probability distribution $\boldsymbol{\pi_0}$ of the outcome function X_0 at time $t_{in} = 0$ is a row vector given as

$$\boldsymbol{\pi_0} = [Pr(X_0 = S_0)\; Pr(X_0 = S_1)\; \dots\; Pr(X_0 = S_N)]. \tag{4.14}$$

The initial probability distribution $\boldsymbol{\pi_0}$ gives the probabilities for the various starting states, whereas the transition matrix $\boldsymbol{M}$ determines how the Markov chain process will develop (Kemeny and Snell, 1960).

Let $\boldsymbol{\pi_{t_{in}}}$ be the row vector which gives the probability that the random process $X_{t_{in}}$ will be in state S_m after t_{in} number of steps given as

$$\boldsymbol{\pi_{t_{in}}} = [Pr(X_{t_{in}} = S_0)\; Pr(X_{t_{in}} = S_1)\; \dots\; Pr(X_{t_{in}} = S_N)]. \tag{4.15}$$

From the Chapman-Kolmogorov equation the induced measure of the outcome $\boldsymbol{\pi_{t_{in}}}$ for a finite Markov chain with an initial probability vector $\boldsymbol{\pi_0}$ and transition matrix $\boldsymbol{M}$ is given as

$$\boldsymbol{\pi_{t_{in}}} = \boldsymbol{\pi_0} \boldsymbol{M}^{t_{in}} \tag{4.16}$$

where $\boldsymbol{M}$ is raised to the power t_{in} (Kemeny and Snell, 1960; Pishro-Nik, 2014). Therefore, to study the outcome functions of a finite Markov chain we only need to study the powers of the transition matrix.

To better understand a Markov chain, we classify states to understand the possible directions that a stochastic process can proceed (Pishro-Nik, 2014). If it is possible to go from state S_m to state S_n, then state S_n is said to be *accessible* from state S_m. Two states S_m and S_n are said to *communicate* if they are *accessible* from each other. A Markov chain is said to be *irreducible* if all states communicate with each other.

A state is said to be *recurrent* if at any time we leave that state we will return to that state in the future with a probability one; otherwise, if the probability of returning is less than one, the state is called *transient* (Pishro-Nik, 2014). In particular, a state which when entered cannot be left is said to be *absorbing*; a chain whose recurrent states are absorbing is called an *absorbing Markov chain* (Kemeny and Snell, 1960).

4.1.3 Absorbing Markov Chain

Within the transition matrix $\boldsymbol{M}$, each i-th row represents a current state $S_{i-1} = S_m$ with the j-th column representing the probability to move to state $S_{j-1} = S_n$. It can be shown that state S_0, or row one, is a state that halts the avalanche process and acts as an inhibitor. Calculating the probability of success of p_m (Eq. 4.9) for $m = 0$, or zero failed cells, simplifies to

$$p_0 = P(\sigma_i > \sigma_F - \epsilon_0) = \frac{(1-\alpha) * 0}{3R(R+1)} = 0. \tag{4.17}$$

Subsequently, the binomial distribution for $P_{p_0}(n|N)$ (Eq. 4.10) simplifies to $P_{p_0}(0|N) = 1$ and $P_{p_0}(1, ..., N|N) = 0$, which simplifies the transition matrix $\boldsymbol{M}$ into an absorbing Markov chain in the form of

$$\boldsymbol{M} = \begin{bmatrix} 1 & 0 & \dots & 0 \\ P_{p_1}(0|N) & P_{p_1}(1|N) & \dots & P_{p_1}(N|N) \\ \vdots & \vdots & \ddots & \vdots \\ P_{p_N}(0|N) & P_{p_N}(1|N) & \dots & P_{p_N}(N|N) \end{bmatrix}. \tag{4.18}$$

In the long-term behavior of the absorbing Markov chain we would like to know the probability distribution $\boldsymbol{\pi_{t_{in}}}$ (Eq. 4.15) as $t_{in} \to \infty$, otherwise known as the *limiting distribution* (Pishro-Nik, 2014). From the Chapman-Kolmogorov equation (Eq. 4.16) the limiting distribution $\boldsymbol{\pi_{t_{in} \to \infty}}$ simplifies to

$$\lim_{t_{in} \to \infty} \boldsymbol{\pi_{t_{in}}} = \boldsymbol{\pi_0} \boldsymbol{M}^{t_{in}} =$$

$$= [Pr(X_{t_{in}} = S_0)\ Pr(X_{t_{in}} = S_1)\ \dots\ Pr(X_{t_{in}} = S_N)] = [1\ 0\ \dots\ 0], \tag{4.19}$$

meaning that regardless of the initial probability distribution $\boldsymbol{\pi_0}$ the Markov chain will be absorbed into state S_0 with a probability 1 and stay there for all dissipation parameters between $0 < \alpha \leq 1$. Hence, raising the transition matrix $\boldsymbol{M}$ (Eq. 4.18) to greater and greater powers, the matrices approach a matrix whose first column are all 1, and 0 elsewhere.

All the possible outcomes can be presented as a *tree* with each Markov chain a possible *path* through the tree, and each path made of segments called *branches* (Kemeny and Snell, 1960). The transition probabilities at each branch are called *branch probabilities* (Kemeny and Snell, 1960).

Once the Markov chain is absorbed into state S_0 at an arbitrary inner plate update end time t_{end} the *path probability* P_{path} can be calculated as the product of all branch probabilities given as

$$P_{path} = \prod_{t_{in}=0}^{t_{end}} Pr(X_{t_{in}+1} = S_n | X_{t_{in}} = S_m), \tag{4.20}$$

where the branch probability $Pr(X_{t_{in}+1} = S_n | X_{t_{in}} = S_m)$ is simply the transition probability $M_{(m+1)(n+1)} = M_{ij}$ (Kemeny and Snell, 1960). It follows that the sum of all branch probabilities, or all possible outcomes, must be one.

Lastly, the cumulative number of failures S_{cum} for a Markov chain is the sum of all states $S_{m_{t_{in}}}$ traversed at an inner plate time t_{in} until being absorbed into state S_0 at an inner plate update end time t_{end}. It is calculated as

$$S_{cum} = \sum_{t_{in}=0}^{t_{end}} S_{m_{t_{in}}}. \tag{4.21}$$

4.2 Application of Markov Chains

Effectively, the transition matrix can be used to simulate the stochastic process based on underlying CA model parameters. At the start of each inner plate $t_{in} = 0$ of the CA model a single event $m = 1$ is induced within the entirety of the system, which is equivalent to starting in state S_1, row two, within the transition matrix. Thereafter, identical to the CA model, the stress redistributed to the surrounding N neighboring cell is ϵ_1 (Eq. 4.8) with a probability of p_1 (Eq. 4.9) that an internal stress σ_i is greater than $\sigma_F - \epsilon_1$.

Given the binomial distribution $P_{p_1}(n|N)$ (Eq. 4.10) with a probability p_1 for $n = 0, 1, ..., N$ Bernoulli trials a single outcome of n number of failed cells will occur at the next inner plate update time $t_{in} = t_{in} + 1$. But, rather than re-calculating the binomial distribution $P_{p_m}(n|N)$ for the varying preceding failures m and induced failures n, all of the possible transitions are tabulated into the transition matrix $\boldsymbol{M}$.

Therefore, the process starts at $t_{in} = 0$ in state S_1 with an induced event of size $m = 1$ with the transition probabilities given by the row $M_{1,j}$ for all columns j. Given the succeeding number of failed cells n the process moves into state S_n with a transition probability $M_{1,(n+1)}$. At an inner plate update time of $t_{in} = 1$, the process is now in state S_n and can move into another state with transition probabilities given by the row $M_{(n+1),j}$ for all columns j. This process is continued until reaching state S_0 or row 1; state S_0 is an absorbing state with all other states $S_1, \ldots, S_N$ being transient states.

4.2.1 Example

As an example, let us consider a homogeneous hexagonal system defined by the system parameters of $\sigma_F = 1$, $\sigma_R = 0$, $\alpha = 0.05$, and $R = 1$. Within the CA model, σ_F and σ_R correspond to the failure and residual thresholds of a cell, respectively, with α being the dissipation parameter of the system. The stress transfer radius is set to $R = 1$, or a one neighboring cell radius, to keep the size of the transition matrix $\boldsymbol{M}$ at a minimum.

From Equation 4.5, the total number of surrounding cells N within a radius of $R = 1$ is $N = 6$. Given the number of surrounding cells, the total number of potential cells failures m at a given inner plate update time cannot exceed $N = 6$. Therefore, the set of all possible states S_m at a given inner plate update time range from $S_m = \{S_0, S_1, ..., S_6\}$.

The amount of stress uniformly redistributed to each neighboring cell ϵ_m (Eq. 4.8) after any m number of cell failures simplifies to

$$\epsilon_m = \frac{(\sigma_F - \sigma_R)(1-\alpha)}{3R(R+1)} m = \frac{(1-0)(1-0.05)}{3(1+1)} m = \frac{0.95}{6} m, \tag{4.22}$$

where $m = 0, 1, ..., 6$. Given an internal stress σ_i uniformly distributed between

σ_F and σ_R the probability p_m that $\sigma_i > \sigma_F - \epsilon_m$ (Eq. 4.9) is calculated as

$$p_m = \frac{(1-\alpha)m}{3R(R+1)} = \frac{(1-0.05)m}{3(1+1)} = \frac{0.95m}{6}, \tag{4.23}$$

where $m = 0, 1, ..., 6$. As a side note, the probability of success p_m is independent of the failure σ_F and residual σ_R thresholds of the system. The binomial distribution (Eq. 4.10) becomes

$$P_{p_m}(n|N) = \frac{N!}{n!(N-n)!} p_m^n (1-p_m)^{N-n} = \frac{6!}{n!(6-n)!} p_m^n (1-p_m)^{6-n}, \tag{4.24}$$

for the probability of success p_m for $m = 0, 1..., 6$ given failures and $n = 0, 1..., 6$ potential failures. Each element of the transition matrix M_{ij} is calculated from the binomial distribution $P_{p_m}(n|N)$ (Eq. 4.11), where the probability of success (cell failure) p_m given m previous cell failures varies row wise and the number of potential cell failures n varies column wise.

Given the system parameters of $\sigma_F = 1$, $\sigma_R = 0$, $\alpha = 0.05$, and $R = 1$, the binomial distribution is given by Equation 4.24. Every element of the transition matrix M_{ij} is calculated from the binomial distribution $P_{p_m}(n|N)$ (Eq. 4.24) for every m given cell failures (row) and n potential cell failures (column) and is approximately

$$\boldsymbol{M} = \begin{bmatrix} 1 & 0 & 0 & 0 & 0 & 0 & 0 \\ 0.35 & 0.40 & 0.19 & 0.05 & 0.01 & 0 & 0 \\ 0.10 & 0.28 & 0.33 & 0.21 & 0.07 & 0.01 & 0 \\ 0.02 & 0.11 & 0.26 & 0.31 & 0.21 & 0.08 & 0.01 \\ 0 & 0.03 & 0.11 & 0.26 & 0.32 & 0.22 & 0.06 \\ 0 & 0 & 0.02 & 0.09 & 0.26 & 0.39 & 0.24 \\ 0 & 0 & 0 & 0 & 0.03 & 0.23 & 0.74 \end{bmatrix}, \tag{4.25}$$

where individual values of M_{ij} have been rounded for clarity. Within the transition matrix $\boldsymbol{M}$, each state S_m is a row, where row one is the absorbing state S_0 and all other rows are transient states $S_1, \ldots, S_6$. To visualize the possible

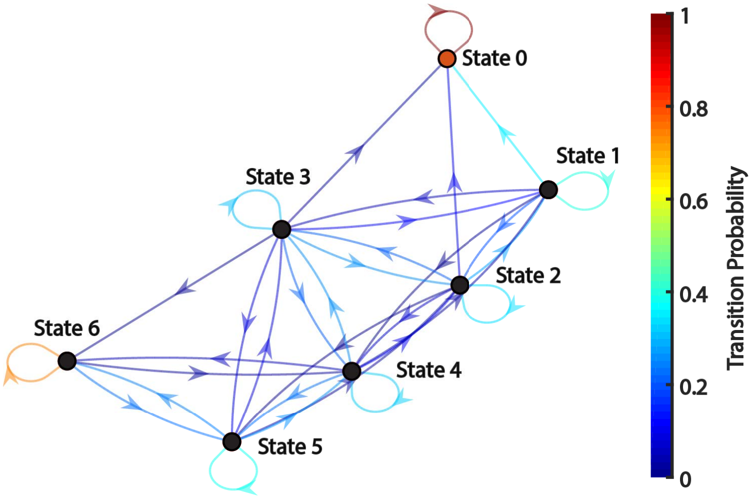

Figure 4.1: A directed graph of a Markov transition matrix (Eq. 4.25) with a total of 7 states. State S_0 is an absorbing state, red circle, with states $S_2, \ldots, S_6$ being transient states, black circles. The transition probabilities are shown in the colorbar ranging from low probability (dark blue) to high probability (dark red).

transitions a directed graph of the Markov chain is shown in Figure 4.1 with state S_0 being an absorbing state, red circle, and states $S_1, \ldots, S_6$ being transient states, black circles. The transition probabilities are shown in the colorbar ranging from low probability (dark blue) to high probability (dark red).

Consider the absorbing Markov chains shown in Figure 4.2 as possible outcomes. In step 0, all Markov chains start in state S_1 which is equivalent to starting with one failure to reproduce the processes of the CA model. Hence forth, given the probabilities from the transition matrix $\boldsymbol{M}$ a succeeding number of states S_m, or m failures, are realized until the Markov chain is terminated at state S_0.

As the Markov chain gets longer the branch probability P_{path} decreases; therefore, the probability of having a greater number of cumulative failures S_{cum} decreases. Furthermore, there are multiple paths to an identical cumulative number of failures. As shown in Figure 4.2, the third and fourth Markov chains have cumulative failures of three, yet the third Markov chain sequence of $\{S_1, S_1, S_1, S_0\}$ is nearly three times more likely than the fourth Markov chain $\{S_1, S_2, S_0\}$.

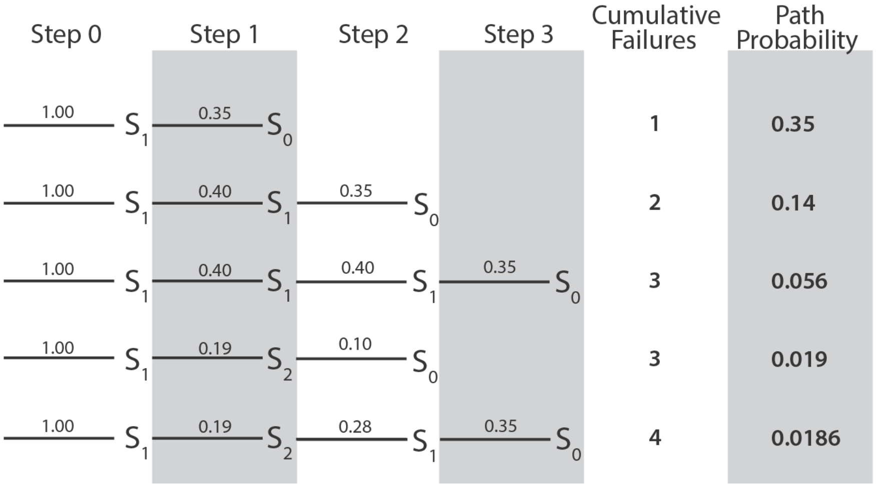

Figure 4.2: Five possible absorbing Markov chains from the transition matrix $\boldsymbol{M}$ (Eq. 4.25). In step 0, all absorbing Markov chains start in state S_1 and continue until they terminate at state S_0. Shown are the branch probabilities for each segment, along with the cumulative failures and path probabilities for each path.

4.3 Frequency-Size Probability Distribution

4.3.1 Predicting Homogeneous Models

The interest of studying CA models stems from the existence of a universal Gutenberg-Richter like scaling consistent with those observed of real earthquake fault systems (Tiampo et al., 2007). For the CA models, model statistics are gathered over a large simulation runtime known as plate update times. In theory, it is possible to construct an analytical frequency-size probability distribution from the absorbing Markov chains.

Given that all absorbing Markov chains are finite there are also a finite number of paths that sum to a specific cumulative number of failures S_{cum} (Eq. 4.21). The probability that a cumulative number of failures $P(S_{cum})$ will occur is the sum of all path probabilities P_{path} (Eq. 4.20) for that specific number of failures S_{cum} calculated as

$$P(S_{cum}) = \sum P_{path}(S_{cum}). \tag{4.26}$$

As an example, Figure 4.3 shows all possible paths up to a cumulative

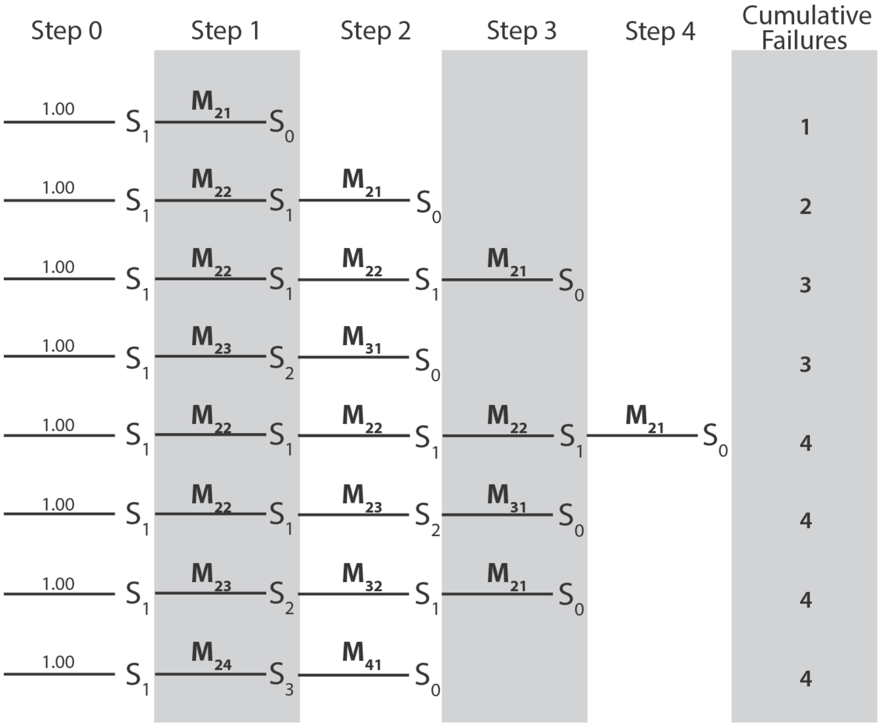

Figure 4.3: All possible paths up to a cumulative number of failures $S_{cum} = 4$. In step 0, all absorbing Markov chains start in state S_1 and continue until they terminate at state S_0. The branch probabilities for each segment M_{ij} and cumulative failures for each path S_{cum} are shown.

number of failures $S_{cum} = 4$. In step 0, all absorbing Markov chains start in state S_1 and continue until they terminate at state S_0. The branch probabilities for each segment are given from the transition matrix M_{ij}. Summing over all path probability P_{path} (Eq. 4.26) for a given cumulative number of failures S_{cum} (Eq. 4.21) gives the probability $P(S_{cum})$ (or frequency) that a given cumulative number of failures S_{cum} (or size) occurs.

Therefore, one simply needs to compute all integer partitions and permutations of a given cumulative number of failures S_{cum}. Unfortunately, calculating all partitions and permutations for a large cumulative number of failures quickly becomes computationally expensive. Therefore, the analytical frequency-size probability distribution is limited to the low cumulative number of failures of say $S_{cum} \leq 17$.

To get the frequency-size distribution for the homogeneous models one simply multiplies the analytically calculated frequency-size probability distribution

$P(S_{cum})$ by the total number of simulated plate update times t_{pu} given as

$$n_s = P(S_{cum}) \times t_{pu} = P(s) \times t_{pu}, \tag{4.27}$$

where n_s is the count of events of size s; the size s is the shorthand notation for the cumulative number of failures S_{cum} that occur within one plate update time with n_s being the shorthand notation for the non-cumulative count of failed cells of size s (Klein et al., 2000, 2007). Therefore, from the transition matrix $\boldsymbol{M}$ we can calculate the frequency-size distribution given any constant (homogeneous) system parameters of σ_F, σ_R, α, and R. But what if our model is a mixed system with cells that vary in σ_F, σ_R, and α? Below, we discuss how to predict such mixed models assuming a fixed stress transfer radius R.

4.3.2 Predicting Mixed Models

In order to get the frequency-size distribution for mixed model, we consider the mixed (inhomogeneous) model as the sum of individual and independent homogeneous models. In other words, the inhomogeneous model is the sum of independent homogeneous parts. Although a simplistic approach, this allows us to examine the influences that may originated from different submodels interacting with each other.

An issue that arises is that the analytical frequency-size distribution determined from the transition matrix $\boldsymbol{M}$ is for a homogeneous model with constant dissipation parameter α, stress transfer radius of R, and failure σ_F and residual σ_R thresholds. Whereas, when an inhomogeneous model consists of homogeneous subsystems the effective number of plate updates t_{pu} simulated for each homogeneous subsystem should vary depending on their seismogenic contribution. Therefore, the effective number of plate updates t_{pu} that each homogeneous subsystem is simulated for varies depending on their representative size L^2, and their failure σ_F and residual σ_R thresholds. Utilising an effective number of plate updates to simulate each homogeneous subsystem is needed because each subsystem may complete an equal amounts of plate updates t_{pu}, but within different physical time t_{phys} frames.

Given a n finite number of homogeneous subsystems, we calculate a transition matrix $\boldsymbol{M}$ and a frequency-size probability distribution $P_1(s), \ldots, P_n(s)$ for every homogeneous subsystem as discussed in the previous section. Additionally, we need to calculate appropriate contributions or weights $w_1, \ldots, w_n$ for every n homogeneous subsystem given that subsystem parameters (σ_F, σ_R, α) vary. The mixture probability density function $P_{mix}(s)$ is given as

$$P_{mix}(s) = \sum_{i=1}^{n} w_i P_i(s), \tag{4.28}$$

where w_i are the weights and $P_i(s)$ the frequency-size probability distribution for the i-th homogeneous subsystem. We calculate the fraction of size f_i that the i-th homogeneous subsystem represents from the whole system given as

$$f_i = \frac{L_i^2}{L^2}, \tag{4.29}$$

where L_i^2 is the size of the subsystem divided by the total system size L^2. To account for the differences in the failure σ_{F_i} and residual σ_{R_i} thresholds for the i-th homogeneous subsystem, we calculate the relative failure ratio r_i given as

$$r_i = \frac{min(\sigma_F - \sigma_R)}{\sigma_{F_i} - \sigma_{R_i}}, \tag{4.30}$$

where $min(\sigma_F - \sigma_R)$ is the lowest difference in the failure and residual thresholds from all n homogeneous subsystems. Each ratio r_i is calculated relative to a baseline $min(\sigma_F - \sigma_R)$ value, since subsystems with greater differences in the failure and residual thresholds would not contribute as significantly in the mixture probability density function $P_{mix}(s)$. Therefore, the weight w_i for the i-th subsystem is calculated by multiplying both the fraction of size f_i (Eq. 4.29) and relative failure ratio r_i (Eq. 4.30) which simplifies to

$$w_i = f_i r_i = \frac{L_i^2 \, min(\sigma_F - \sigma_R)}{L^2[\sigma_{F_i} - \sigma_{R_i}]}. \tag{4.31}$$

The calculated weight w_i is not a function of the dissipation parameter α, as it is already accounted for in the transition matrix $\boldsymbol{M}$ and in extension the analytical frequency-size distribution $P_i(s)$ of the i-th homogeneous model. To get the frequency-size distribution for the inhomogeneous models, we multiply the mixture probability density function $P_{mix}(s)$ (Eq. 4.28) by the total number of simulated plate updates t_{pu} which simplifies to

$$n_s = P_{mix}(s) \times t_{pu} = t_{pu} \sum_{i=1}^{n} w_i P_i(s) = t_{pu} \sum_{i=1}^{n} \frac{L_i^2 \, min(\sigma_F - \sigma_R)}{L^2[\sigma_{F_i} - \sigma_{R_i}]} P_i(s), \quad (4.32)$$

where n_s is the count of events of size s for the inhomogeneous model. Therefore, if all of the failure σ_F and residual σ_R thresholds are equal between models the assigned weights only dependent on the fraction of size f_i. But, if differences exist in the relative failure ratio r_i of the models, then an additional weighting is assigned based on the given model's hardness $\sigma_{F_i} - \sigma_{R_i}$ relative to a baseline model's hardness $min(\sigma_F - \sigma_R)$.

The analytical size-frequency distributions $P(s)$ or $P_{mix}(s)$ are limited to low sizes $s \leq 17$, nonetheless low cumulative number of failures are more statistically probable compared to larger number of failures. This is because the transition matrix $\boldsymbol{M}$ has a single absorbing state S_0 with all other transition probabilities between states S_m occurring with a probability of less than one. It follows that as the Markov chain gets longer the path probability P_{path} (Eq. 4.20) decreases. To obtain a more complete frequency-size distribution an alternative sampling method is needed.

4.4 Markov Chain Monte Carlo

We utilize a Markov chain Monte Carlo (MCMC) method to repeatably sample absorbing Markov chains from the binomial distribution $P_{p_m}(n|N)$, or equivalently the transition matrix $\boldsymbol{M}$, to simulate the time series of the total cumulative cell failures S_{cum} per plate update time t_{pu}. The Markov chain Monte Carlo algorithm is implemented as follows.

Firstly, the system parameters $\sigma_F, \sigma_R, R, \alpha, t_{pu}$ are specified, where σ_F and σ_R are the failure and residual thresholds, R is the cell radius for stress transfer, α the dissipation parameter, and t_{pu} the total number of plate update times to be simulated. From the cell radius R, the total number of surrounding cells N is calculated (Eq. 4.5). Within each plate update t_{pu} a single failure $m = 1$ is initiated, equivalent to starting the Markov chain in state S_1.

Given the current number of failures m, the probability of success p_m (Eq. 4.9) is calculated. The binomial distribution $P_{p_m}(n|N)$ with parameters specified by the number of trials N, and probability of success p_m for all n trials is computed. From the computed binomial distribution $P_{p_m}(n|N)$ a random sample for the new number of failures m is generated; the probability of occurrence $P_{p_m}(m|N)$ (transition probability) given the new failure m is calculated. We update the Markov chain $\{S_1, ..., S_m\}$ and move to the next inner plate update time $t_{in} = t_{in} + 1$ until the number of failures is $m = 0$ and the Markov chain has been absorbed into state S_0.

Once the Markov chain has reached state S_0, the cumulative number of failures S_{cum} (Eq. 4.21) and path probability P_{path} (Eq. 4.20) are calculated for the final absorbed Markov chain $\{S_1, ..., S_0\}$.

If the total number of plate update times t_{pu} to be simulated has not been reached, a new plate update time is started, and the entire process is repeated. A question that arises in reference to the CA model, how much physical time t_{phys} passes between each plate update time t_{pu}? Knowing the amount of stress added $\Delta\sigma$ at each plate update time t_{pu} allows for the examination of the recurrence times between events in proportional time steps.

At a given plate update time within the CA model, $\Delta\sigma = min(\sigma_F - \sigma_i)$ units of stress is added to each cell to initiate a single failure event. Therefore, the $\Delta\sigma$ units of stress added is the total minimum amount of stress sampled from the L^2 number of cells within the entire system. Replicating this process for the Markov chain Monte Carlo algorithm, we sample L^2 random internal stresses σ_i from the probability density function of $P(\sigma_i)$ (Eq. 4.1). From the total L^2 samples of σ_i, the stress added at that particular plate update time is given as $\Delta\sigma = \sigma_F - max(\sigma_i)$. Lastly, the flowchart for the Markov chain Monte Carlo algorithm is summarized in Figure 4.4.

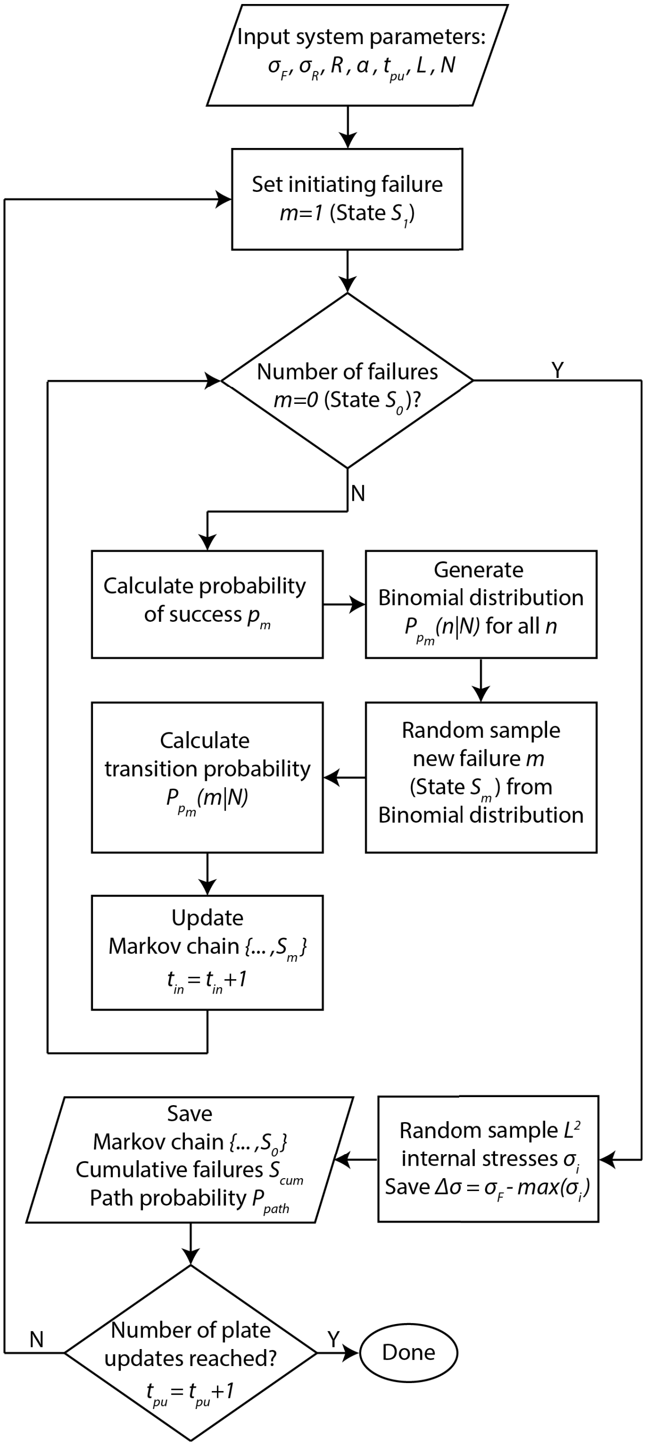

Figure 4.4: Flowchart of the Markov Chain Monte Carlo algorithm. The absorbing Markov chain $\{S_1, ..., S_0\}$ is built by repeatedly random sampling from the binomial distribution $P_{p_m}(n|N)$ for each inner plate update time t_{in} until reaching the absorbing state S_0. This process is repeated for a predefined number of plate update times t_{pu}.

Chapter 5

Cellular Automaton Homogeneous Results

In this chapter, we examine homogeneous CA models for varied dissipation parameters α (elastic ratios) that define the stress transfer to neighboring cells after a failure. Varying the dissipation parameter of the system affects the scaling exponent, or slope, of the frequency-size distribution. Examining the homogeneous CA model results allows us to validate our implementation with others and with our proposed Markov chain (MC) model.

Furthermore, we investigate system details such as the internal stress distribution, avalanche sequences, spatial clustering, and model expectancies. An accurate understanding of the internal stress distribution of the CA model is crucial in modeling the Markov process. Examining the avalanche sequences and spatial clustering of events offers insight into how an earthquake may evolve. Lastly, the model expectancies serve as a basic conceptual validation.

5.1 Homogeneous Model

In this section, we examine the results for our homogeneous CA model. The 2-D model is a square lattice with a length of $L = 256$ cells with periodic boundary conditions. For all cells, the failure threshold is set to $\sigma_F = 1.0$ with a residual threshold of $\sigma_R = 0.0 \pm \eta$, where η is a random uniformly distributed noise between $\eta = [-0.1, +0.1]$. The long range stress redistribution radius is $R = 16$, meaning that every failed cell uniformly transfers stress to $N = 816$ neighbours (Eq. 3.2) within a hexagonal implementation. We find that increasing the long range stress redistribution R beyond $R > 16$ does not make the power law scaling significantly better, as noted by Gu (2016) as well, while significantly increasing computational time required to run the model.

We simulate the model for a wide range of chosen dissipation parameters α, where $\alpha = 0.05$, 0.10, 0.20, 0.40, 0.60, 0.80, and 1.00. Examining a range of different values of α allows us to later compare the CA model to the proposed MC model. Prior to simulation, the internal stresses of each cell are uniformly randomly distributed between $-\eta < \sigma_i < \sigma_F$. Afterwards, the system was simulated for 2×10^6 plate updates to remove any transient effects before recording the size, or number of failed cells, for the next 10^6 plate updates. All model statistics reported are after this 2×10^6 burn-in period.

5.1.1 Time Series

A snippet of the time series up to $t_{phys} = 1$ is shown in Figure 5.1 for different dissipation parameters α. From the time series, as the dissipation parameter increases from $\alpha = 0.05$ (Fig. 5.1 top subplot) to $\alpha = 1.00$ (Fig. 5.1 bottom subplot) the average size of an event decreases. For all cases, the time series events remain random and unpredictable with no signs of foreshock and aftershock sequences prior to a large sized event, a seismic property that has been observed in nature (Omori, 1894; Utsu et al., 1995). With no diagnostic precursor or seismic activity prior to a random large event, forecasting is impractical. This is in accordance with the original BK model where aftershocks were introduced into the numerical model through a viscous region that created time delayed shocks between two fault regions (Burridge and Knopoff, 1967) or as some form of heterogeneities present in CA models (De Rubeis et al., 1996; Castellaro and Mulargia, 2001; Kazemian et al., 2015).

Table 5.1 summarizes the total stress, or physical time, required for all models to complete 10^6 plate updates along with the total plate updates completed given the physical time cutoff of $t_{phys} = 15.2101$. From Table 5.1, one expects

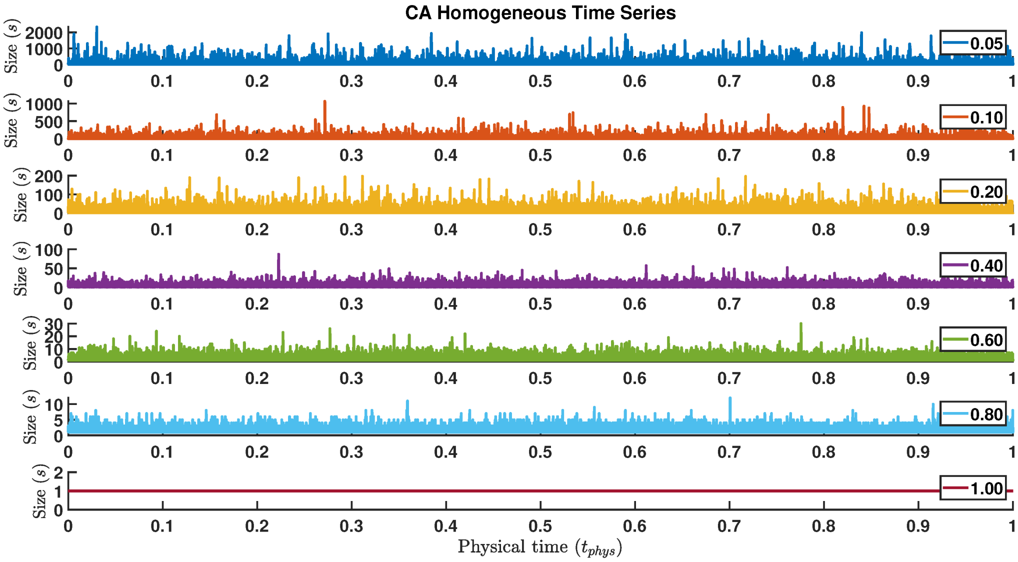

Figure 5.1: Physical time series of events (number of failed cells) for varied dissipation parameters, shown in legend, over 1 unit of physical time. From top to bottom, as the dissipation parameter α increases the size of events decreases.

that as the dissipation parameter α increases so should the total physical time needed to complete an equivalent number of plate updates. This is because a system with a lower dissipation parameter should be closer to failure relative to a more dissipative system. Discrepancy in the total physical time needed to complete all 10^6 plate updates for different dissipation parameters is expected due to the stochastic nature of the process and should decrease as the model runtime is increased.

5.1.2 Frequency-Size Distribution

The non-cumulative frequency-size distributions for all of the homogeneous models are shown in Figure 5.2, along with the theoretical OFC model for mean-field scaling, plotted as a black line, given as $n_s \sim s^{-3/2}$ for long range interaction ($R \gg 1$) and low dissipation parameters ($\alpha \to 0$) (Klein et al., 2000, 2007). In plotting the non-cumulative frequency-size distributions an identical physical time cutoff ($t_{phys} = 15.2101$) was used for all models, which gives fair comparison between their seismogenic index (intercept).

The non-cumulative frequency-size distribution is a log-log scale histogram

Dissipation parameter α	Total physical time for 10^6 plate updates	Total plate updates for $t_{phys} = 15.2101$
0.05	15.2101	1,000,000
0.10	15.2338	998,415
0.20	15.2560	996,953
0.40	15.2551	997,011
0.60	15.2653	996,293
0.80	15.2600	996,711
1.00	15.2585	996,770

Table 5.1
Total stress added, proportional to physical time, to each homogeneous CA model over 10^6 plate updates and the total number of plate updates completed given a physical time cutoff of $t_{phys} = 15.2101$.

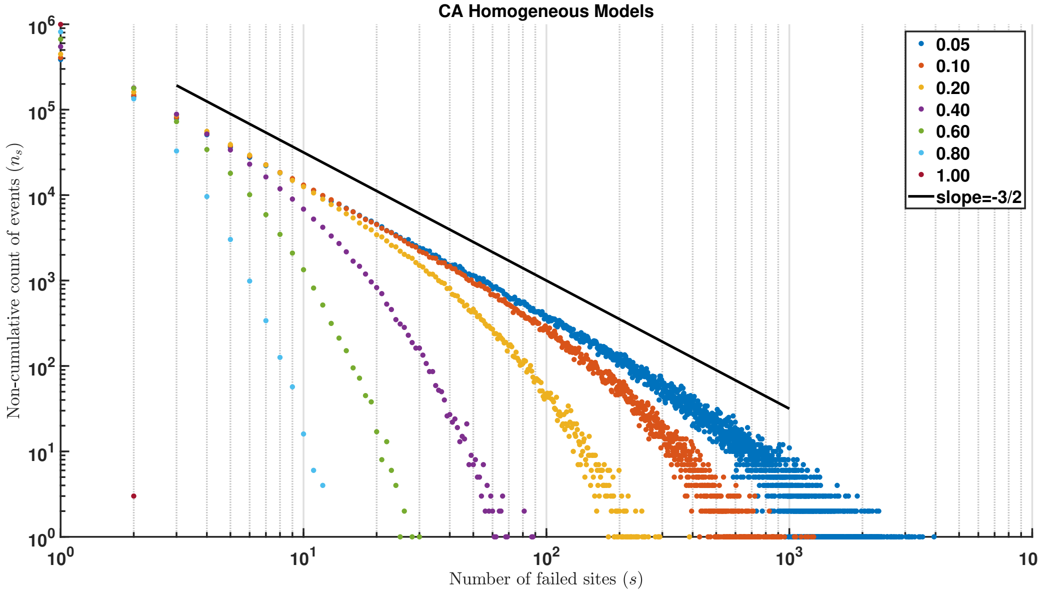

Figure 5.2: Non-cumulative frequency-size distribution for varied dissipation parameters α increasing from right to left. The distributions suggest that as the dissipation parameter increases both the intercept and slope increase. The black line has a slope of $-3/2$ predicted from the scaling of OFC models with low dissipation and long range interactions.

with integer bin sizes (x-axis) with the measure of frequency given as counts (y-axis). The log-linear slope, otherwise known as *b*-value, gives the proportionality of large to small events; a large slope indicates more similar sized events, while a small slope indicates a larger range of sizes. Because the data from all models is over equal periods of time (physical time cutoff) the intercept, or *a*-value, gives the seismogenic index or frequency of small sized events. Unlike earthquake catalogues, the numerical data do not suffer from magnitude of completeness, which is a minimum magnitude above which it is thought that all earthquakes are recorded reliably (above background noise) (Naylor et al., 2010).

As the dissipation parameter α increases, we observe an increase in the slope from $-3/2$ towards $-5/2$ (*b*-value) and an increase in the intercept (*a*-value) in Figure 5.2; therefore, we observe a decrease in the maximum expected size (magnitude) with an increase in small size events. A higher stress dissipation suppresses the occurrence of large sized events since a greater fraction of potential stress is lost from the system, while a low dissipation approaches the mean-field scaling plotted as the black line (Klein et al., 2007).

In the limit of $\alpha = 1.00$, we find each event size equals one with essentially a probability of one (Fig. 5.1 and 5.2) because all stress is dissipated after a plate update time with the algorithm bringing the cell with the highest internal stress concentration to failure in the next iteration.

Figure 5.2 shows an exception since an event of size two $s = 2$ exists indicating that two cells had failed at a given plate update time. Likely, both cells had identical internal stresses σ_i, or a difference less than machine precision, such that adding $min(\sigma_F - \sigma_i)$ at the beginning of a plate update failed both cells. This phenomenon has also been noted by others (Klein et al., 2000).

Another way of examining the data is by plotting the interevent times with the mean physical times (y-axis) between events of size s (x-axis) on a log-log scale, as shown in Figure 5.3. Whereas the non-cumulative frequency-size distribution plots the count of an event of size s, the interevent plot shows the mean physical time $\bar{t}_s$ between events of size s for all 10^6 plate updates. In Figure 5.3, the solid color curve is the mean interevent physical time $\bar{t}_s$, with the top and bottom dashed lines showing the third ($Q3$) and first ($Q1$) quantiles,

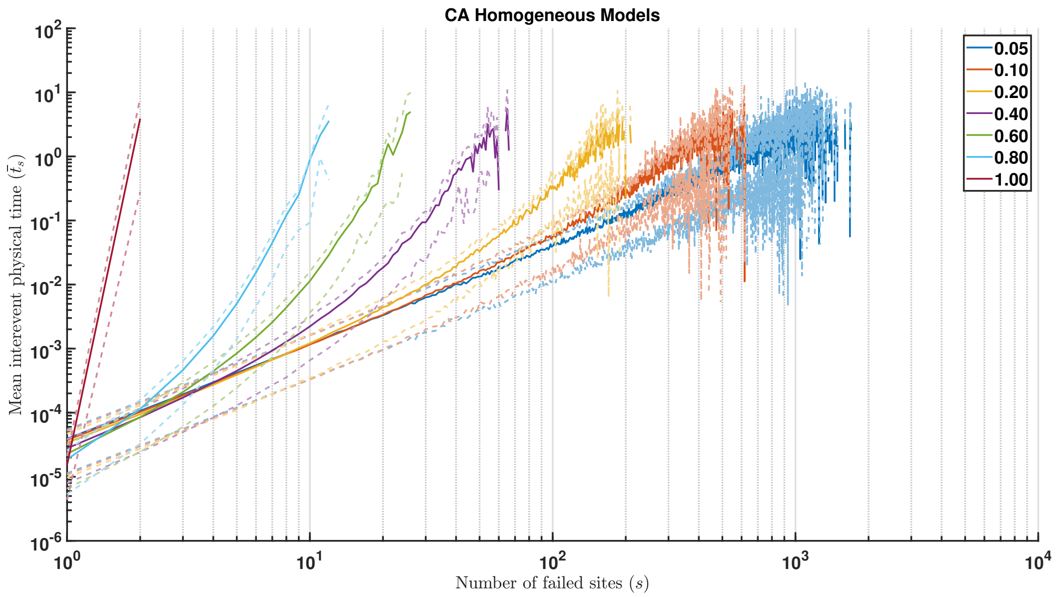

Figure 5.3: Mean interevent physical time $\bar{t}_s$ between events of size s for varied dissipation parameters. Top and bottom dashed lines are the third and first quartiles, respectively, for a given curve. As the dissipation parameter increases the mean interevent physical time $\bar{t}_s$ for a given sized event s increases.

respectively, for that given curve. For sparse data, particularly the tail end of the curve, the calculated mean interevent physical time and quantiles have lots of variability and gaps in data.

Generally, the mean interevent physical time (or period) increases as the event size s increases for all models. Likewise, the interevent physical time $\bar{t}_s$ for the largest size events is similar for all models although the actual maximum observed size increases with decreasing dissipation parameter α. More specifically, the mean physical time between events of size $s < 10$ decreases as the dissipation parameter α increases. But, for event sizes of $s > 10$ the mean physical time decreases as the dissipation parameter decreases. Therefore, a high dissipation system has an increased occurrence of small sized events with a reduced occurrence of larger sized events. The opposite occurs for a low dissipation system, where there is a reduced occurrence of small sized events with an increased occurrence of larger sized events. This observation also explains the change in the slope (b-value) for the non-cumulative magnitude-size distributions (Fig. 5.2).

5.2 System details

Additionally, at the end of every 500-th of the total 10^6 plate updates we output a snapshot of the internal stresses of all cells and the lattice's inner plate failure sequence t_{in}; furthermore, we output the cumulative failures of each cell within an interval of 500 plate updates. Therefore, we have an idea of the internal stress distribution as the system evolves, how an avalanche sequence might develop spatially and the cumulative number of failures for every cell. This gives us 2×10^3 snapshots from the total 10^6 plate updates.

5.2.1 Internal Stress Distribution

Shown in Figure 5.4, are the internal stress snapshots, left subplot, and the resulting histogram, right subplot, for models with dissipation parameters of $\alpha =$ a) 0.05, b) 0.20, and c) 0.80, from top to bottom. Regardless of the dissipation parameter, the internal stress distribution is approximately uniformly distributed between $\sigma_R + \eta < \sigma_i < \sigma_F$ $(0.1 < \sigma_i < 1.0)$ as shown on the histograms. A sloping trend is observed between $\sigma_R - \eta < \sigma_i < \sigma_F$ $(-0.1 < \sigma_i < +0.1)$ since a cell's internal stress σ_i is set to $\sigma_i = \sigma_R \pm \eta$ after a failure, where η is a uniformly distributed random number. Therefore, the residual stress σ_R of a cell after failure is governed by the distribution from which η is sampled.

Due to the stochastic nature of the CA model, there are deviations from a uniform internal stress distribution since the histogram is for a single plate update time. Shown in Figure 5.5, are the cumulative or stacked histograms of the internal stresses for models with dissipation parameters of $\alpha = 0.05, 0.20, 0.80$ across all 2×10^3 snapshots. Although not included, the same internal stress distributions were noted for all other homogeneous models ($\alpha =$ 0.05, 0.10, 0.20, 0.40, 0.60, 0.80, and 1.00).

Physically, we expect that a system with a lower dissipation parameter ($\alpha = 0.05$) distributes a larger amount of internal stresses between neighbouring cells compared to a system with a greater dissipation parameter ($\alpha = 1.00$) because less stress is removed in each plate update time. Yet, regardless of the dissipation parameter α the underlying internal stress distribution remains

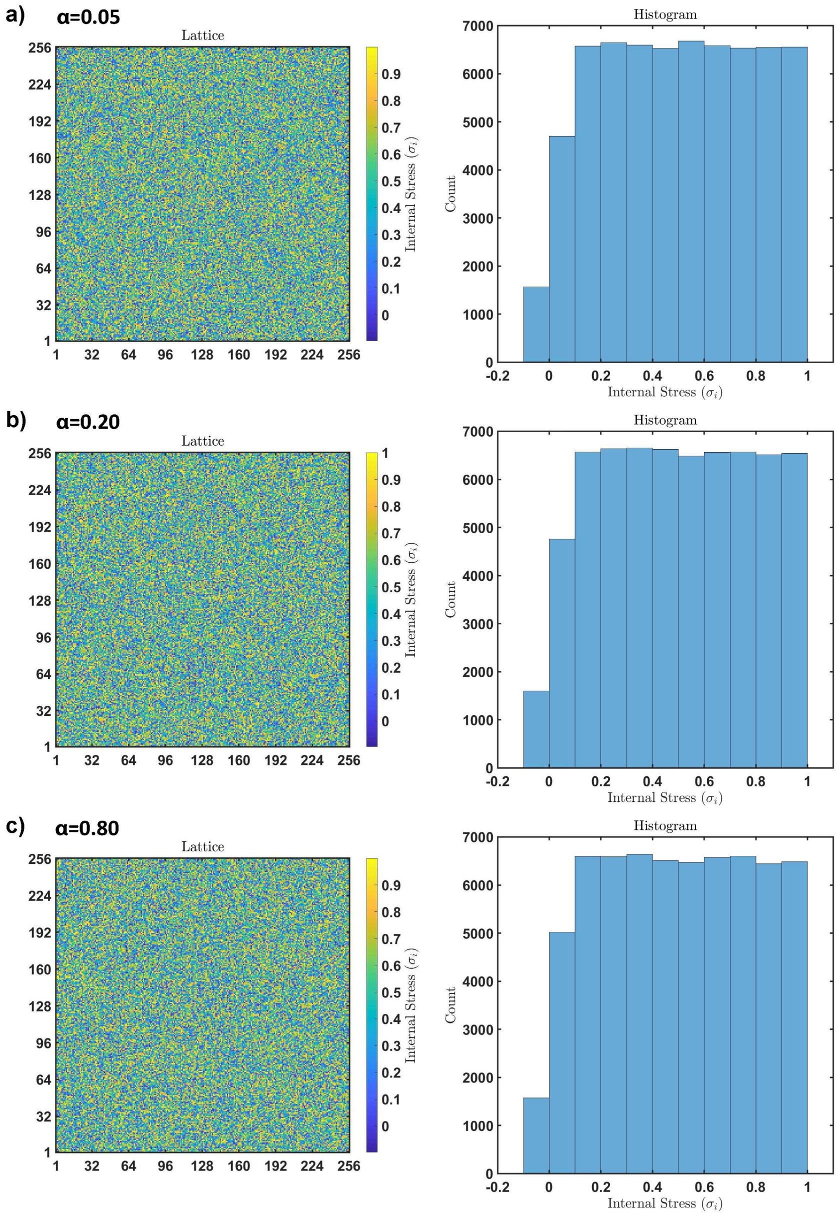

Figure 5.4: Internal stress snapshot shown on the left subplot with histogram of the lattice shown on the right subplot. From top to bottom, the plots are for models with dissipation parameters α of a) 0.05, b) 0.20, and c) 0.80. As the dissipation parameter increases the internal stress distribution remains uniformly distributed between $\sigma_R + \eta < \sigma_i < \sigma_F$ $(0.1 < \sigma_i < 1.0)$ and nearly identical across models.

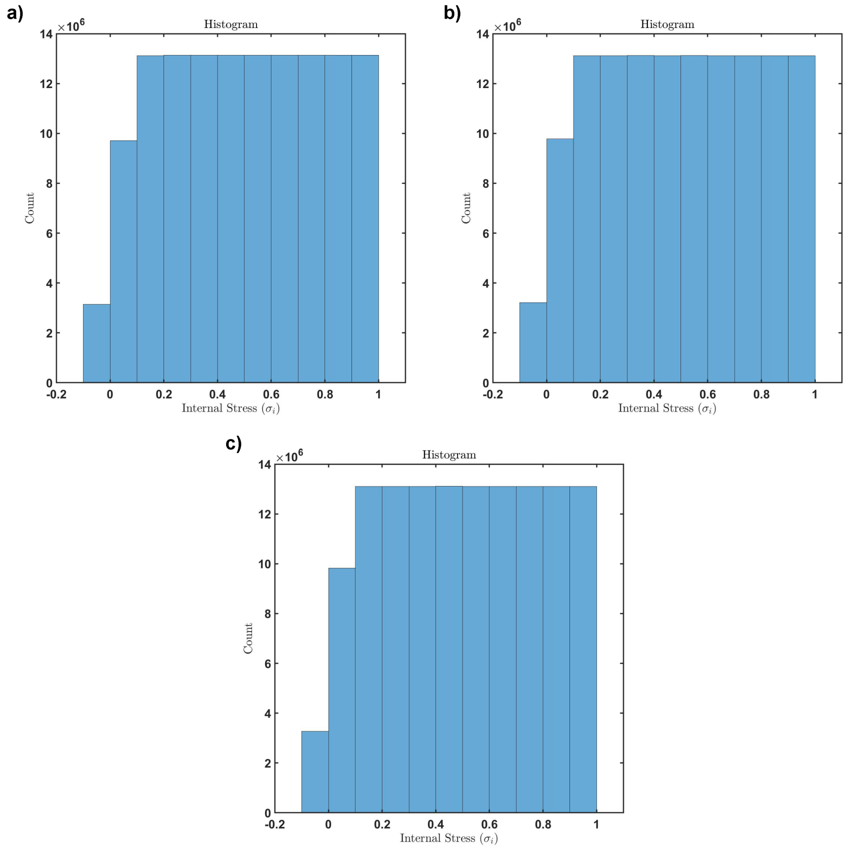

Figure 5.5: Cumulative internal stress histogram for all 2×10^3 snapshots for models with dissipation parameters of $\alpha =$ a) 0.05, b) 0.20, and c) 0.80. In all cases, the internal stress distribution approaches a uniform distribution between $\sigma_R + \eta < \sigma_i < \sigma_F$ ($0.1 < \sigma_i < 1.0$) with deviations between $\sigma_R - \eta < \sigma_i < \sigma_R + \eta$ ($-0.1 < \sigma_i < +0.1$).

approximately uniformly distributed for $\sigma_R + \eta < \sigma_i < \sigma_F$. The tail end at $\sigma_R - \eta < \sigma_i < \sigma_R + \eta$ is instead governed by the implementation of noise η within the CA model.

At the next plate update the minimum stress $min(\sigma_F - \sigma_i)$ is added to each cell of the system, thus shifting the internal stress distributions σ_i towards the failure threshold σ_F. Any internal stress greater than the failure threshold $\sigma_i > \sigma_F$ are reset to $\sigma_i = \sigma_R \pm \eta$. It follows that the main initiators and propagators of an avalanche of failures are the cells with internal stresses closest to the failure threshold σ_F.

5.2.2 Avalanche Sequences

At the beginning of a plate update, a single failure event is induced which may develop into an avalanche sequence of failed blocks otherwise known as the slip history. In seismology, asperities are areas of a fault held together by a localized region of high strength that are resistive to breaking (Lay et al., 1982). The observed variability in the slip distribution of an earthquake has been suggested as being governed by the varying degrees of asperities present within the slipping fault surface (Lay et al., 1982). These asperities with varied roughness govern the rupture process, ground motion and seismic release observed during a large slip event (Lay et al., 1982; Delouis et al., 2010; Candela et al., 2011).

Shown in Figure 5.6 is the size (cumulative failures) plotted against a given inner plate update time t_{in} for the three largest events for models with dissipation parameters of $\alpha = 0.05, 0.20, 0.80$ across all 2×10^3 snapshots. For a model with low dissipation $\alpha = 0.05$, Figure 5.6a, we observe that the slip history is highly variable with greater fluctuations in size. As the dissipation parameter increases, Figure 5.6b and c, the slip history decreases in size and duration. As expected, models with low dissipation parameters transfer greater amounts of stress to neighboring cells, thus creating more complex and lengthy ruptures. Examining the slip history for all homogeneous models, Figure 5.6, we notice that the peak, or main event, of a developing avalanche may occur at the beginning, middle or end of the slip history.

Within the CA model, the variability in the slip distribution and the propagation of a rupture is controlled by critically stressed regions (as defined by the areas with large concentrations of cells close to failure) that exist within the system and not the presence of asperities (as defined by stronger cells with higher failure thresholds). This suggests that variations in the slip history may not be enough to imply the presence of asperities (variations in failure strength). Lastly, (Rundle and Klein, 1995) observed similar results in their implementation of the homogeneous massless blocks connected to nearest neighbors blocks. The authors suggest that such a phenomenon is possible within a homogeneous model if several patches simultaneously fail analogous to a nucleation process (Monette and Klein, 1992).

Shown in Figure 5.7 are the spatial distributions of the three avalanche events (black cell), from left to right, for models with dissipation parameters of $\alpha =$ a) 0.05, b) 0.20, and c) 0.80, from top to bottom. Each avalanche is initiated at the failed cell marked by the red circle. The long range stress transfer for a failed cell is $R = 16$, where the released stress is uniformly redistributed among $N_{hex} = 816$ surrounding cells. Systems with low dissipation parameters transfer greater amounts of stress to neighboring cells, thus creating a larger cluster.

From Figure 5.7, the cluster may propagate away from the initially induced failure, shown as a red circle. Given that the models are homogeneous, and the internal stress distribution is approximately uniform across the lattice (Fig. 5.4), the clustering of failed cells should be evenly distributed. The fractal dimension D gives a quantitative measure of the spatial clustering of events, where $D = 2$ indicates complete randomness in cell failure distribution (see subchapter). Shown in Figure 5.8 are the correlation integral $C(r)$ versus distance r for all of the previous spatial distributions of the three avalanche events, from left to right, for models with dissipation parameters of $\alpha =$ a) 0.05, and b) 0.20, from top to bottom. The correlation integral $C(r)$ are computed using Equation 3.6. No correlation integral $C(r)$ are computed for models with high dissipation parameters ($\alpha > 0.40$) as their clusters have less than one hundred events (too few samples).

The fractal dimension D is fit using a linear regression model over the linear part of the curve for a radius interval of $1 \leq r \leq 20$ (small r) and is shown in the

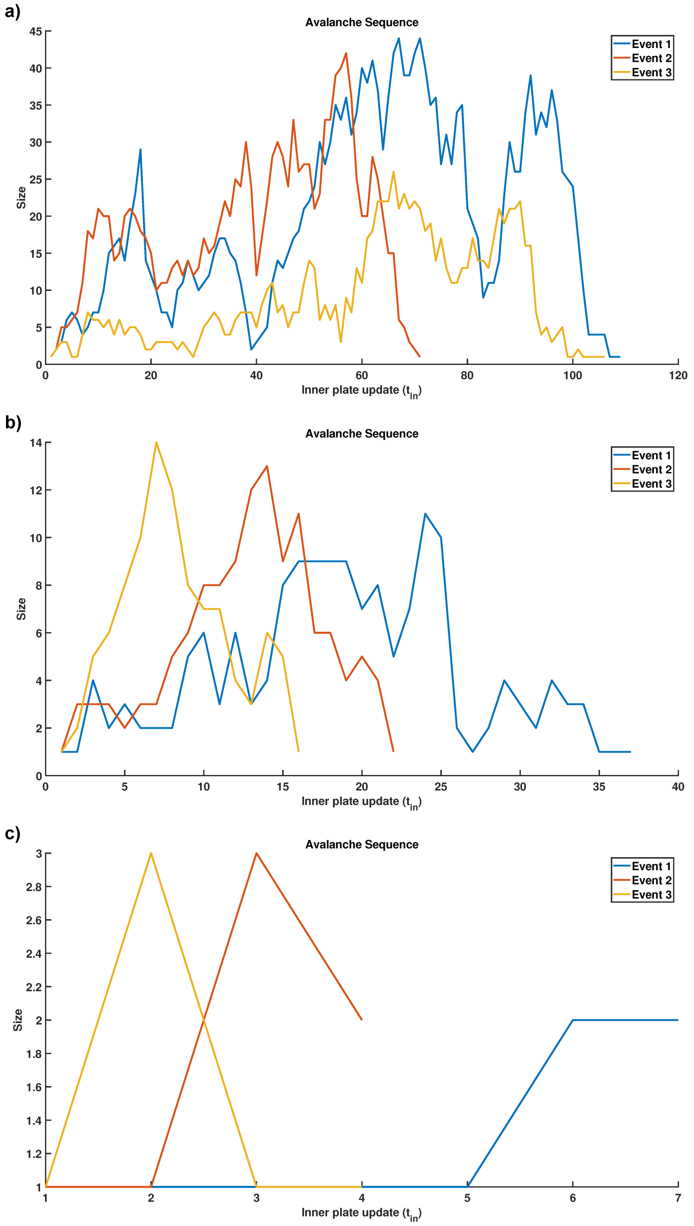

Figure 5.6: Size plotted against inner plate update time t_{in} of the three largest avalanche sequences from all 2×10^3 snapshots for models with dissipation parameters of $\alpha =$ a) 0.05, b) 0.20, and c) 0.80, from top to bottom, respectively. The slip, or individual events, are highly variable and may further propagate within critically stressed regions. Systems with low dissipation parameters transfer greater amounts of stress to neighboring cells, thus creating a more complex slip history.

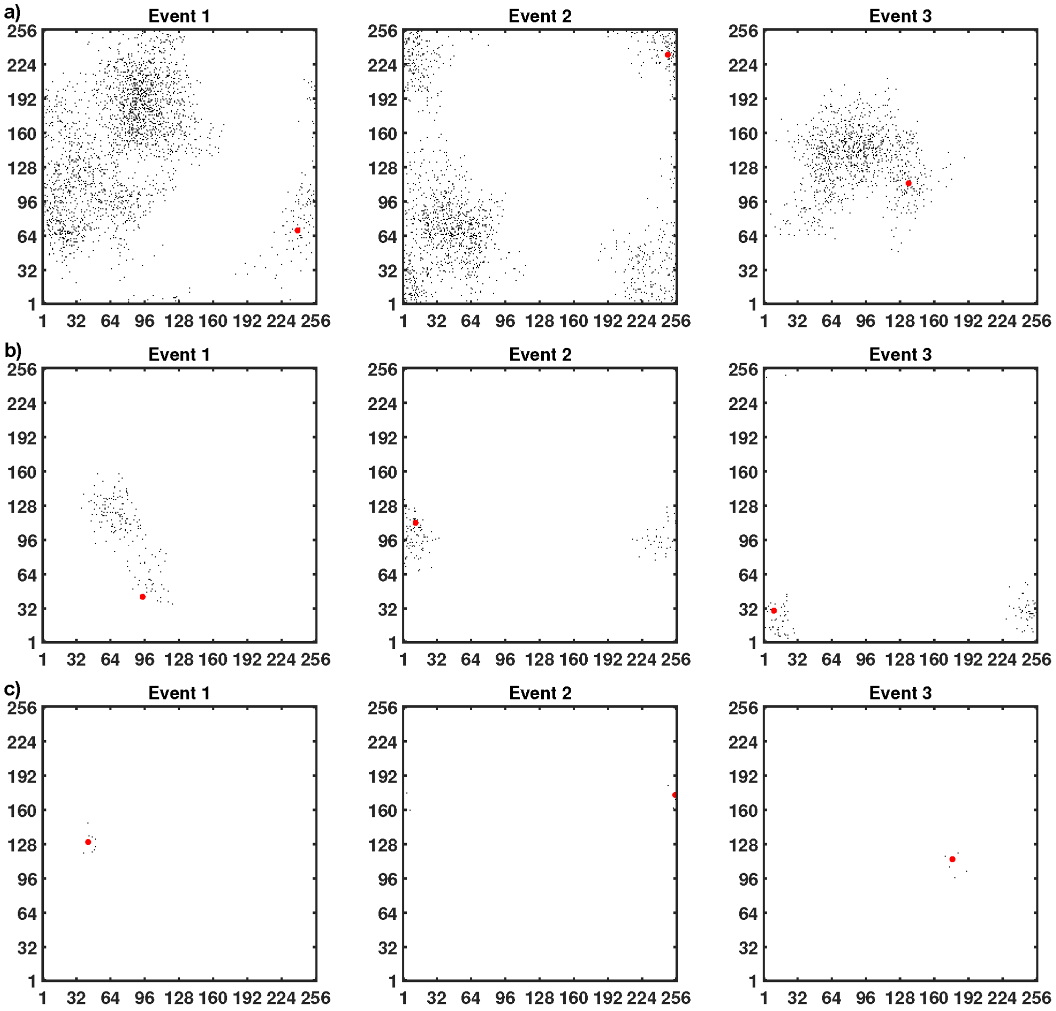

Figure 5.7: Spatial distribution of the three avalanche events, where a black cell represents a failure, for models with dissipation parameters of $\alpha =$ a) 0.05, b) 0.20, and c) 0.80. Each avalanche is initiated at the red circle, with a stress transfer radius of $R = 16$. Systems with low dissipation parameters transfer greater amounts of stress to neighboring cells, thus creating a larger cluster. The rupture initiation point is often not in the center of the total rupture area.

title bar, along with the standard error in the estimate. When estimating the fractal dimension D, if the data fall on a straight line then this is an indication that the spatial distributions of events have fractal structures (Hirata et al., 1987). Therefore, the fractal dimension D is estimated for clusters within radius intervals of $1 \leq r \leq 20$. The fractal dimension is found to be roughly equal to $D = 2$ for the dissipation models of $\alpha = 0.05, 0.20$, Figure 5.8a and b, where clusters have over $N > 100$ events. The fractal dimension of $D \approx 2$ suggests a random distribution in the location of the events for the homogeneous models. Likewise, fractal dimensions of $D = 1$ and $D = 0$ suggest a distribution of events along a lineation and a point, respectively. For greater radius the slope of the correlation integral $C(r)$ versus distance r decreases, suggesting a more linear spatial distribution of events. At large radii, $r > 10^2$, the spatial distribution of events becomes point like with a slope of $D = 0$. Lastly, determining the fractal dimension becomes unpractical for systems with high dissipation parameters ($\alpha > 0.40$) as the maximum number of events in a cluster decreases as shown in the non-cumulative frequency-size distributions, see Figure 5.2.

5.2.3 Model Expectancies

All of the CA models are simulated for a total of 10^6 plate updates for which we track the cumulative failures of each cell in intervals of 500 plate updates. Therefore, we can compare the total number of failures for an individual cell $n_{tot\,cell}$ at the end of all 10^6 plate updates from our CA model results and the simplified self-interacting conceptual model (Eq. 3.4); the results are summarized in Table 5.2. For the conceptual model, the dissipation parameter α, and the total physical time t_{phys} used in Equation 3.4 vary, while the failure threshold $\sigma_F = 1.0$ and residual threshold $\sigma_R = 0.0$ remain constant.

The mean and the standard deviation of the cumulative number of individual cell failures from the CA model match very closely the values of the simple self-interacting conceptual model. This suggests that the system at large behaves uniformly. There are no large deviations from the expected mean value of $n_{tot\,cell}$ calculated from the concept model (Eq. 3.4), therefore suggesting that there is no preferential flow of stress either into (higher failures) or out of

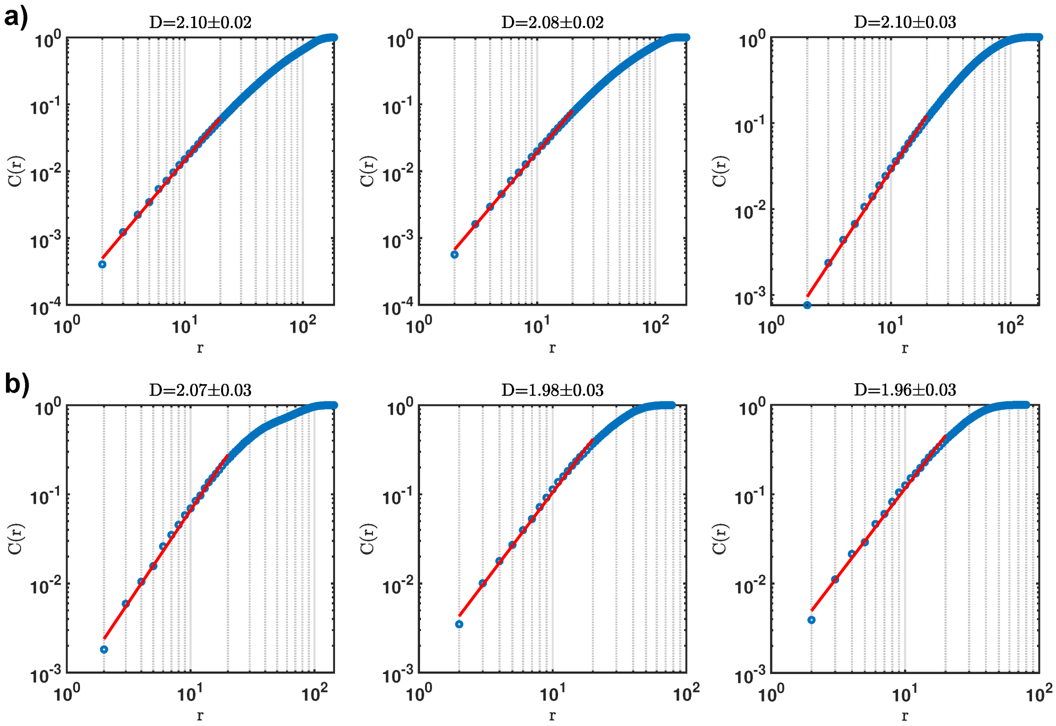

Figure 5.8: Correlation integral $C(r)$ versus distance r for each of the three largest avalanche sequences, left to right, from all 2×10^3 snapshots for models with dissipation parameters of $\alpha =$ a) 0.05, and b) 0.20, from top to bottom. The fractal dimension D, shown in figure title bar with standard error, is determined from the slope, shown as a red line, fitted over a linear part of the curve $1 \leq r \leq 20$.

Dissipation parameter α	Total physical time for 10^6 plate updates	Mean total failures from CA model	Total failures concept model
0.05	15.2101	303.33 ± 1.09	304.20
0.10	15.2338	152.02 ± 0.82	152.34
0.20	15.2560	76.17 ± 0.65	76.28
0.40	15.2551	38.10 ± 0.54	38.14
0.60	15.2653	25.43 ± 0.52	25.44
0.80	15.2600	19.06 ± 0.45	19.08
1.00	15.2585	15.25 ± 0.47	15.26

Table 5.2

Total stress added, proportional to physical time, to each homogeneous model over 10^6 plate updates. The table includes the mean and standard deviation of the cumulative number of individual cell failures from the CA model, and the cumulative number of individual cell failures calculated from the simplified self-interacting conceptual model (Eq. 3.4). The failure threshold $\sigma_F = 1.0$ and residual threshold $\sigma_R = 0.0$ remain constant between the varied models.

(lower failures) the cells within the system.

Chapter 6

Markov Chain Results

In this chapter, we predict the analytical frequency-size probability distribution from the transition matrices of the previously examined homogeneous CA models. Furthermore, using Markov chain Monte Carlo sampling (MCMC) we replicate the time series, frequency-size distribution, interevent time plot, and avalanche sequences of the homogeneous CA models.

6.1 Transition Matrices

Given the system parameters of $\sigma_F = 1.0$, $\sigma_R = 0.0$, $R = 16$ for $\alpha = 0.05, 0.20, 0.40, 0.60, 0.80$, and 1.00 we calculate the transition matrix $\mathbf{M}$ (Eq. 4.18) for every model. Within the CA model, σ_F and σ_R correspond to the failure and residual thresholds of a cell, respectively, with α being the dissipation parameter of the system. The stress transfer radius is set to $R = 16$, for a total of $N = 816$ neighboring cells within a hexagonal grid (Eq. 3.2), which results in a $(N + 1) \times (N + 1)$ transition matrix $\boldsymbol{M}$ for each system.

Shown in Figure 6.1 are the transition matrices for three of the models with varied dissipation parameters of $\alpha =$ a) 0.05, b) 0.20, and c) 0.80 with logarithmic transition probabilities (base 10) given the large range of values. Within the transition matrix $\boldsymbol{M}$, each i-th row represents an m-th current state $S_{i-1} = S_m$ with the j-th column representing the probability to move to the n-th state $S_{j-1} = S_n$, where the transition probabilities are given by the colorbar. For all transition matrices, state S_0 is the absorbing state with all other states $S_1, \ldots, S_{817}$ being transient states.

From the transition matrices (Fig. 6.1), as the dissipation parameter $\alpha \rightarrow 0$ the most likely transition probabilities approach the main diagonal, whereas as $\alpha \rightarrow 1$ the transition probabilities approach the first column. Therefore, as the dissipation parameter α increases, it becomes more probable to transition from a given state S_m to a lower state S_n. From the transition matrix, we construct an analytical frequency-size probability distribution by computing all possible paths, and their cumulative probabilities $P(S_{cum})$, up to a cumulative number of failures of $S_{cum} = 17$; these are later plotted along the frequency-size distributions sampled from the MCMC method.

6.2 Markov Chain Monte Carlo

We utilize the MCMC to repeatably sample absorbing Markov chains from the transition matrix $\boldsymbol{M}$ given the system parameters of $\sigma_F = 1.0$, $\sigma_R = 0.0$, $R = 16$, $L = 256$ for $\alpha = 0.05, 0.20, 0.40, 0.60, 0.80$, and 1.00. The total number of plate updates to be simulated is set to 10^6, identical to the CA models. For each plate update, the Markov chain begins at state S_1, or one induced failure, at the inner plate update of $t_{in} = 1$ and continues until the Markov chain has been absorbed into state S_0. For each plate update t_{pu}, we save the Markov chain at every inner plate update t_{in} (avalanche sequence), cumulative failures S_{cum} (size), and the units of stress added $\Delta\sigma$ to induce a failure (t_{phys}).

6.2.1 Time Series

A snippet of the MCMC (positive values) and CA (negative values) time series up to $t_{phys} = 1$ is shown in Figure 6.2 for different dissipation parameters α. From the time series, as the dissipation parameter increases from $\alpha = 0.05$ (Fig. 6.2 top subplot) to $\alpha = 1.00$ (Fig. 6.2 bottom subplot) the average size of an event decreases. For all cases, the time series is random and unpredictable with no signs of foreshock and aftershock sequences prior to a large sized event, identical to the CA model results.

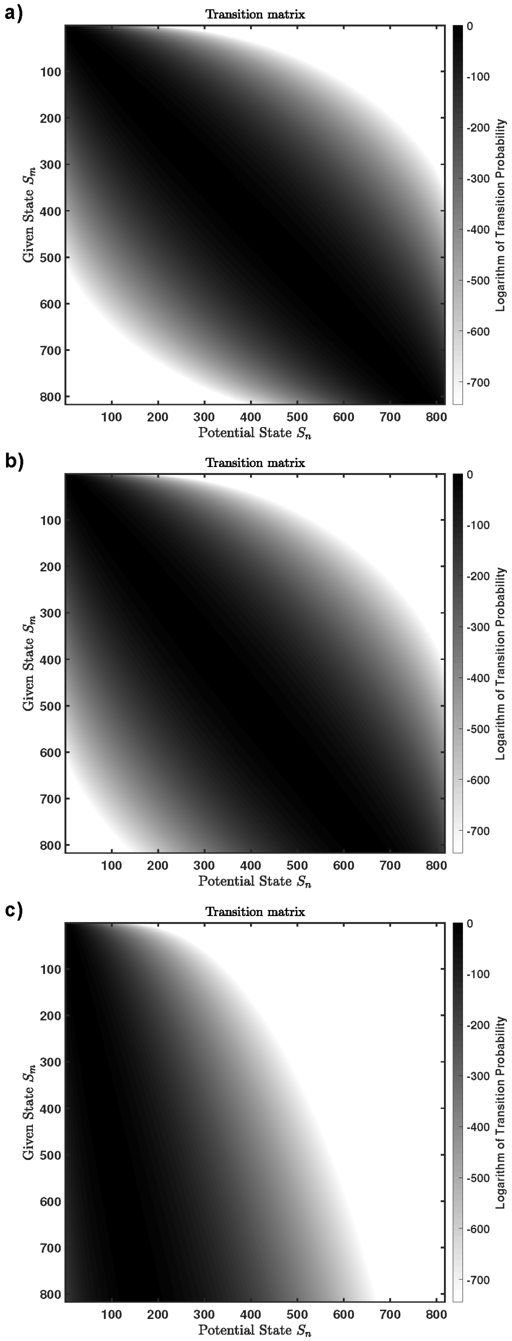

Figure 6.1: Calculated transition matrices $\mathbf{M}$ for three varied dissipation parameters of $\alpha =$ a) 0.05, b) 0.20, and c) 0.80 given identical system parameters of $\sigma_F = 1.0$, $\sigma_R = 0.0$, $R = 16$. Given a current state S_m the transition probability to a potential state S_n is shown by the colorbar in a logarithmic scale, base 10, given the large range of values. A system with a low dissipation parameter may reach higher states S_n, whereas a system with a high dissipation is bound to lower potential states S_n.

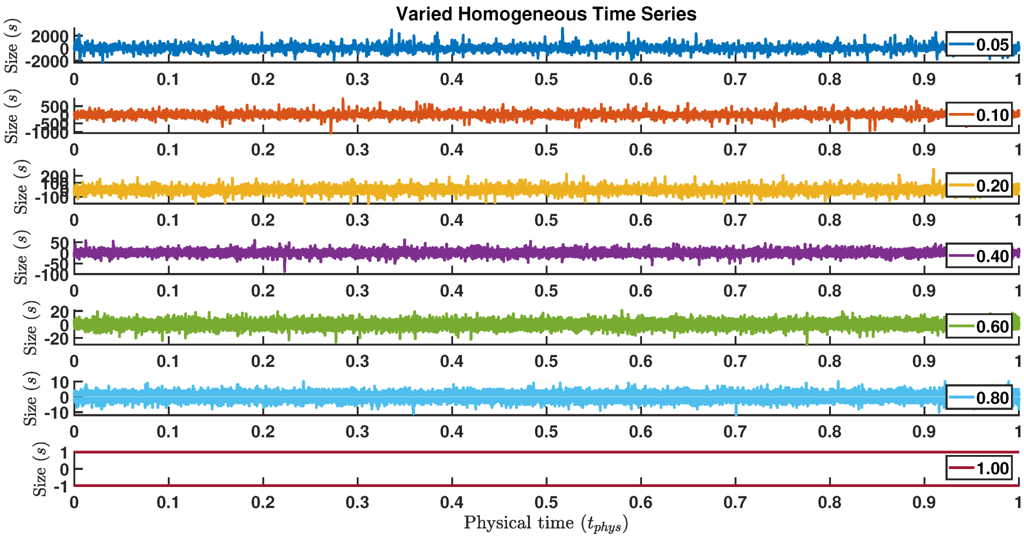

Figure 6.2: Physical time series of events (number of failed cells) for varied dissipation parameters over 1 units of physical time from the MCMC (positive values) and CA (negative values) models. As the dissipation parameter increases the size of events decreases. Both models are in good agreement.

A physical time cutoff of $t_{phys} = 15.2101$ was used for the non-cumulative frequency-size distributions, identical to the homogeneous CA models. Table 6.1 summarizes the total stress, or physical time, required for all MCMC models to complete 10^6 plate updates, along with the total plate updates completed given the physical time cutoff. From Table 6.1, the total physical time needed to complete an equivalent number of plate updates is independent of the dissipation parameter of the model. This is because for the MCMC model, the physical time steps are sampled from identical uniform internal stress distributions ($\sigma_R < \sigma_i < \sigma_F$) for a samples size of L^2, see Figure 4.4.

For the CA models, the total physical time t_{phys} needed to complete an equivalent number of plate updates t_{pu} decreases with decreasing dissipation parameter α as the system should be closer to failure. For the CA model, see Table 5.1, the total physical time to complete 10^6 plate updates can be seen to increases from $t_{phys} = 15.2101$ to 15.2585 for a system with a dissipation parameters of $\alpha = 0.05$ and 1.00, respectively. Comparatively, the total physical time needed to complete 10^6 plate updates for the MCMC model does not show a decrease in physical time. This would suggest that differences in the internal

Dissipation parameter α	Total physical time for 10^6 plate updates	Total plate updates for $t_{phys} = 15.2101$
0.05	15.2802	995,394
0.10	15.2594	996,822
0.20	15.2744	995,830
0.40	15.2817	995,402
0.60	15.2595	996,755
0.80	15.2650	996,326
1.00	15.2515	997,263

Table 6.1

Total stress added, proportional to physical time, to each MCMC model over 10^6 plate updates and the total number of plate updates completed given a physical time cutoff of $t_{phys} = 15.2101$. The physical time cutoff is identical to the homogeneous CA models.

stress distribution exist for CA models with different dissipation parameters.

6.2.2 Frequency-Size Distribution

The non-cumulative frequency-size distributions for both the MCMC (circles) and CA (crosses) models are shown in Figure 6.3, along with the theoretical OFC model with mean-field scaling of $n_s \sim s^{-3/2}$ plotted as a black line (Klein et al., 2000, 2007). The black diamonds are the analytically calculated frequency-size probability distributions multiplied by the total number of plate updates t_{pu} completed given a physical time cutoff of $t_{phys} = 15.2101$ for the MCMC models (Table 6.1). The physical time cutoff is identical for both MCMC and CA models.

The predicted frequency-size distributions, plotted as black diamonds, match the MCMC frequency-size distribution very accurately, particularly for well sampled non-cumulative event counts n_s. Visually, both the analytical (black diamond) and MCMC models (circles) are also in good agreement with the frequency-size distributions of the homogeneous CA models (crosses). As the dissipation parameter α increases, we observe an increase in both the slope and intercept in Figure 6.3; therefore, we observe a decrease in the maximum expected size (magnitude) with an increase in small size events. Likewise, a higher stress dissipation suppresses the occurrence of large sized events, while

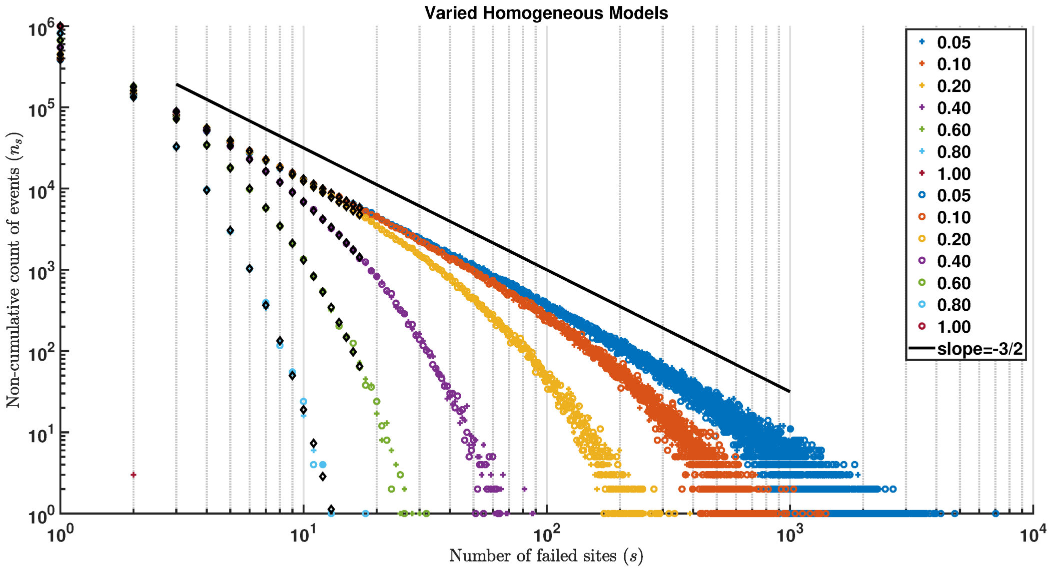

Figure 6.3: Non-cumulative frequency-size distributions for the MCMC (circles) and CA (crosses) models for varied dissipation parameters α. The black diamonds are the analytically calculated frequency-size distribution for the Markov process. Both MCMC and CA models are in good agreements and suggest that as the dissipation parameter increases both the intercept and slope increase. The black line has a slope of $-3/2$ predicted from the scaling of OFC models with low dissipation and long range interactions.

a low dissipation approaches the mean-field scaling, plotted as the black line, predicted for OFC models (Klein et al., 2007).

The CA model with a dissipation parameter of $\alpha = 1.00$ has three instances out of a million plate updates where two events where simultaneously induced at the beginning of a plate update. Although very rare, there is a chance that the internal stresses of two cells are equal or within machine precision of each other.

Shown in Figure 6.4 are the interevent plots of the mean physical time $\bar{t}_s$ between events of size s for all 10^6 plate updates; it can be thought of as the average time between events of size s. In Figure 6.4, the solid and dotted curves are the mean interevent physical time $\bar{t}_s$ for the MCMC and CA models, respectively, with the top and bottom dashed lines being the third ($Q3$) and first ($Q1$) quartiles for the MCMC models. Again, both MCMC and CA models are in good agreement with each other. At the tail end of the curves, the data are sparse and therefore the calculated mean interevent physical time $\bar{t}_s$ contains

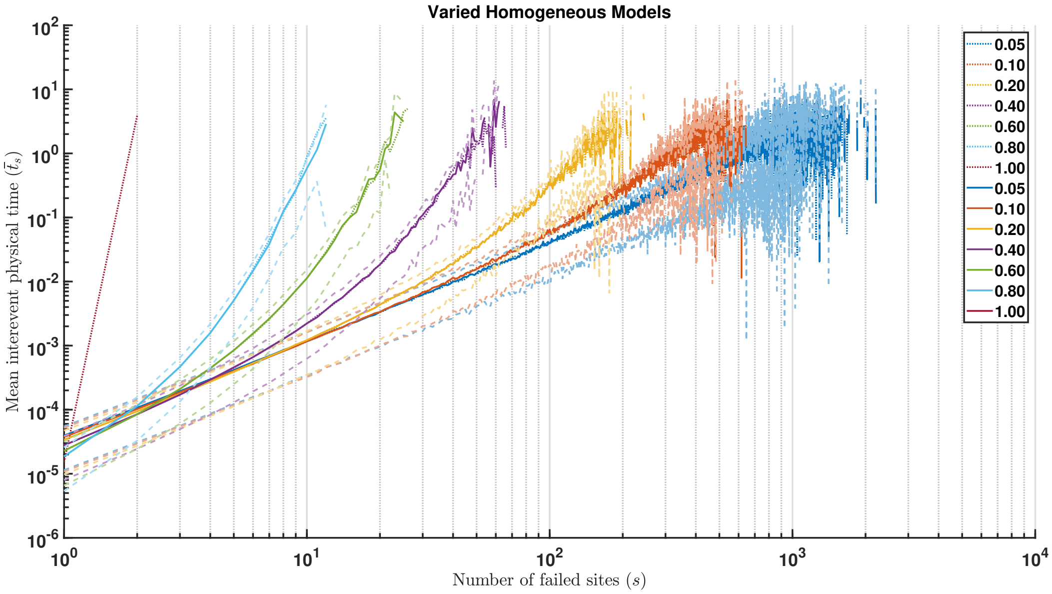

Figure 6.4: Mean interevent physical time $\bar{t}_s$ between events of size s for varied dissipation parameters from the MCMC (solid curve) and CA (dotted line) models. The top and bottom dashed lines are the third and first quartiles for the MCMC models. As the dissipation parameter increases the mean interevent physical time $\bar{t}_s$ for a given sized events s increases. The MCMC and CA models are nearly identical.

lots of variability and gaps in data.

From Figure 6.4, the mean interevent physical time (or period) increases as the event size s increases for all MCMC models (solid curve), which is in good agreements with the homogeneous CA models (dotted line). The interevent physical time $\bar{t}_s$ for the largest size events is found to be similar across all MCMC models, also a feature of the mean interevent plot of the CA models. Identical to the homogeneous CA models, a high dissipation system has an increased occurrence of small sized events with a reduced occurrence of larger sized events. The opposite occurs for a low dissipation system, where there is a reduced occurrence of small sized events with an increased occurrence of larger sized events. Therefore, the results of a homogeneous CA model can be replicated by modeling a stochastic process with a proper underlying stress distribution for the system.

6.2.3 Avalanche Sequences

At the beginning of a MCMC plate update, a single failure event is induced which may propagate into new failures depending on the underlying transition matrix of the system. An assumption for the MCMC model is that the internal stress distribution remains unchanged after a failure, whereas in the CA model there would be a slight decrease in the systems internal stress after any given failure. On the other hand, within the CA model an induced failure might occur near or at a critically stressed region aiding in the development of an avalanche sequence.

Shown in Figure 6.5 is the size (cumulative failures) plotted against a given inner plate update time t_{in} for three events for the MCMC models with dissipation parameters of $\alpha =$ a) 0.05, b) 0.20, and c) 0.80. The avalanche sequences for the MCMC models were chosen to be equal, or nearly equal, in total cumulative size as the avalanche sequences of the homogeneous CA models (Fig. 5.6). Due to the complex evolution of both models, the many ways an avalanche may develop and the limited number of observations it is unlikely that both MCMC and CA models will have identical avalanche sequences.

Nonetheless, for a model with low dissipation $\alpha = 0.05$, Figure 6.5 top, we observe that the slip history is highly variable, and shows fluctuations in size identical to those of the CA model (Fig. 5.6a). As the dissipation parameter increases, Figure 6.5 b and c, the slip history decreases in size and duration as well. System with low dissipation parameters have increased probabilities to induce a failure of equal or larger size, thus their avalanche sequences (Markov chains) tend to be longer and more complex.

Examining the transition matrices of 6.1 suggests that the avalanche sequences, or Markov chains, are more probable to develop along a preferred path. For large sequences it is more probable that an avalanche sequence steadily increases and decreases. As the dissipation parameter α decreases the avalanche sequences are more likely to stay at the same state or to transition to a greater state. Inversely, for high dissipation parameters the avalanche sequence is much more probable to transition to a lower state.

Within the MCMC model, the variability in the avalanche sequences is purely a stochastic process governed at large by the internal stress distribution

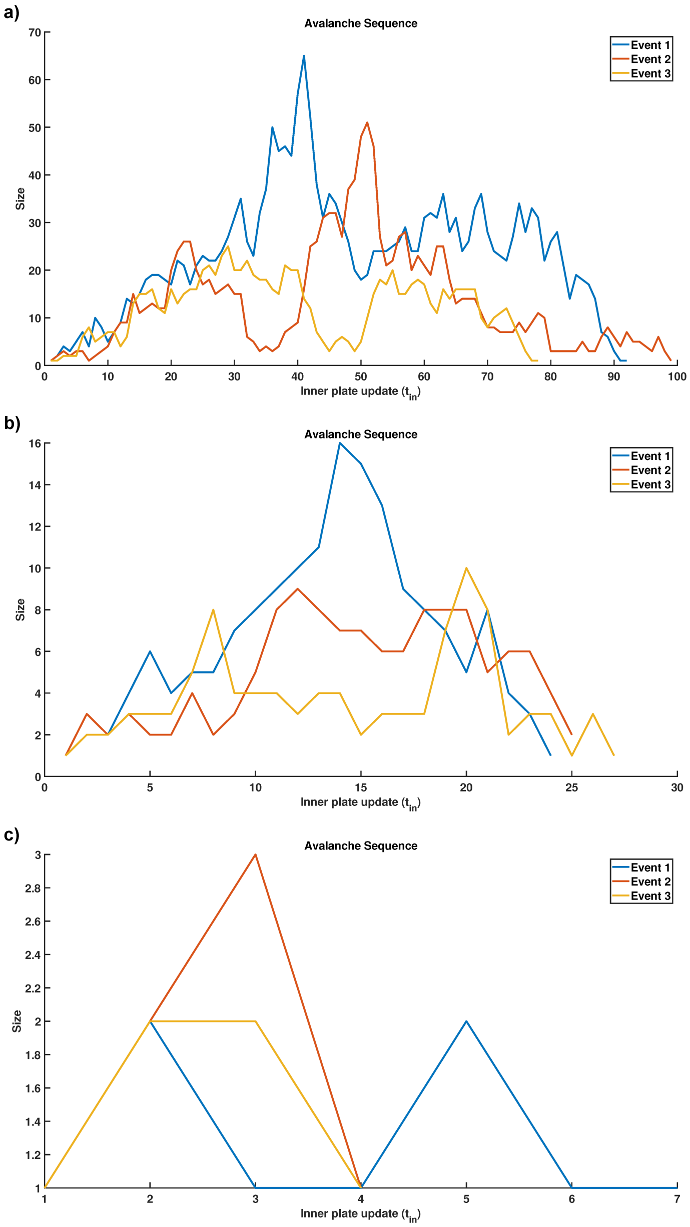

Figure 6.5: Size plotted against inner plate update time t_{in} of the three avalanche sequences for MCMC models with dissipation parameters of $\alpha =$ a) 0.05, b) 0.20, and c) 0.80. The slip, or individual events, are highly variable and depend on the path taken by the absorbed Markov chain. Systems with low dissipation parameters have transition matrices that increase the probability of transitions to greater states, thus creating more complex slip history.

of the system. In many ways, this simplified MCMC approach can recreate the results of the more complex CA model.

Chapter 7

Cellular Automaton Inhomogeneous Results

In seismology, areas of a fault held together by a localized region of high strength that are resistive to breaking are referred to as asperities (Lay et al., 1982). The effect of asperities has been described with two models. In the asperity model, the failure initiates at a strongly coupled region and propagates into the weaker zones, while in the barrier model the rupture initializes within the weaker zone and propagates into a strongly coupled region where the facture may continue or seize (Lay et al., 1982). Within our inhomogeneous CA model, we observe that asperities may behave as either one.

The most important factors of asperities are their distributions of strengths, the average ratio of asperity strength to the surrounding, and the spatial distribution of surrounding fault strengths (Kanamori, 1981). These factors would influence the foreshock sequences, quiescence period and precursory swarms, respectively.

In seismology, an asperity patch is thought to be the cause of spatial and temporal characteristics of earthquakes (Aki, 1984; Yamanaka and Kikuchi, 2004). In our model, inhomogeneities are incorporated as asperities with an increased failure threshold compared to a normal cell. Therefore, an asperity has a greater capacity to store and release stress back into the system once it fails. The addition of inhomogeneities into the CA model has been shown to add temporal and spatial clustering as observed in natural earthquakes (Kazemian et al., 2015).

In this chapter, we examine inhomogeneous CA models as large block asperities (first subchapter) and as varied structures (second subchapter). Why do asperities create temporal and spatial clustering within time series plots and how does it affect the scaling exponent (slope) and intercept (seismogenic index) of the frequency-size distribution? Along side, we include the predicted Markov chain (MC) frequency-size distribution for mixed systems.

Lastly, we investigate how the internal stress distribution, avalanche sequences, spatial clustering, and model expectancies are modified by the implementation of asperities.

7.1 Inhomogeneous Block Models

To examine the basic role of inhomogeneities in our model we varied the percentage of asperities within the model as a conglomerate block. The 2-D model has a lattice size of $L = 256$ cells, a long range stress redistribution of $R = 16$ with periodic boundary conditions. The dissipation parameter of $\alpha = 0.05$ was kept constant with the failure thresholds of the normal cells set to $\sigma_F = 1.0$, and $\sigma_{F_{asp}} = 11.0$ for the asperities. All cells have identical residual stresses of $\sigma_R = 0.0 \pm \eta$, where η is a random uniformly distributed noise between $\eta = [-0.1, +0.1]$. Therefore, the noise η remains fixed between all models, regardless of the failure threshold. We consider five different cases with 0%, 25%, 50%, 75%, and 100% percent of asperities present within the model, see Figure 7.1. Prior to simulation, the internal stresses of each cell are uniformly randomly distributed between $-\eta < \sigma_i < \sigma_F$, as previously done for the homogeneous CA models. The impact of noise is discussed in a later part of this chapter. In all cases, the system was simulated for 2×10^6 plate updates to remove any transient effects before recording the size, or number of failed cells, for the next 10^6 plate updates.

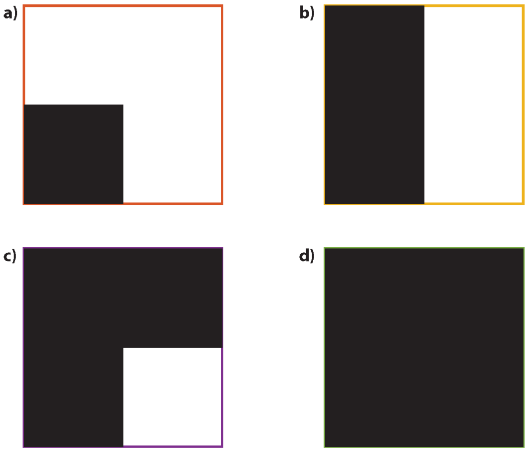

Figure 7.1: Various inhomogeneous block models with normal cells ($\sigma_F = 1.0$) in white and asperities ($\sigma_{F_{asp}} = 11.0$) in black. Models shown have asperity percentages ranging from a) 25%, b) 50%, c) 75%, and d) 100%. The total lattice size is 256 by 256 hexagonal elements.

7.1.1 Time Series

A snippet of the time series up to $t_{phys} = 11$ is shown in Figure 7.2 for block models containing different fractions of asperities, along with the benchmark model with no asperities ($asp = 0.00$). From the time series, the addition of asperities increases the maximum expected event size when compared to the no asperity model ($asp = 0.00$). Notably, the $asp = 0.75$ model produces nearly double the maximum size when compared to all other models. As the percentage of asperities increases, the time series develop temporal and periodic clustering or synchronized failures of cells. Visually, the periodicity of the time series clusters between the various block models is very similar. Therefore, the failure threshold of the asperities governs the quiescence period between the clusters. An increase in $\sigma_{F_{asp}}$ would result in an increase in quiescence period Δt_{phys} between major clusters because more stress, and thus physical time, is needed to bring stronger cells to failure.

When comparing the benchmark no asperity model ($asp = 0.00$) with the complete asperity model ($asp = 1.00$) there is a distinct difference in the time series clustering. Although both models are homogeneous with respect to their failure thresholds, the asperity model $asp = 1.00$ generates time series clusters, whereas the no asperity model $asp = 0.00$ does not. The cause of the difference

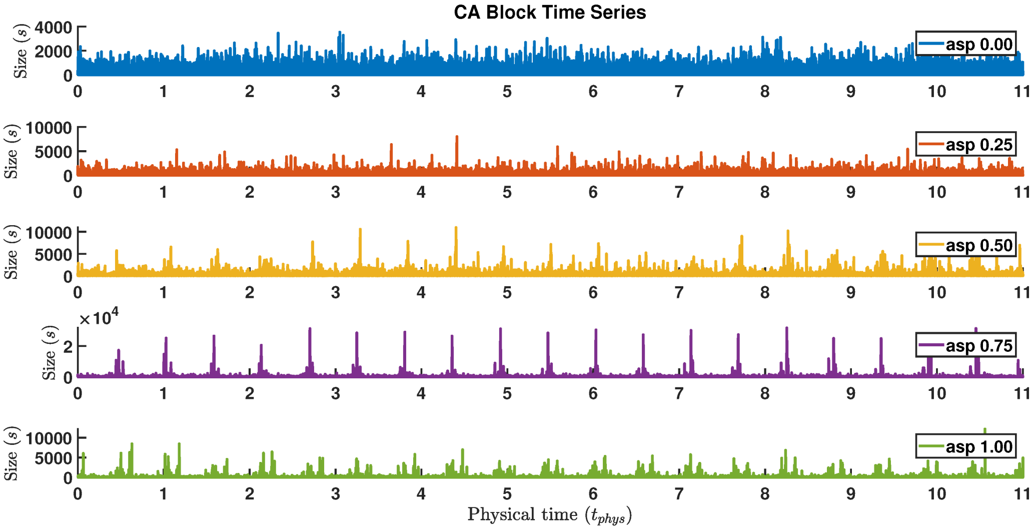

Figure 7.2: Physical time series of events (number of failed cells) for varied block models over 11 units of physical time. As the percentage of asperities increases a more complex temporal clustering appears with an increase in the maximum size compared to the benchmark no asperity model ($asp = 0.00$). The regular peaks are particularly visible for the $asp = 0.75$ model. Model structures are shown in Figure 7.11.

is discussed in this chapter and in a later chapter.

Given that the asperities failures are synchronized, it is possible to predict the average physical time period of the cluster ($\bar{t}_{cluster}$) from Equation 3.4 by setting $n_{tot\,cell} = 1$ and solving for $\bar{t}_{cluster}$. Therefore, we find that $\bar{t}_{cluster} = n_{tot\,cell}(\sigma_{F_{asp}} - \sigma_R)\alpha = 1(11-0)0.05 = 0.55$, which can be visually confirmed from the times series of the clusters in Figure 7.2.

An identical physical time cutoff ($t_{phys} = 15.2101$) for all models gives fair comparison between the various models and their seismogenic index (intercept) in the non-cumulative frequency-size distributions. Table 7.1 summarizes the total stress, or physical time, required for all block models to complete 10^6 plate updates along with the total plate updates completed given the physical time cutoff. From Table 7.1, as the percentage of asperities increases so should the total physical time needed to complete an equivalent number of plate updates. This is because the presence of asperities increases the average failure threshold, or hardness, of the system.

Interestingly, when comparing the two homogeneous models of only normal

Asperity block model	Total physical time for 10^6 plate updates	Total plate updates for $t_{phys} = 15.2101$
$asp = 0.00$	15.2101	1,000,000
$asp = 0.25$	19.7113	771,337
$asp = 0.50$	28.9180	527,117
$asp = 0.75$	54.0634	284,660
$asp = 1.00$	940.9927	20,010

Table 7.1
Total stress added, proportional to physical time, to each inhomogeneous block model over 10^6 plate updates and the total number of plate updates completed given a physical time cutoff of $t_{phys} = 15.2101$.

cells $asp = 0.00$ and only asperities $asp = 1.00$, the total physical time required to complete 10^6 plate updates greatly increases from $t_{phys} = 15.2101$ to 940.9927. Given that a homogeneous model with no asperities requires a runtime of $t_{phys} = 15.2101$ for a failure threshold of $\sigma_F = 1.0$, if the inhomogeneous model physical time scaled linearly we would expect that an increased failure threshold would require a runtime of approximately $t_{phys} = 15.2101 \times \sigma_{F_{asp}} = 15.2101 \times 11 = 167.3111$. Instead, the simulated $asp = 1.00$ model requires a total of $t_{phys} = 940.9927$ to complete all 10^6 plate updates. Briefly, this is due to the synchronized failures of asperities that significantly change the dynamics of the CA model, as later discussed in this chapter.

7.1.2 Frequency-Size Distribution

The non-cumulative frequency-size distributions for all of the inhomogeneous block models are shown in Figure 7.3 as circles, with a physical time cutoff of $t_{phys} = 15.2101$ used for all models. The predicted Markov chain (MC) frequency-size distributions for inhomogeneous models are plotted as black diamonds for their respective block models. Lastly, the black line is the theoretical scaling of a homogeneous OFC model.

For the CA block models, as the percentage of asperities increases the intercept decreases, while the slope remains constant. Therefore, there is a reduction in the occurrence of small to large sized events ($10^0 < s < 10^3$) with the presence of asperities. Yet, there is a significant increase in the range and the maximum expected size (magnitude) with the presence of asperities, particularly for the $asp = 0.75$ block model. Lastly, the homogeneous asperity model $asp = 1.00$ shows a slight dip in the slope with a suppression of events between the range of $1 < s < 5 \times 10^1$. This is also present in the interevent time plot, shown later, for which all 10^6 plate updates are used.

For the predicted MC block models, plotted as diamonds, the intercept is seen to decrease with increasing percentage of asperities. The predicted frequency-size distributions for mixed systems is calculated as the sum of individual homogeneous MC models (Eq. 4.32). As the percentage of asperities increases the predicted frequency-size distributions increasingly deviates from the CA frequency-size distributions. In particular, for $asp = 0.75$ and 1.00 models there is a decrease in small sized events compared to the Markov chain models. Whereas the CA model for $asp = 0.00$ is in good agreement with the predicted MC model, the $asp = 1.00$ CA model is not. This suggests that the implementation of asperities behaves significantly different to normal cells.

Shown in Figure 7.4 are the interevent times plots of the mean physical time $\bar{t}_s$ between events of size s for all 10^6 plate updates. In Figure 7.4, the solid color curve is the mean interevent physical time $\bar{t}_s$, with the top and bottom of the dashed lines showing the third ($Q3$) and first ($Q1$) quartiles, respectively, for that given curve. For sparse data, particularly the tail end of the curves, the calculated mean interevent physical time and quantiles have lots of variability and gaps in data.

Generally, the mean interevent physical time (or period) increases as the event size s increases for all block models. Towards the tail end of the plot large events are under sampled for all models resulting in a sporadic curve. As the percentage of asperities increases there is an increase in the interevent physical time (decreased occurrence) for events of identical size s. Identical to the non-cumulative frequency-size distribution, there is a change in the slope for the $asp = 1.00$ model between the range of $10^1 < s < 10^2$ with a decrease in the mean interevent physical time (increased occurrence) for large sized events. This change in slope is not present in any other block model, nor for the homogeneous $asp = 0.00$ model with a lesser failure threshold. We will return to this point when discussing the influence of noise variance.

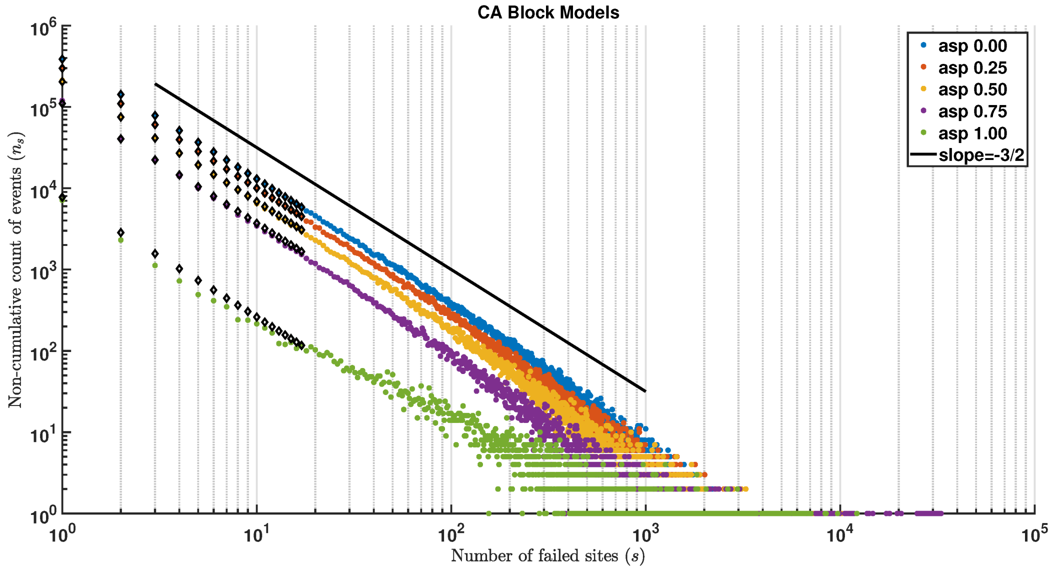

Figure 7.3: Non-cumulative frequency-size distribution as circles for CA block models along with the predicted Markov chain distributions as black diamonds. The CA distributions suggest that as the block percentage of asperities increases (top to bottom distributions) the intercept decreases, while the slope stays constant. The predicted Markov chain models also suggest that the intercept should decrease with increasing asperities, but to a greater extent than the CA models. For the CA models, asperities increase the maximum size from the baseline homogeneous $asp = 0.00$ model, particularly the $asp = 0.75$ block model having the greatest maximum magnitudes ($s_{max} \approx 3 \times 10^4$). The CA blocks models have a low dissipation parameter of $\alpha = 0.05$. The black line has a slope of $-3/2$ predicted from the scaling of OFC models with low dissipation and long range interactions.

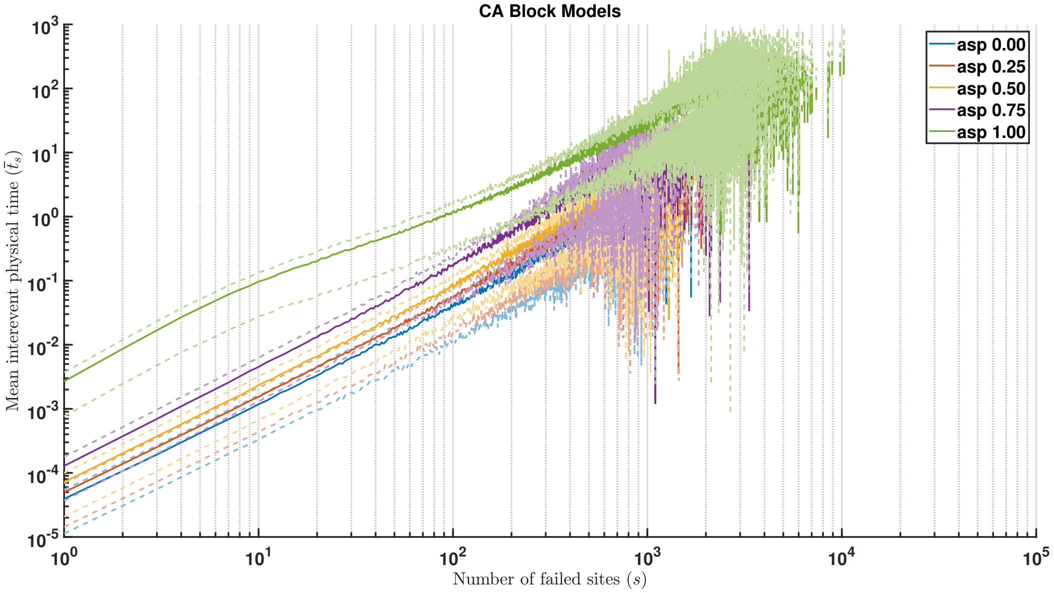

Figure 7.4: Mean interevent physical time $\bar{t}_s$ between events of size s for varied block models. Top and bottom dashed lines outline of the third and first quartiles, respectively, for a given curve. As the percentage of block asperities increases the mean interevent physical time $\bar{t}_s$ for a given sized events s increases. Uniquely, the asperity model $asp = 1.00$ has a change in the slope between the range of $10^1 < s < 10^2$ with a decrease in the mean interevent physical time for larger sized events.

7.2 System details

Additionally, at the end of every 500-th of the total 10^6 plate updates we output a snapshot of the internal stresses of all cells and the lattice's inner plate failure sequence t_{in}, and cumulative failures of each cell for a total of 2×10^3 snapshots.

7.2.1 Internal Stress Distribution

Shown in Figure 7.5 are the internal stress snapshots, and their respective histograms, for block models of $asp =$ a) 0.25, b) 0.50, c) 0.75, and d) 1.00, from top to bottom. The internal stress snapshot for the block model $asp = 0.00$ (no asperity) model is shown in a previous chapter, see Figure 5.4a. The internal stress distributions for all asperity block models show a triggering front of cells with high internal stress (about to fail) followed by cells with low internal stress (previously failed). These triggering fronts appear to travel away from the normal cells and inwards into the asperity blocks. Therefore, the normal cells may load the asperity blocks at the boundaries, thus creating a triggering front that travels inward into the asperities. The temporal clustering observed in the time series is the result of the trigger front advancing inwards within the asperity block.

For the homogeneous asperity model $asp = 1.00$, there are no normal cells, yet the internal stress distribution organizes itself much the same way. A triggering front sweeps periodically through the entire system, being the origin of the major time series clustering. This large triggering front appears to originate from the consistent bands of cells of alternating internal stresses found at the top the lattice, Figure 7.5d. These cells organize themselves as a subsystem failing at shorter timescales relative to the rest of the system, until triggering the larger wavefronts that make their way downwards across the rest of the system. As a side note, this banded subsystem has been validated to be present within the square lattice implementation, as well as the current hexagonal lattice, and is not an error in periodic boundaries.

As the percentage of asperities increases, the histogram of the internal stress distribution for asperities becomes less uniform and shifts towards a unimodal distribution with a peak at the center, as shown in Figure 7.6. The internal stress distribution of the normal cells remains uniformly distributed.

At the next plate update the minimum stress $min(\sigma_F - \sigma_i)$ is added to each cell of the system to induce a failure. At large, the normal cells subsystem behaves independent of the asperity blocks. If an asperity does fail at the boundary of the normal cells a large cluster of failures occurs within the normal cells due to the relatively large stress release. Yet, the time series clustering originates from the propagation of failures due to the asperity block. Given that the internal stresses within the asperities are synchronized in wavefronts, once a failure does occur it is likely that a chain reaction of events propagates along the critically stressed regions where the internal stresses are near the failure threshold σ_F.

7.2.2 Avalanche Sequences

At the beginning of a plate update, a single failure event is induced which may develop into an avalanche of failed cells otherwise known as the slip history. The presence of asperities has been shown to create temporal clustering within the time series (Fig. 7.2). Do avalanche sequences initiate at an asperity and propagate outwards towards weaker zones (asperity model), or does the rupture initiate at a weaker zone and propagate towards the asperities (barrier model)? Shown in Figure 7.7 are the three largest avalanche sequence from all 2×10^3 snapshots for block models $asp =$ a) 0.25, b) 0.50, c) 0.75, and d) 1.00. For the avalanche sequences, shown in Figure 7.7, the failure of an asperity at a given inner plate update t_{in} is marked with a colored black circle; this is omitted for the $asp = 1.00$ avalanche sequences for clarity. The avalanche sequence for the block model $asp = 0.00$, no asperities, is shown in Figure 5.6a.

From the block models $asp =$ a) 0.25, b) 0.50, c) 0.75, the slip history is variable with the largest event not necessarily corresponding to the failure of an asperity. Instead, the failure of asperities, black circles, are spread throughout the rupture sequences. Likewise, the initial failure at $t_{in} = 1$ may be initiated at an asperity and propagate outwards, or it may initiate at a normal cell and make its way towards the asperities. This is better shown in the spatial distributions of the three avalanche events, from left to right, for the block models a) 0.25,

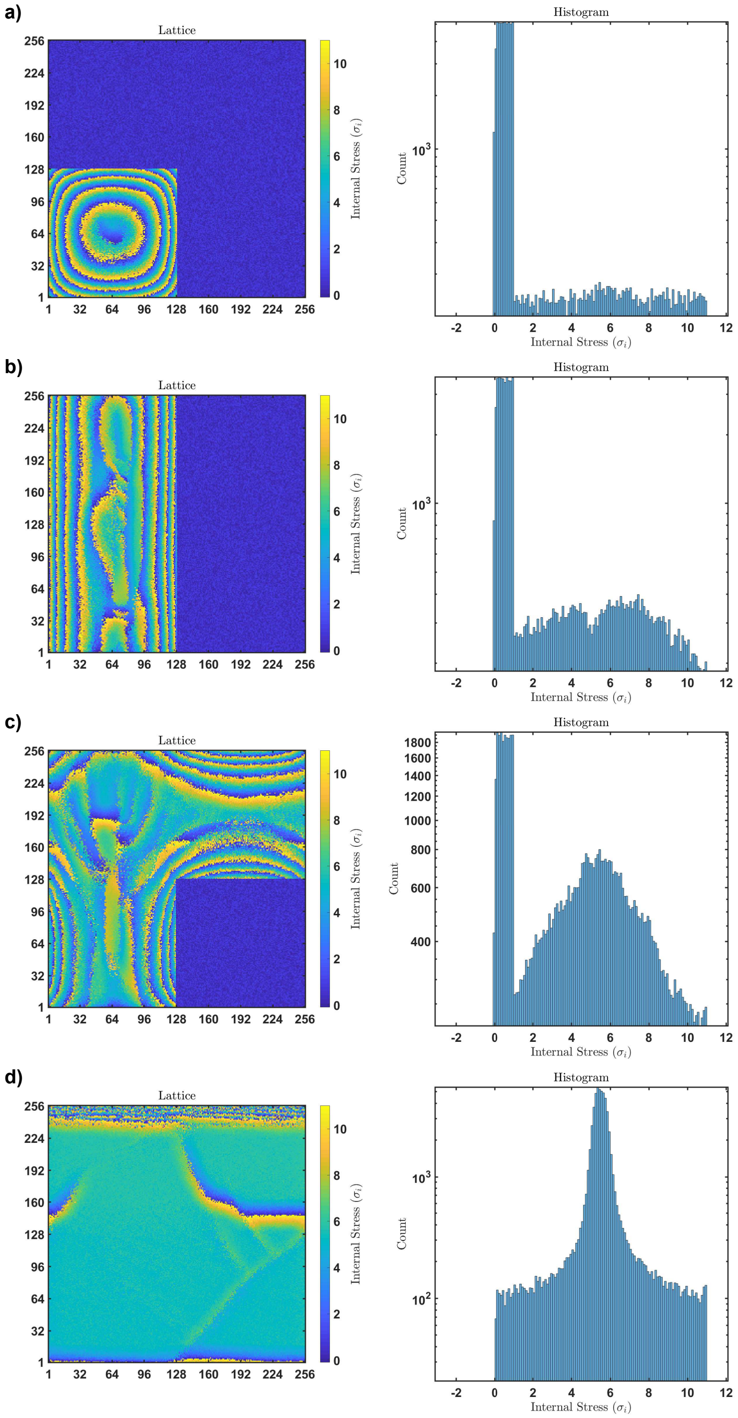

Figure 7.5: Internal stress snapshot shown on the left subplot with histogram of the lattice shown on the right subplot. From top to bottom, the plots are for models with asperity blocks of $asp =$ a) 0.25, b) 0.50, c) 0.75, and d) 1.00. For the internal stress snapshot of the $asp = 0.00$ model, see Figure 5.4a. The internal stress distributions for all asperity block models show structure in the form of a failure wavefront. From the histograms (logarithmic scale), as the percentage of block asperities increases the internal stress distribution of the asperities becomes unimodal.

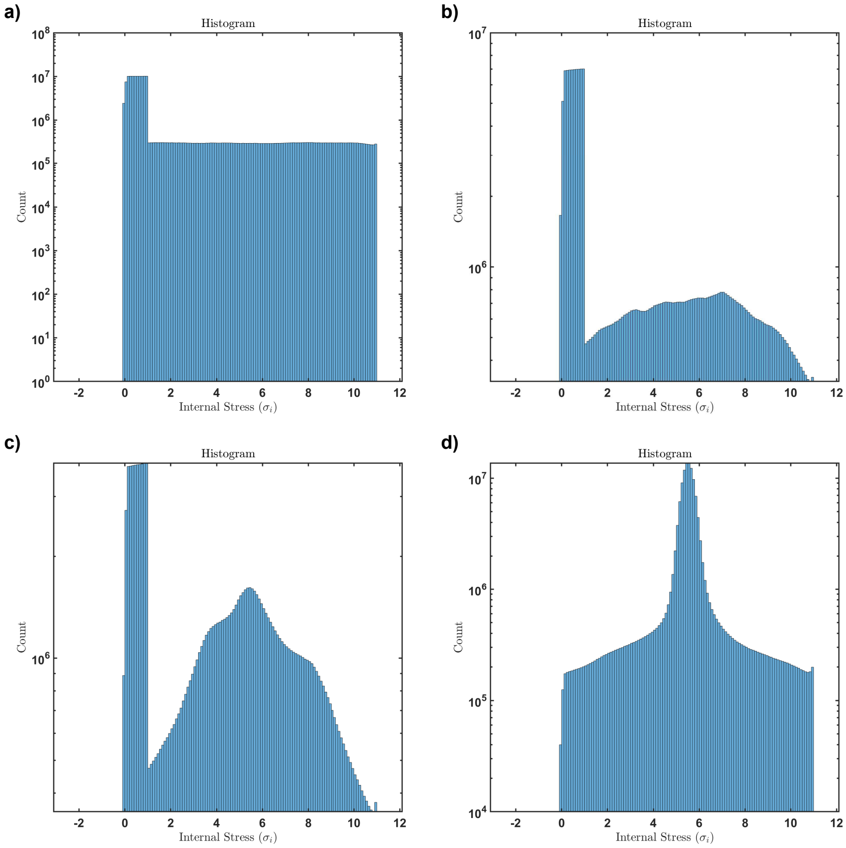

Figure 7.6: Cumulative internal stress histogram (logarithmic scale) for all 2×10^3 snapshots for block models $asp =$ a) 0.25, b) 0.50, c) 0.75, and d) 1.00. For the cumulative internal stress histogram of the $asp = 0.00$ model, see Figure 5.5a. In all cases, as the percentage of asperities increases the internal stress distribution approaches a unimodal distribution with a center peak, whereas the normal cells remain uniformly distributed.

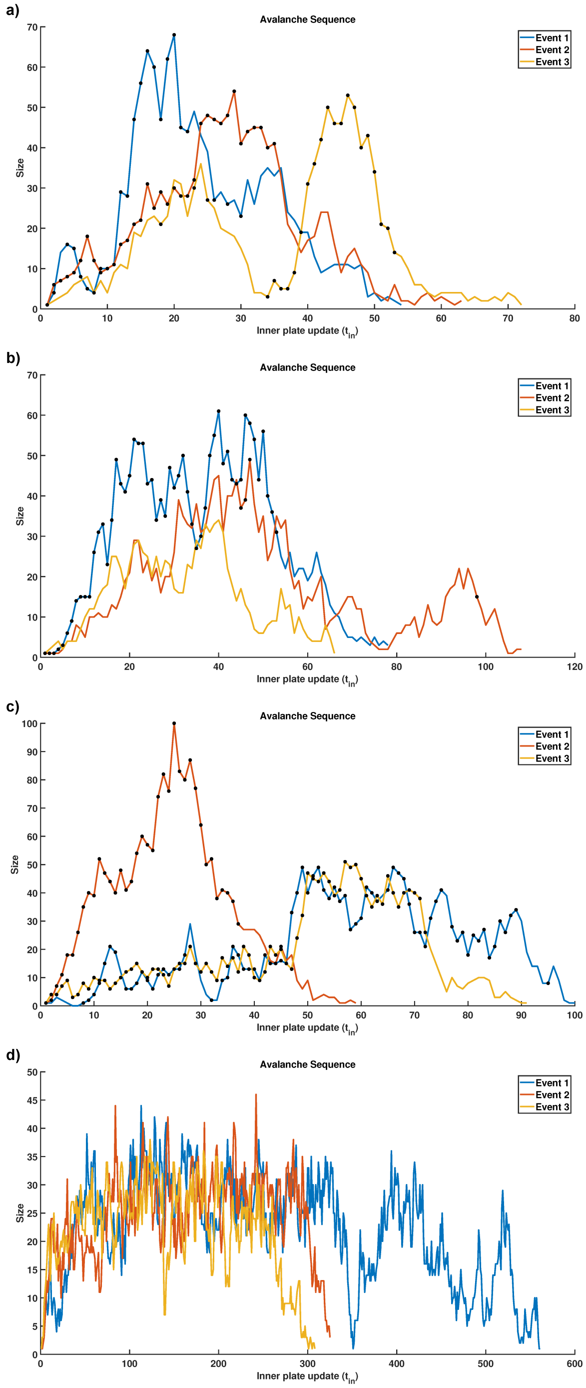

Figure 7.7: Size plotted against inner plate update time t_{in} of the three largest avalanche sequences from all 2×10^3 snapshots for block models $asp =$ a) 0.25, b) 0.50, c) 0.75, and d) 1.00. The avalanche sequence for the block model $asp = 0.00$, no asperities, is shown in Figure 5.6a. The failure of an asperity at a given inner plate update t_{in} is marked with a black circle; this is omitted for the $asp = 1.00$ avalanche sequences for clarity. The slip sequences are highly variable with the failure of asperities, black circles, spread throughout the avalanche. The largest event in the slip sequences does not necessarily indicate the failure of an asperity.

b) 0.50, c) 0.75, and d) 1.00, from top to bottom. Each avalanche is initiated at the failed cell marked by the red circle, where the failures of normal cells are plotted in black and the failures of asperities are plotted in blue.

As seen from the spatial clusters of the block models, Figure 7.8, failure may begin at an asperity and propagate along other asperities and possibly propagate to the surrounding normal cells (asperity model). Likewise, there may be instances where the failure initiates at the normal cells and propagates to the boundaries of the asperities, that may or may not fail (barrier model). Spatially, failures of asperities are distributed along critically stressed wavefronts, whereas the failures of the normal cells tend to be clustered around a previously failed asperity or evenly spread out. From the avalanche sequence, once an asperity does fail it is more likely that other asperities failures will subsequently fail given their close proximity. Equally, if the avalanche sequence does reach the normal cells the last avalanche sequence will most likely end within the normal cells rather than the asperity cells.

The failure behavior for the homogeneous asperity model $asp = 1.00$ is completely different to the other block models. In the $asp = 1.00$ model, the failure sequence propagates as a wavefront across the lattice. A large sized events would mean that the failure wavefront has propagated further across the lattice compared to a smaller sequence, as shown in Figure 7.8d. Therefore, the slip sequences of Figure 7.7d are very similar in shape with the main difference being the slip duration, which is proportional to avalanche size.

The fractal dimension D was fit for radius intervals of $1 \leq r \leq 20$ (small r), along with the standard error in the estimate, shown in Figure 7.9. For small radii, the fractal dimension of $D \approx 2$ suggests a random distribution in the location of the events. For greater radii the slope of the correlation integral $C(r)$ versus distance r decreases, suggesting a transition towards a more linear spatial distribution of events. At large radii, $r > 10^2$, the spatial distribution of events becomes point like with a slope of $D = 0$.

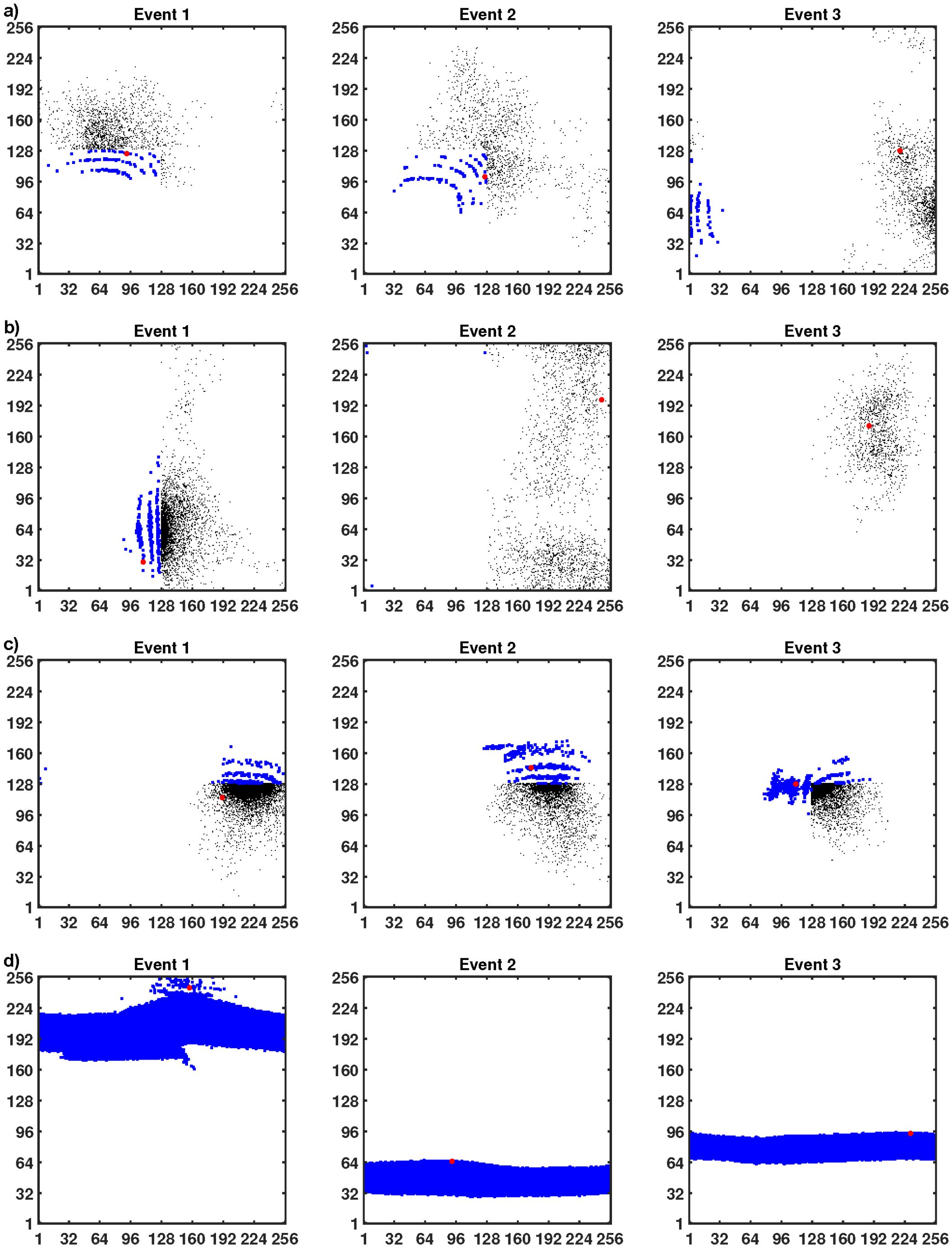

Figure 7.8: Spatial distributions of the three avalanche events, from left to right, for the block models asp = a) 0.25, b) 0.50, c) 0.75, and d) 1.00, from top to bottom. Each avalanche is initiated at the failed cell marked by the red circle, where the failures of normal cells are plotted in black and the failures of asperities are plotted in blue.

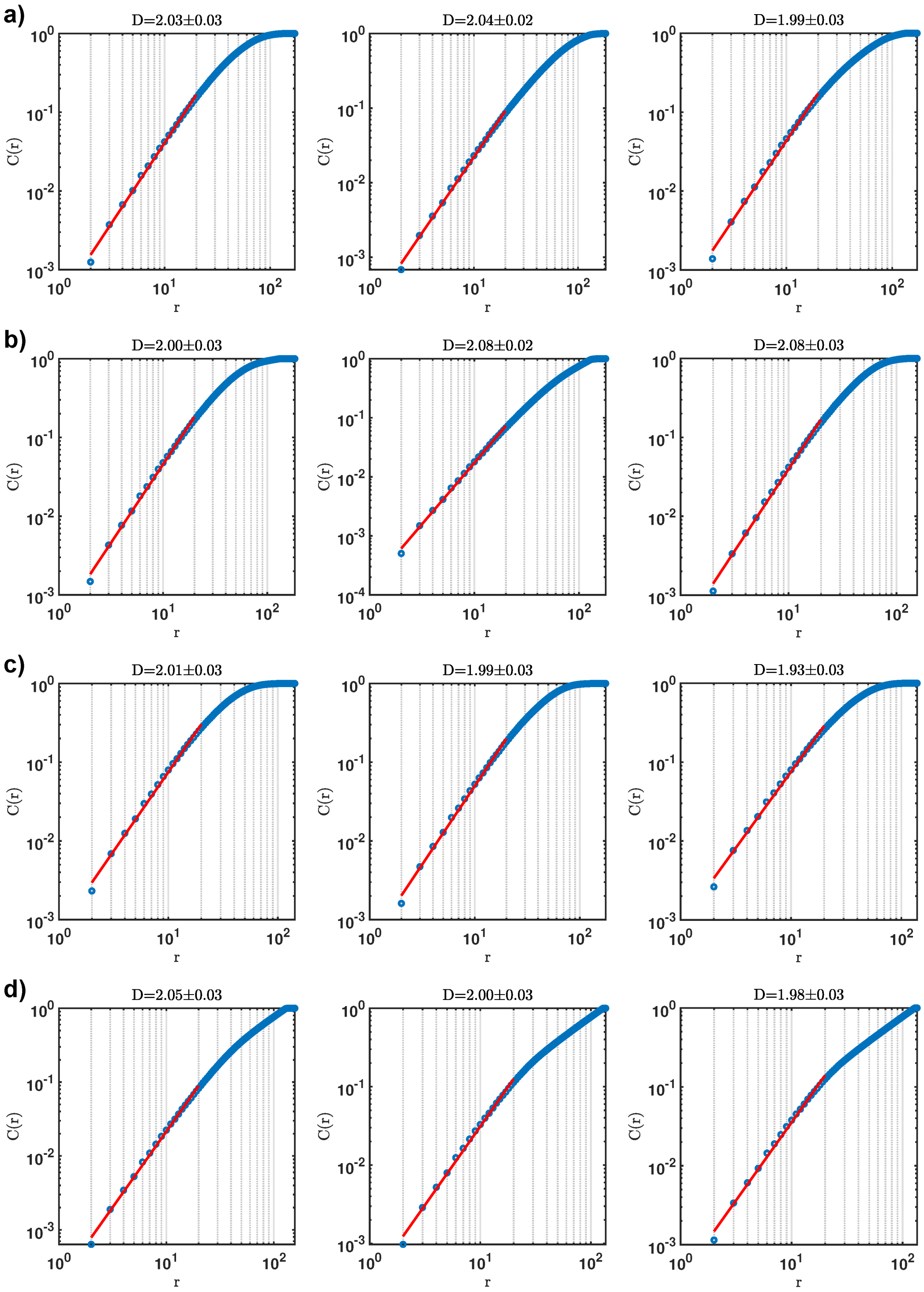

Figure 7.9: Correlation integral $C(r)$ versus distance r for each of the three largest avalanche sequences, left to right, from all 2×10^3 snapshots for block models $asp =$ a) 0.25, b) 0.50, c) 0.75, and d) 1.00. The fractal dimension D, shown in figure title bar with uncertainty, is determined from the slope, shown as a red line, fitted over a linear part of the curve $1 \leq r \leq 20$.

Asperity model	Total physical time for 10^6 plate updates	Mean total failures from CA model	Total failures concept model
asp=0.00	15.2101	303.33 ± 1.09 (nrm)	304.20 (nrm)
asp=0.25	19.7113	392.65 ± 1.65 (nrm) 35.70 ± 0.46 (asp)	394.23 (nrm) 35.84 (asp)
asp=0.50	28.9180	572.51 ± 10.50 (nrm) 52.34 ± 0.47 (asp)	578.36 (nrm) 52.58 (asp)
asp=0.75	54.0634	988.55 ± 130.26 (nrm) 97.59 ± 0.55 (asp)	1081.27 (nrm) 98.30 (asp)
asp=1.00	940.9927	1704.45 ± 0.75 (asp)	1710.90 (asp)

Table 7.2
Total stress added, proportional to physical time, to each block model over 10^6 plate updates. The table includes the mean and standard deviation of the cumulative number of individual cell failures for normal cells (nrm) and asperity cells (asp) from the CA model, and the cumulative number of individual cell failures calculated from the simplified self-interacting conceptual model (Eq. 3.4). The dissipation parameter $\alpha = 0.05$ and residual threshold $\sigma_R = 0.0$ remain constant between the block models.

7.2.3 Model Expectancies

All of the CA models are simulated for a total of 10^6 plate updates for which we track the cumulative failures of each cell in intervals of 500 plate updates. Therefore, we can compare the total number of failures for an individual cell $n_{tot\,cell}$ at the end of all 10^6 plate updates from our CA model results and the simplified self-interacting conceptual model (Eq. 3.4); the results are summarized in Table 7.2. The failure thresholds of the asperity cell $\sigma_{F_{asp}} = 11.0$ and normal cell $\sigma_F = 1.0$ vary depending on the cell, along with the total physical time t_{phys} taken to complete all 10^6 plate updates, while the dissipation parameter $\alpha = 0.05$ and residual threshold $\sigma_R = 0.0$ remain constant. Likewise, the cumulative number of individual cell failures over 10^6 plate updates for all of the inhomogeneous block models are shown in Figure 7.10.

Overall, when considering the standard deviation, the mean cumulative number of individual cell failures from the CA model for both the normal cells and asperity cells are approximately within the predicted values of the conceptual model. At large, this suggests that the normal and asperity block behave uniformly. Yet, as the percentage of asperities increases within the block model,

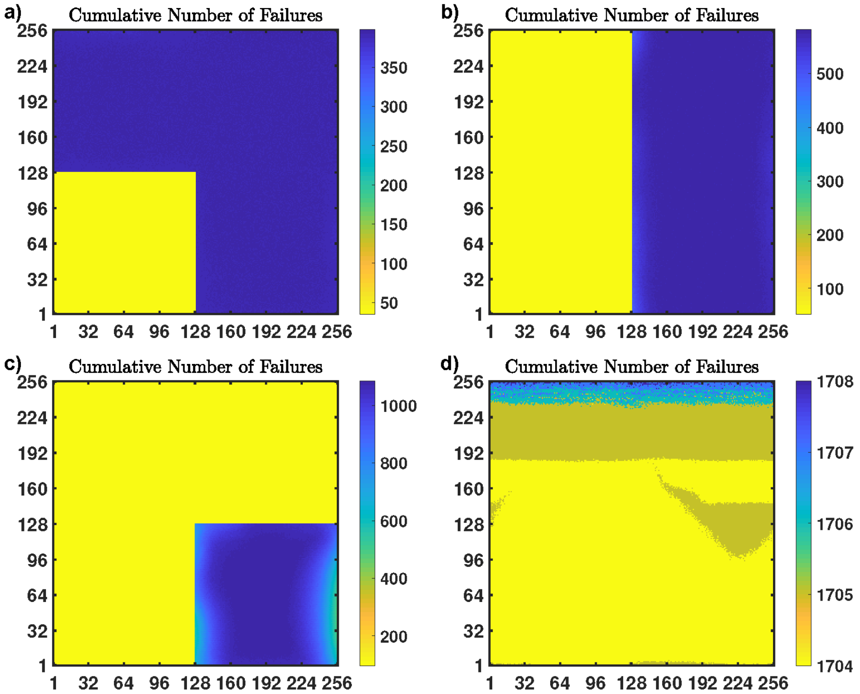

Figure 7.10: Cumulative number of failures for each cell over 10^6 plate updates for block models $asp =$ a) 0.25, b) 0.50, c) 0.75, and d) 1.00. Low cumulative number of failures appear to be at the boundaries of the asperity block.

there is a decrease in the mean failure of the normal cells compared to the predicted concept model. A decrease in the mean total number of failures for a normal cell would suggest a deficiency of stress flow into the normal cells, which would result in lower failures. As shown in Figure 7.10a-c, the cumulative number of failures for the normal cells are decreased at the borders of the asperities, but not uniformly along the boundary. From the block models asp =0.25, 0.50, and 0.75 the cumulative number of failures for the normal cells found at the boundaries of the asperities can be as low as $n_{tot_{cell}} = 378, 484,$ and 464, respectively. Given that the asperities fail less often than the normal cells, it is expected that the normal cells at the borders of the asperities have a reduced total number of failures. Yet, Figure 7.10 shows that this failure deficit is not evenly spread at every border, or even in every block model. Furthermore, we note that the cumulative number of failures for the asperities near the border do not fail more frequently than those further within the asperity block.

Lastly, the cumulative number of failures for the homogeneous asperity model $asp = 1.00$, Figure 7.10d, are not evenly distributed. The band of cells at the top of the lattice, from which the failure wavefront originates, have a slightly increased cumulative number of failures compared to the rest of the cells. Therefore, these top cells establish a static subsystem that fails at a periodicity that is irregular to the sweeping failure wavefront that makes its way across the lattice.

A question that arises is why is this band found at the top edge of the model, and not randomly distributed elsewhere such as in the middle of the lattice? Possibly this is an inherent feature due to the order in which cells are failed, where within the code the internal stresses of cells are read and failed in horizontal scan lines from the top to bottom. Therefore, when the entire lattice is near failure the sequence in which cells are read and failed may act as a seed in creating this top horizontal band of cells with slightly increased cumulative failures. This has not been validated within our model.

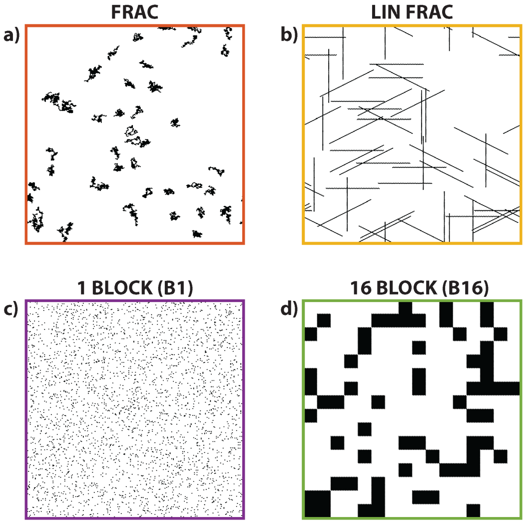

Figure 7.11: Various inhomogeneous structure models with normal cells ($\sigma_F = 1.0$) in white and asperities ($\sigma_{F_{asp}} = 11.0$) in black. Models shown have varied structures with asperity percentages ranging of a-c) 5%, and d) 25%. The total lattice size is 256 by 256 hexagonal elements.

7.3 Inhomogeneous Structure Models

To examine the effect of structure in our model we varied the spatial distribution of asperities within the lattice system. Identical to the previous inhomogeneous block models, all other model parameters were kept identical, such as $\alpha = 0.05$, $\sigma_F = 1.0$, $\sigma_{F_{asp}} = 11.0$, $\sigma_R = 0.0 \pm 0.1$, and $L = 256$. We consider four different cases that vary in structure with three models having 5% percent of asperities (frac, lin frac, rnd B1) and one model containing 25% of asperities (rnd B16), see Figure 7.11. Structures include a) random walk (frac), b) linear fractures (lin frac), c) random blocks of width 1 (rnd B1), and d) random blocks of width 16 (rnd B16). The benchmark homogeneous model contains no asperities. Identical to the previous section, the internal stresses of each cell are uniformly randomly distributed between $-\eta < \sigma_i < \sigma_F$. In all cases, the system was simulated for 2×10^6 plate updates to remove any transient effects before recording the size, or number of failed cells, for the next 10^6 plate updates.

7.3.1 Time Series

A snippet of the time series up to $t_{phys} = 11$ is shown in Figure 7.12 for structure models, along with the benchmark model with no asperities. From the time series, the structure of the asperities changes the shape of the clustering and the maximum event size, while the quiescence period between the clusters remains identical. In detail, the frac model (Fig. 7.12b) shows a clear foreshock, mainshock and aftershock sequence with very similar foreshocks and aftershocks in duration and size. The lin frac model (Fig. 7.12c) also shows a foreshock, mainshock and aftershock sequence, yet the foreshock sequences have a slight decrease in seismicity prior to the mainshock. The rnd B1 model (Fig. 7.12d) has approximately a doubling in the maximum size of the mainshock compared to the frac, and lin frac models and shows very little, if any, foreshock or aftershock sequences. Lastly, the time series of the rnd B16 model (Fig. 7.12e), which contains 25% asperities, shows a random and unpredictable large sized event much like the benchmark no asperity model. Although this model contains five times the percentage of asperities compared to the other structure models, its maximum magnitude is much less.

In the structure models, where clustering does occur for models frac, lin frac, and rnd B1, the predicted average physical time period between the cluster can be calculated in the same manner as the block models (Eq. 3.4) as $\bar{t}_{cluster} = n_{tot\,cell}(\sigma_{F_{asp}} - \sigma_R)\alpha = 1(11 - 0)0.05 = 0.55$. Therefore, the quiescence period between clusters for inhomogeneous models is governed by the failure and residual thresholds of the asperity cells, along with the dissipation parameter of the system.

An identical physical time cutoff ($t_{phys} = 15.2101$) is used for all structure models for the non-cumulative frequency-size distributions. Table 7.3 summarizes the total stress, or physical time, required for all models to complete 10^6 plate updates, along with the total plate updates completed given the physical time cutoff. Given that the frac, lin frac, and rnd B1 models have equal percentage of asperities the total physical time needed to complete all 10^6 plate updates is approximately identical. The rnd B16 model requires a greater amount of physical time to complete all plate updates due to the increased percentage of asperities.

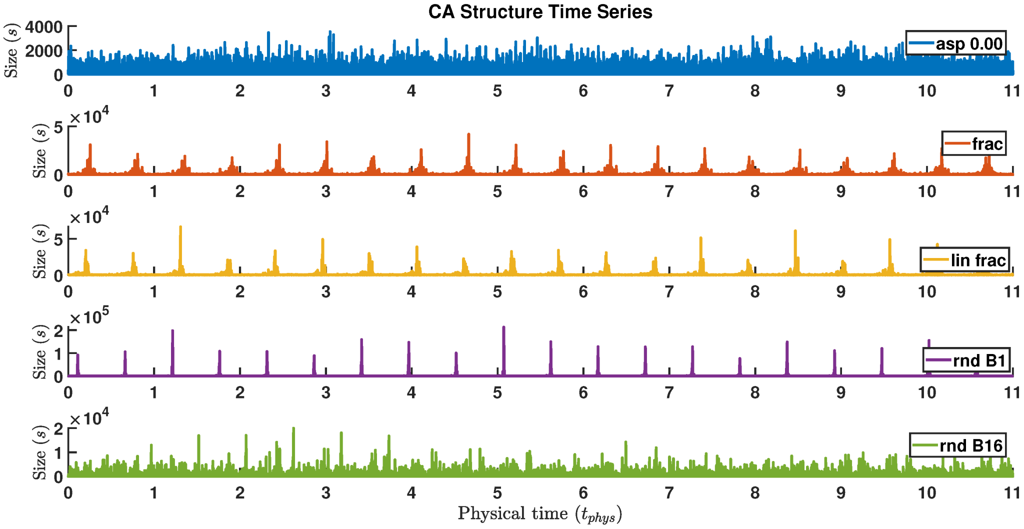

Figure 7.12: Physical time series of events (number of failed cells) for varied structure models, see legend, over 11 units of physical time. Formation of periodic and frequent earthquake clusters or swarm events are seen for the fracture (frac), linear fracture (lin frac), and block width 1 (rnd B1) models. Notably, the largest peaks sizes $s > 10^5$ are observed for the rnd B1 model. The block width 16 (rnd B16) model shows a random and unpredictable time series similar to the benchmark model. Model structures are shown in Figure 7.11. The benchmark homogeneous model with no asperities is the $asp = 0.00$ model.

Asperity block model	Total physical time for 10^6 plate updates	Total plate updates for $t_{phys} = 15.2101$
asp=0.00	15.2101	1,000,000
frac	16.0022	950,804
lin frac	16.0161	949,751
rnd B1	16.0267	949,194
rnd B16	19.9832	760,433

Table 7.3
Total stress added, proportional to physical time, to each structure block model over 10^6 plate updates and the total number of plate updates completed given a physical time cutoff of $t_{phys} = 15.2101$.

7.3.2 Frequency-Size Distribution

The non-cumulative frequency-size distributions for all of the inhomogeneous structure models are shown in Figure 7.13 with a physical time cutoff of $t_{phys} = 15.2101$. For structured asperity models we observe negligible decrease in the intercept (or seismogenic index) with the greatest changes being in the slope and the maximum expected size (magnitude). In particular, there is a reduction in the occurrence of small to large sized events ($10^1 < s < 10^3$) with a significant increase in the range and the maximum expected size (magnitude), particularly for the rnd B1 model. The rnd B16 model behaves differently to the other structure models, where we observe a decrease in the intercept while the slope remains similar to the previously examined CA block models. Unlike the CA block models, the CA structure models increase the slope, or b-value, in the non-cumulative frequency-size distribution.

The predicted MC structure models, plotted as diamonds, are calculated as the sum of individual homogeneous MC models (Eq. 4.32). Therefore, the predicted MC models for the frac, lin frac, and rnd B1 are identical as they all contain 5% of asperities. The MC models predict that greater percentages of asperities will decrease all seismicity while maintaining a constant slope. Conversely, the CA models suggest that the underlying asperity structures influence the slope and the maximum expected magnitude. Therefore, the discrepancies between the predicted MC models and the CA models suggest that these differences originate due to the interaction between the asperities and normal cells.

Shown in Figure 7.14 are the interevent plots of the mean physical time $\bar{t}_s$, solid color curve, between events of size s for all 10^6 plate updates where the dashed lines outline the third ($Q3$) and first ($Q1$) quartiles, respectively. For all structure models containing asperities, there is an increase in the mean physical time $\bar{t}_s$ (decreased occurrence) for events of size $s > 2 \times 10^1$ compared to the homogeneous model. As previously shown in Figure 7.13, the decrease of small sized events comes at the cost of increased maximum magnitudes. For small sized events $s < 2 \times 10^1$ the mean interevent physical time $\bar{t}_s$ for the frac, lin frac, rnd B1 and no asperity models behave very similarly. Furthermore, the frac, lin frac and rnd B1 models are nearly identical between the magnitude ranges of

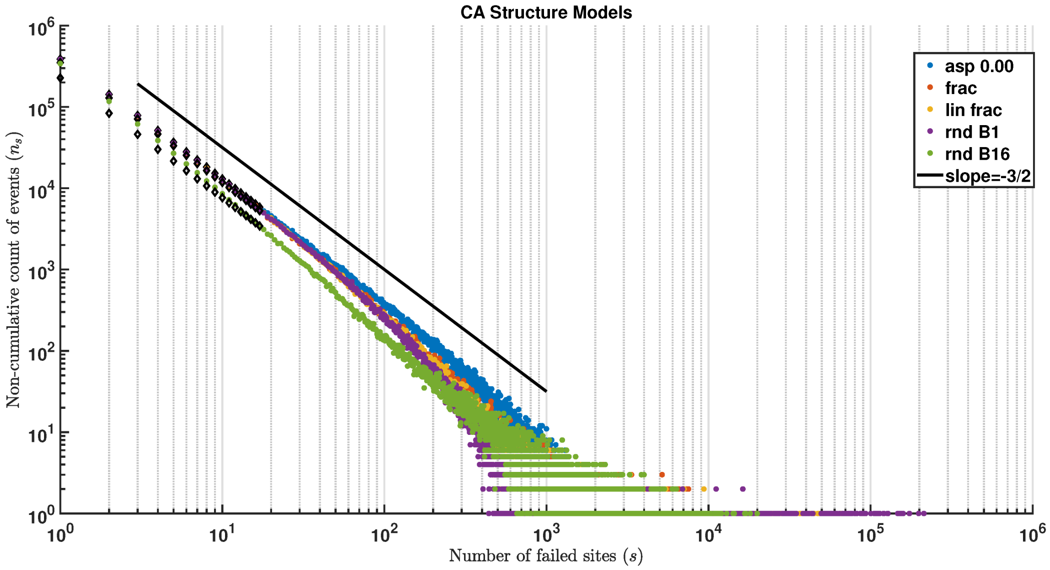

Figure 7.13: Non-cumulative frequency-size distribution as circles for CA structure models along with the predicted Markov chain distributions as black diamonds. Compared to the baseline model, the asperity structures increase the slope and the range of the maximum expected size (magnitude) while the intercept remains constant. The rnd B1 model generates the greatest maximum magnitudes ($s_{max} \approx 2 \times 10^6$) compared to all other structure models. For the rnd B16 model, there is a decrease in the intercept while the slope remains constant similar to the previous results examined for the block models. The CA structure models have a low dissipation parameter of $\alpha = 0.05$. The black line has a slope of $-3/2$ predicted from the scaling of OFC models with low dissipation and long range interactions.

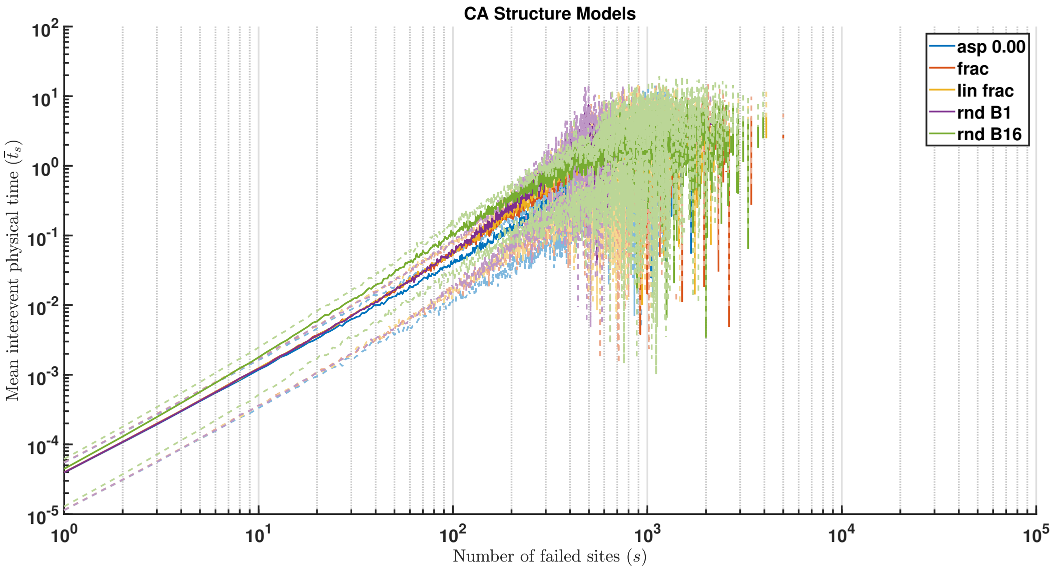

Figure 7.14: Mean interevent physical time $\bar{t}_s$ between events of size s for varied structure models. Top and bottom dashed lines represent the third and first quartiles, respectively, for a given curve. For all structure models containing asperities, there is an increase in the mean physical time $\bar{t}_s$ (decreased occurrence) for events of size $s > 2 \times 10^1$ compared to the homogeneous model. For models frac, lin frac, and rnd B1 the mean interevent physical time $\bar{t}_s$ curve is nearly identical between the magnitude ranges of $10^0 < s < 10^2$ with deviations at larger magnitudes. For the rnd B16 model there is an increase in the interevent physical time (decreased occurrence) for events of identical size s.

$1 < s < 10^2$ with deviations occurring between them at larger magnitude ranges $s > 10^2$. The rnd B16 model is more similar to the block models previously examined, where there is an increase in the interevent physical time (decreased occurrence) for events of identical size s.

7.4 System details

At the end of every 500-th of the total 10^6 plate updates we output a snapshot of the internal stresses of all cells and the lattice's inner plate failure sequence t_{in}, and cumulative failures of each cell for a total of 2×10^3 snapshots.

7.4.1 Internal Stress Distribution

Shown in Figure 7.15 are the internal stress snapshots, and their respective histograms, for models a) frac, b) lin frac, c) rnd B1, and d) rnd B16. The internal stress distributions for all asperity structures show greater variations, where a single asperity structure may have cells with low internal stresses (blue) and high internal stresses (yellow). Visually, we can identify a synchronization of internal stresses across asperities that appear to originate from earlier initiating asperity failure zone(s) (bright blue) as seen in the frac, lin frac and rnd B1 models. Effectively, the asperities structures are in communication with the surrounding asperity structures within the long range stress transfer of $R = 16$. Therefore, the temporal clustering observed in the times series would originate from one or more failure wavefronts that initiate in an asperity structure and propagate outwards towards the surrounding asperities.

For the structure model rnd B16 (Fig. 7.15d), the asperity blocks behave differently from the rest of the structured models and show an internal stress distribution more similar to the large block models previously examined. The internal stresses of the asperity blocks organize themselves into smaller block subsystems that behave similarly to the large block models previously examined. The internal stress distributions for the rnd B16 blocks show triggering fronts that form at the normal cells boundaries and propagate inwards into the asperity blocks. Therefore, the surrounding normal cells may load the asperity blocks at the boundaries, thus creating a triggering front that travels inward, or at times across, the block asperities.

The histogram of the internal stress distribution, Figure 7.16, shows that the asperities have a unimodal distribution with a peak at the center, whereas the internal stress distribution of the normal cells remains uniformly distributed. Looking at individual snapshots from Figure 7.15a-c, the internal stress distribution of the frac, lin frac and rnd B1 models show gaps in between $1 < \sigma_i < 1.6$, $1 < \sigma_i < 2$, and $1 < \sigma_i < 4$, respectively. Compared to the previously examined block models, the internal stresses of the structure asperities are more tightly clustered. This is most likely due to the low percentage (5%) of asperities within the system, as the rnd B16 model shows a greater spread in the internal stresses of the asperities. At the next plate update the minimum

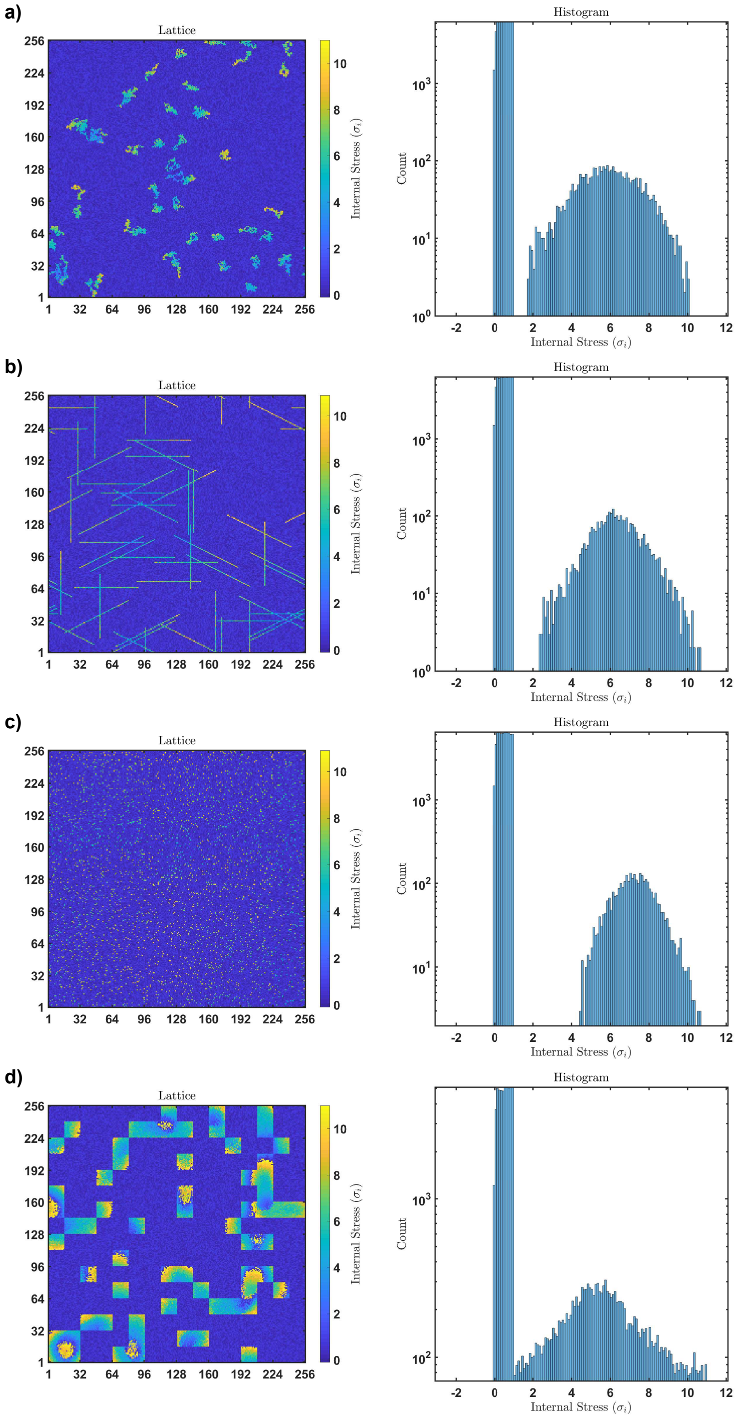

Figure 7.15: Internal stress snapshot shown on the left subplot with histogram (logarithmic scale) shown on the right subplot. From top to bottom, the plots are for models with structure of a) frac, b) lin frac, c) rnd B1, and d) rnd B16. Visually, we can identify a synchronization of internal stresses across the asperities that appear to originate from earlier asperity failure zone(s) (cyan blue). The internal stress distributions for the rnd B16 blocks show failure fronts that form at the normal cells boundaries and propagate inwards, or across, the asperity blocks.

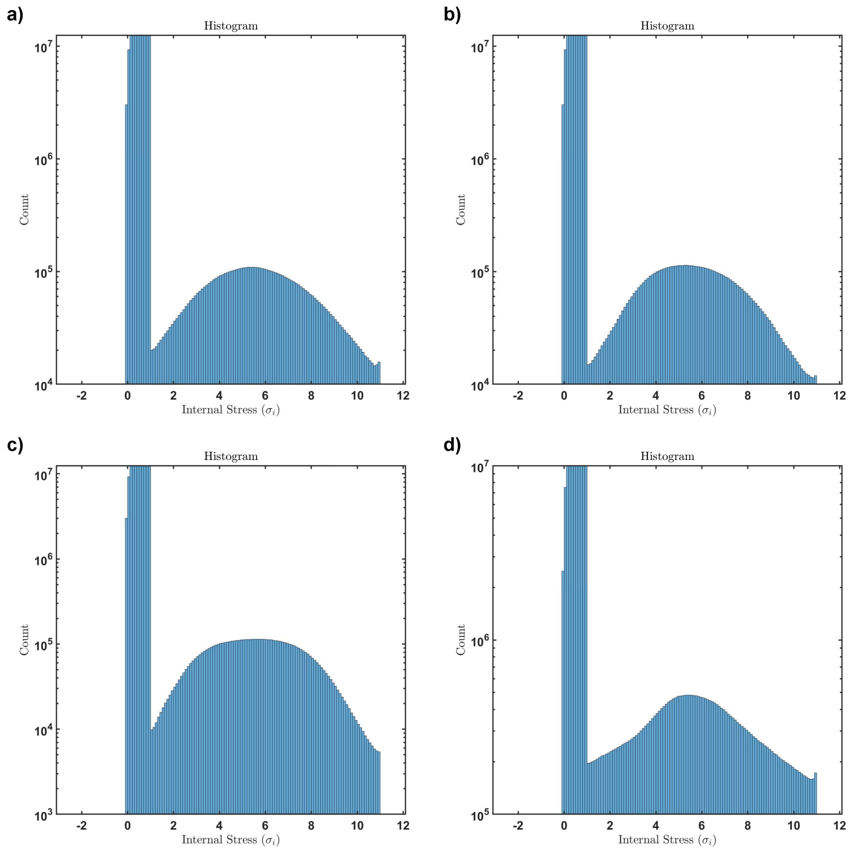

Figure 7.16: Cumulative internal stress histogram (logarithmic scale) for all 2×10^3 snapshots for structure models a) frac, b) lin frac, c) rnd B1, and d) rnd B16. In all cases, the internal stress distribution of the asperities is a unimodal distribution with a center peak, whereas the normal cells remain uniformly distributed.

stress $min(\sigma_F - \sigma_i)$ is added to each cell of the system, and the internal stress distribution of the asperities shifts towards the failure threshold of $\sigma_{F_{asp}} = 11.0$.

7.4.2 Avalanche Sequences

At the beginning of a plate update, a single failure event is induced which may develop into an avalanche of failed cells otherwise known as the slip history. The presence of structured asperities creates temporal clustering with varied foreshock, mainshock and aftershock sequences, as shown in the time series (Fig. 7.12). How does the spatial distribution of asperities surrounding weaker normal cells influence the avalanche sequences? Shown in Figure 7.17 are the three largest avalanche sequence from all 2×10^3 snapshots for the structure models a) frac, b) lin frac, c) rnd B1, and d) rnd B16. For the avalanche sequence, the failure of an asperity at a given inner plate update t_{in} is marked with a black circle.

From the structure models a) frac, b) lin frac, c) rnd B1, and d) rnd B16, the slip history is variable with the largest event in the sequence not necessarily corresponding to the failure of an asperity. The failure of asperities, black circles, are spread throughout the rupture sequences. Furthermore, an induced failure at $t_{in} = 1$ may begin at an asperity and propagate outwards, or it may initiate at a normal cell and make its way towards the asperities. This is better shown in Figure 7.18 with the spatial distributions of the three avalanche events, from left to right, for the structure models a) frac, b) lin frac, c) rnd B1, and d) rnd B16, from top to bottom. Each avalanche is initiated at the failed cell marked by the red circle, where the failures of normal cells are plotted in black and the failures of asperities are plotted in blue.

Examining both the avalanche sequences and the spatial distributions (Figures 7.17 and 7.18) shows that the initiating failures do not necessarily correspond to the center of the failure cluster. Instead, the major cluster of failed cells tend to be around failed asperity cells due to the relatively large release of stress to the weaker surrounding normal cells. Furthermore, from all of the snapshots for all structure models, the avalanche sequences were found to always terminate within the weaker normal cells.

The fractal dimension D was fit for radius intervals of $1 \leq r \leq 20$ (small r), along with the standard error in the estimate, shown in Figure 7.19. For small radii, the fractal dimension of $D \approx 2$ suggests a random distribution in the location of the events. Given that the inhomogeneous structures are much less in length than the stress transfer range, the fractal dimension D effectively measures the random distribution of events due to the stress transfer range rather than the asperity structures.

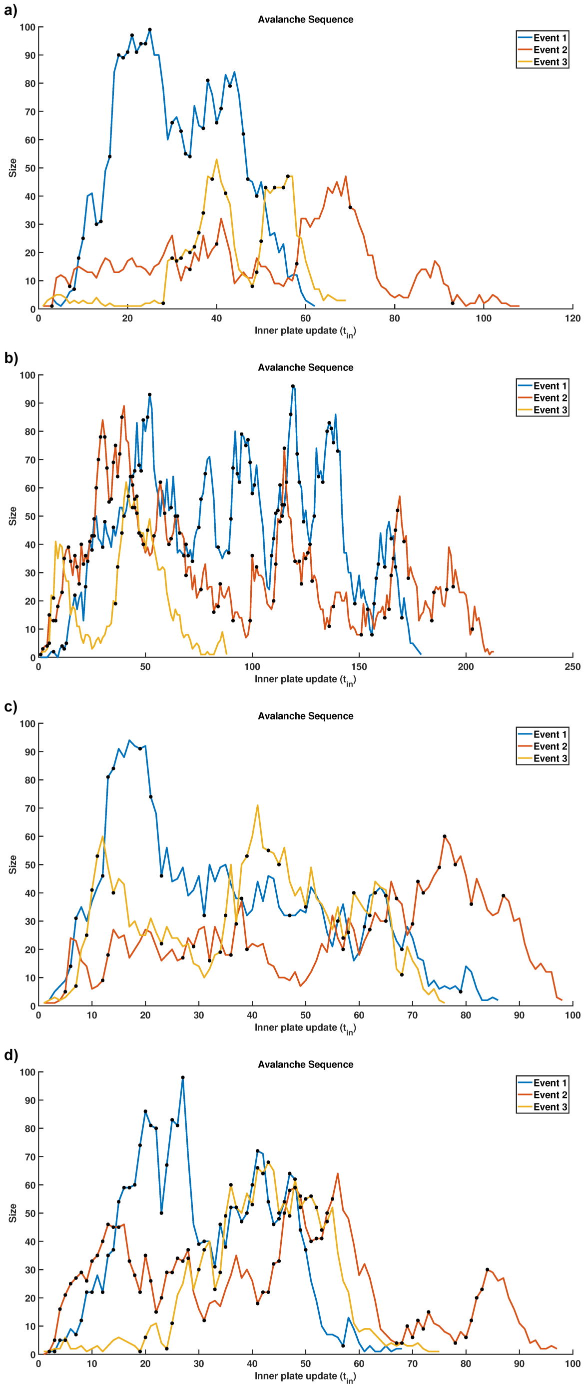

Figure 7.17: Size plotted against inner plate update time t_{in} of the three largest avalanche sequences from all 2×10^3 snapshots for structure models a) frac, b) lin frac, c) rnd B1, and d) rnd B16. For the avalanche sequences, the failure of an asperity at a given inner plate update t_{in} is marked with a black circle. The slip sequences are highly variable with the failure of asperities spread throughout the avalanche. As an asperity fails it may induce failure in nearby asperities.

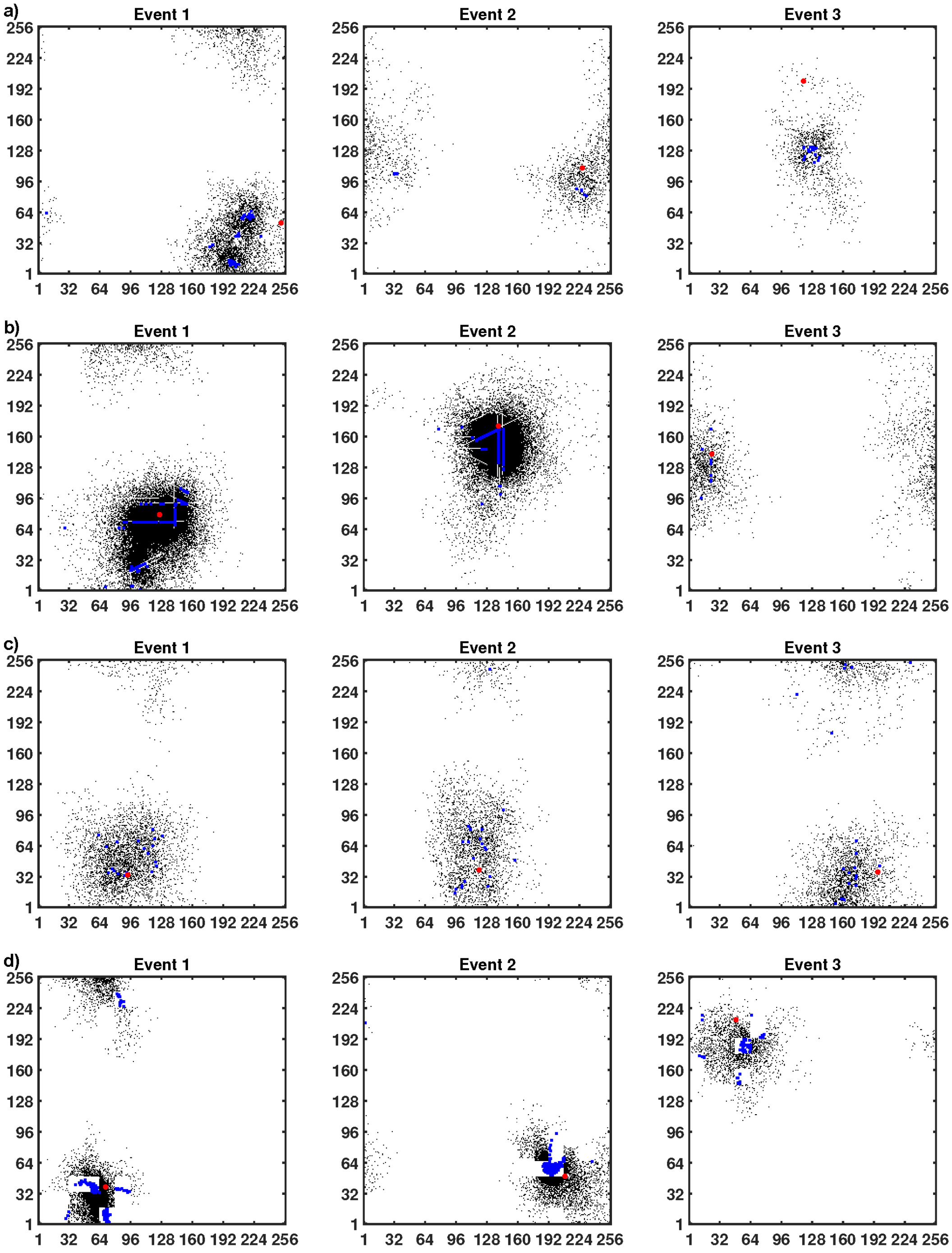

Figure 7.18: Spatial distributions of the three avalanche events, from left to right, for the structure models a) frac, b) lin frac, c) rnd B1, and d) rnd B16, from top to bottom. Each avalanche is initiated at the failed cell marked by the red circle, where the failures of normal cells are plotted in black and the failures of asperities are plotted in blue. Large clusters of failed cells tend to be around asperity structures.

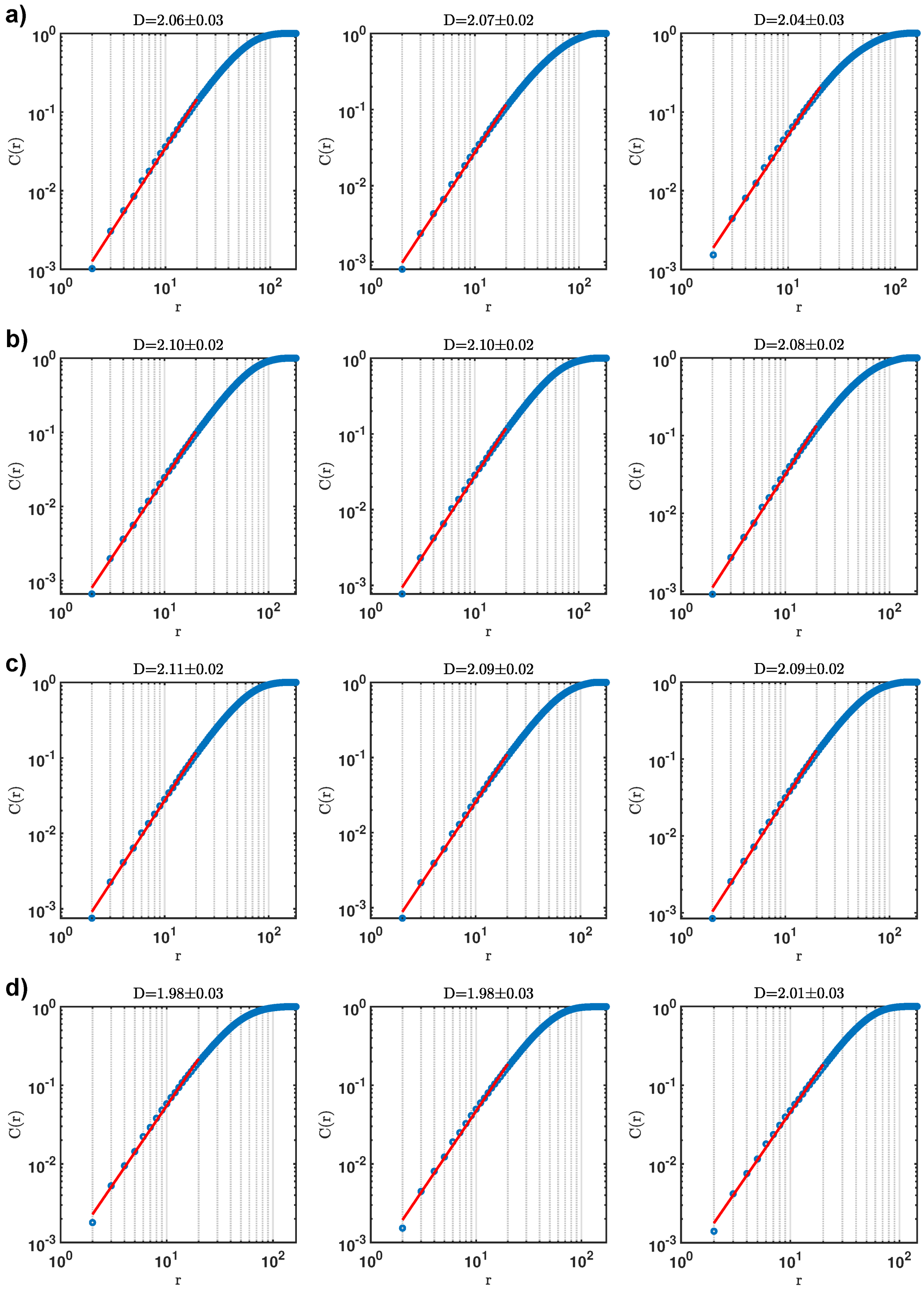

Figure 7.19: Correlation integral $C(r)$ versus distance r for each of the three largest avalanche sequences, left to right, from all 2×10^3 snapshots for structure models a) frac, b) lin frac, c) rnd B1, and d) rnd B16, from top to bottom. The fractal dimension D, shown in figure title bar with uncertainty, is determined from the slope, shown as a red line, fitted over a linear part of the curve $1 \leq r \leq 20$.

Asperity model	Total physical time for 10^6 plate updates	Mean total failures from CA model	Total failures concept model
frac	16.0022	310.69 ± 12.96 (nrm) 29.00 ± 0.04 (asp)	320.04 (nrm) 29.09 (asp)
lin frac	16.0161	303.87 ± 15.72 (nrm) 29.00 ± 0.06 (asp)	320.32 (nrm) 29.12 (asp)
rnd B1	16.0267	272.81 ± 18.48 (nrm) 29.01 ± 0.12 (asp)	320.53 (nrm) 29.14 (asp)
rnd B16	19.9832	383.86 ± 19.18 (nrm) 36.19 ± 0.40 (asp)	399.66 (nrm) 36.33 (asp)

Table 7.4
Total stress added, proportional to physical time, to each structure model over 10^6 plate updates. The table includes the mean and standard deviation of the cumulative number of individual cell failures for normal cells (nrm) and asperity cells (asp) from the CA model, and the cumulative number of individual cell failures calculated from the simplified self-interacting conceptual model (Eq. 3.4). The dissipation parameter $\alpha = 0.05$ and residual threshold $\sigma_R = 0.0$ remain constant between the structure models.

7.4.3 Model Expectancies

All of the CA models are simulated for a total of 10^6 plate updates for which we track the cumulative failures of each cell in intervals of 500 plate updates. The results for the total number of failures for an individual cell $n_{tot\,cell}$ at the end of all 10^6 plate updates from our CA model results and the simplified self-interacting conceptual model (Eq. 3.4) are summarized in Table 7.4. The failure thresholds of the asperity cell $\sigma_{F_{asp}} = 11.0$ and normal cell $\sigma_F = 1.0$ vary depending on the cell, along with the total physical time t_{phys} taken to complete all 10^6 plate updates, while the dissipation parameter $\alpha = 0.05$ and residual threshold $\sigma_R = 0.0$ remain constant. Likewise, the cumulative number of individual cell failures over 10^6 plate updates for all of the inhomogeneous structure models are shown in Figure 7.10.

From Table 7.4, the mean cumulative number of normal cell failures decreases from the frac, lin frac, and rnd B1 models, although all three models have approximately 5% asperities with nearly identical total physical time needed to complete 10^6 plate updates. Therefore, the spatial distribution of structure asperities influences the failure statistics of the CA model. A decrease

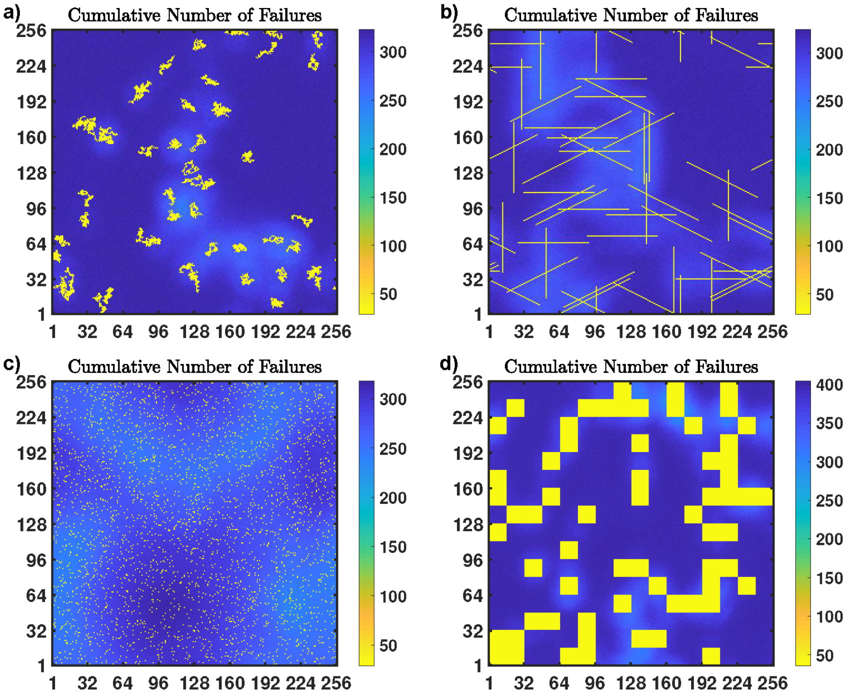

Figure 7.20: Cumulative number of failures for each cell over 10^6 plate updates for structure models a) frac, b) lin frac, c) B1, and d) B16. Low cumulative number of failures appear to be in areas with larger asperity density.

in the mean total number of failures for a normal cell would suggest a deficit of stress flowing into the normal cell resulting in lower cumulative failures. As shown in Figure 7.20, the cumulative number of failures for the normal cells is strongly decreased at the borders of certain but not all asperity structures. For the frac, lin frac, rnd B1, and rnd B16 models the cumulative number of failures for the normal cells found at the boundaries of the asperities can be as low as $n_{tot_{cell}} = 242, 256, 231,$ and 284, respectively. Given that the asperities fail less often than the normal cells, it is expected that the normal cells at the asperities have a reduced total number of failures, yet some clusters show a greater deficit. Most likely, some asperity structures spatially distribute themselves into a more effective barrier geometry, or stress sink, and inhibit the propagation of avalanches through the neighboring normal cells.

Chapter 8

Discussion

8.1 Homogeneous Models

8.1.1 Cellular Automaton

From the CA homogeneous time series, see Fig. 5.1, the average size event is governed by a system's ability to dissipate stress. As a system's dissipation parameter α decreases, the average size event s increases. Therefore, greater stress dissipation supresses the occurrence of larger events while increasing the occurrence of smaller events; this is highlighted in the non-cumulative frequency-size distributions of Figure 5.2.

The non-cumulative frequency-size distribution is a Gutenberg-Richter like relation, see Equation 2.4, between an s size event and its measure of frequency n_s. The frequency-size distributions for the homogeneous models (Fig. 5.2) confirm that as the stress dissipation parameter α increases larger size events occur less frequently, while the occurrence of smaller events increases. The intercept of the frequency-size distribution has been interpreted as a system's capacity to generate earthquakes, analogous to the a-value from the GR relation. Likewise, the slope, or b-value, of the scaling relation determines the relative frequency of large events versus smaller events.

In terms of seismology, the homogeneous CA models would suggest that a dissipative system has an increase in both the slope (b-value) and intercept (a-

value), meaning that a greater proportion of small sized events are generated over large sized events. We note that as the dissipation parameter decreases, the distribution approaches a constant slope of $-3/2$, as suggested for an OFC model with low dissipation and long range interactions (Klein et al., 1997). As an aside, it has been observed that for CA models the number of earthquakes n_s with s size events exhibit power law scaling of $n_s \sim s^{-3/2}$ with some authors suggesting that earthquake dynamics can be described by equilibrium statistical mechanics (Klein et al., 1997, 2000).

Often ignored is the context of timescales within the CA models. In terms of seismic hazard, the probability that an event will occur within a given time window is necessary in risk assessment. In our model two timescales exist, the plate update time t_{pu} and the physical time t_{phys}. The plate update time t_{pu} is an iterative step used to simulate the model, whereas the physical time t_{phys} is related to the amount of stress added at each plate update time t_{phys} used as a non-dimensional time proxy, see Equation 3.1.

This allows us to examine the mean interevent time $\bar{t}_s$ (or period) between s sized events for all homogeneous CA models, as shown in Figure 5.3. For all homogeneous CA models, the interevent plot suggests that on average the time between small sized events is less than for larger sized events. A system's ability to generate larger sized events depends on the dissipation parameter α, but the interevent plot suggests that the average period between that system's largest sized events is nearly identical across all homogeneous models. Therefore, a system with a high dissipation parameter generates small sized events more frequently, but not large sized events.

We find that the internal stresses of the homogeneous CA models are approximately uniformly distributed between $\sigma_R + \eta < \sigma_i < \sigma_F$, as shown in Figures 5.4 and 5.5. Between the range of $-\eta < \sigma_i < +\eta$ the internal stress distribution is primarily governed by the implementation of noise within the model. At the beginning of a plate update time the minimum stress $min(\sigma_i - \sigma_F)$ is added to the entire system, thus shifting the histogram towards σ_F. Although all homogeneous CA models have nearly identical internal stress distributions the dynamics of the system after a failure are different. Once a failure occurs $(\sigma_i \geq \sigma_F)$, a fraction of the stress $(1 - \alpha)[\sigma_i - \sigma_R]$ is redistributed equally to neighboring cells, therefore a system with a lower dissipation parameter can bring a greater number of cells to failure. As a note, the internal stress distribution of a system with a dissipation parameter of $\alpha = 1.00$ is entirely governed by the initialized internal stress distribution as no stress transfer occurs during simulation.

Within the CA model the transfer of energy occurs within two timescales, the plate update time t_{pu} (slow loading rate) and the inner plate update time t_{in} (fast energy release). The inner plate update time t_{in} would represent the rupture sequence that occurs during the slip of an earthquake. We find that the avalanche sequences are highly variable with the main event, or peak slip, occurring anytime during the slip history, see Figure 5.6. This suggests that the variations in the slip history do not necessarily originate from heterogeneities (variations in failure strength) but can originate within a homogeneous medium as variations in internal stresses. Furthermore, we examined the spatial clustering of the avalanche sequences, shown in Figure 5.7, and find that the cluster may propagate away from the initially induced failure. Often, the rupture initiation point (red circle) is not the center of the total rupture area. The size of the cluster greatly depends on the system's dissipation parameter.

In seismology, the fractal dimension (D-value) has been used to investigate the spatial characteristics in the failure of events, see Equations 3.6 and 3.7. For the homogeneous CA models, we find that the fractal dimension for clusters is approximately equal to $D = 2$ within a radius interval of $1 \leq r \leq 20$. This suggests that the events are approximately randomly distributed within the two-dimensional model, which is expected given that the internal stress of the CA models are themselves uniformly distributed (Figure 5.4). Lastly, we find that the mean total failures of an individual cell within the CA model closely matches those of a simplified concept model, see Table 5.2. This suggests that the system behaves uniformly without any preferential flow of stress towards a particular region.

8.1.2 Markov chain Monte Carlo

Fundamentally, Markov chains are governed by the transition matrices. By assuming a stationary and uniformly distributed internal stress distribution we statistically replicated the time series, frequency-size distributions and interevent times between events for a much more complex CA model. The time series were shown to have identical size scaling across all dissipation parameters α, and the analytically derived frequency-size distribution and MCMC sampling algorithm are in good agreement with the CA model, see Figures 6.2 and 6.3, respectively. Furthermore, the mean interevent physical time between events of size s (Fig. 6.4) can be said to be identical between the MCMC and CA models.

Where discrepancies are observed is in the total physical time needed to complete equivalent plate updates t_{pu} as a function of the dissipation parameter α. We expect that a system with a low dissipation parameter is on average closer to failure compared to a more dissipative system. This is true of the CA models (Table 5.1), where the average physical time required to complete 10^6 plate update times systematically increases with increasing dissipation parameter. Therefore, on average the internal stress distribution for low dissipation systems is ever so slightly closer to the failure threshold. For the MCMC sampling algorithm, the internal stress distribution is assumed to be constant regardless of dissipation parameter, and thus it is unable to capture this distinction, see Table 6.1.

Nonetheless, examining the CA process as a Markov process offers important statistical inferences. Examining the transition matrices of 6.1 suggests that the avalanche sequences, or Markov chains, are more probable to develop along a preferred path. For large sequences it is more probable that an avalanche sequence steadily increases and decreases. As the dissipation parameter α decreases the avalanche sequence has increased probabilities to stay at the same state or to transition to a greater state. Inversely, for high dissipation parameters the avalanche sequence is much more probable to transition to a lower state with some states becoming practically unreachable. Because some avalanche sequences are more probable than others, it is likely that the spread observed in the non-cumulative frequency-size distribution for large s events sizes is due to the probabilistic nature of the system rather than a sampling issue (Fig. 6.3).

Lastly, the cutoff size at large event sizes s in the frequency-size distribution has been suggested to be a finite size effect of the CA models (Olami et al., 1992). The cutoff size effect is illustrated in Figure 6.3 for both MCMC (circle) and CA (cross) models. It is interesting to note that we also observe a cutoff size for the MCMC models despite that the model is a Monte Carlo sampling method (flowchart Figure 4.4). Within the MCMC model, the Markov chain is not bound by system size, but instead continues until it is absorbed into state S_0. This would suggest that the cutoff size in the non-cumulative frequency-size distribution is due to the dissipative nature of the system, rather than a finite size effect. Lastly, in this study we have calculated an analytical non-cumulative frequency-size distribution for both the block and structure inhomogeneous models, but no Markov chain Monte Carlo models. As discussed below, predicting the behavior of mixed systems is more complicated as the interaction between heterogeneities leads to a non-stationary internal stress distribution.

8.2 Inhomogeneous Models

Within our model, asperities have increased failure thresholds relative to the surrounding cells ($\sigma_{F_{asp}} > \sigma_F$), therefore these heterogeneities increase the hardness of the system. When an asperity cell does fail, it redistributes a greater amount of stress to its neighboring cells relative to the failure of a normal cell. If the asperity is surrounded by normal cells, this would result in a larger than average cluster of failed normal cells. What is interesting is the occurrence of temporal clustering that is produced as larger events build up (foreshock) or gradually decrease (aftershock) after the main shock (largest size event) across multiple plate update times. In nature, various seismicity patterns are observed before major earthquakes, such as foreshocks, preseismic quiescence, precursory swarms and these provide some clue about the state of stress in the fault zone (Kanamori, 1981).

8.2.1 Block Models

The physical time series of Figure 7.2 show the presence of swarm events or temporal clustering, particularly for block models $asp = 0.50$, 0.75, and 1.00. These three models show temporal clusters with foreshock, mainshock, and aftershock sequences that vary in shape. A common feature between the block models is the quiescence period between clusters. We find that the average physical time period $\bar{t}_{cluster}$ between clusters is given as $\bar{t}_{cluster} = (\sigma_{F_{asp}} - \sigma_R)\alpha$, which accounts for the total stress required to fail an asperity $(\sigma_{F_{asp}} - \sigma_R)$ and the dissipation parameter α of the model. As the percentage of asperities, or model hardness, increases so does the physical time required to generate an equivalent catalogue of 10^6 events, as shown in Table 7.1.

The non-cumulative frequency-size distributions of the CA block models, Figure 7.3, suggest that the seismogenic index and probability of small sized events ($s<10^3$) decreases as the percentage of asperities increases. Likewise, the predicted Markov chain models, diamonds, would support the idea that as the percentage of asperities increase the seismicity of the system (a-value) decreases while the slope (b-value) remains identical. For the $asp = 1.00$ model, we observe a change in slope between the range of $10^1 < s < 10^2$, which is highlighted in the interevent time plot, Figure 7.4. Although the $asp = 1.00$ model is homogeneous, or without the presence of normal cells, we do not observe this behavior for the no asperity $asp = 0.00$ model. From Figure 7.4, we find that the mean physical time $\bar{t}_{cluster}$ between events of size s increases as the percentage of asperities increases. As an aside, we find that the slope discrepancy observed in the $asp = 1.00$ block model is removed if system noise η is set as a fraction of a cell's failure threshold $(\sigma_R = 0.0 \pm \eta \times \sigma_{Fasp})$ rather than a fixed noise level $(\sigma_R = 0.0 \pm \eta)$. Further in this chapter, we discuss how low noise affect the behavior of the CA model.

From the snapshots of the block models, Figures 7.5 and 7.6, we find that the internal stresses of the asperities are not uniformly distributed as the normal cells. From Figure 7.5, the internal stresses of all asperity block models show a triggering front of cells with high internal stress (about to fail) followed by cells with low internal stress (previously failed). We find that these triggering fronts appear to travel away from the normal cells and inwards into the asperity block. Why do the internal stresses of asperities configure themselves as such? Given that the normal cells fail more regularly than the asperities, the failures of the normal cells at the boundary of the asperity blocks may act as a seed in defining the configuration of the internal stresses of the asperities. As suggested by Figure 7.10 and Table 7.2, there is a decrease in cumulative number of normal cell failures particularly at the boundaries of the asperity blocks. Lastly, the distance between these wavefronts is approximately the stress transfer radius of the system defined as $R = 16$.

From the avalanche sequences and spatial distributions of the CA block models, Figures 7.7 and 7.8, we find that failure may begin at an asperity and propagate along other asperities or normal cells. Likewise, failure may initiate at a normal cell and propagate at the boundaries of the asperities that may or may not fail. From the avalanche sequences, if an asperity cell does fail it is more likely that other asperities will subsequently fail given their close proximity. Equally, if an avalanche sequence does reach the normal cells than the avalanche sequence will likely end within the weaker normal cells. For the spatial distribution of events, we find that a fractal dimension of $D \approx 2$ for radius intervals of $1 \leq r \leq 20$, see Figure 7.9. Within a radius interval less than the stress transfer ($r < R$), the spatial distribution of events is uniformly randomly distributed. For the $asp = 1.00$ block model, the slope of the correlation integral $C(r)$ reflects the linear spatial distribution of events at larger radii ($r > 20$), see Figures 7.7 and 7.8.

8.2.2 Role of structure

We further investigated the effects of inhomogeneities by varying their spatial distributions in more complex structures, see Figure 7.11. As shown in the time series of Figure 7.12, the foreshock, mainshock and aftershock sequences vary depending on the asperity structure. This suggests that spatial distributions of inhomogeneities play a key role in the observed earthquake sequences. Although models frac, lin frac, and rnd B1 contain 5% asperities their physical time series are quite different from the no asperity model. In particular, the rnd B1 structure model generates the largest sized events ($s_{max} \approx 10^5$) compared to the frac, and lin frac models ($s_{max} \approx 5 \times 10^4$).

Similar to the CA block models, we find that the quiescence period between clusters is governed by the failure and residual thresholds of the asperity cells, along with the dissipation parameter of the system. Therefore, the average physical time period between clusters is given as $\bar{t}_{cluster} = 0.55$, just as observed in the CA block models.

From the non-cumulative frequency-size distribution, see Figure 7.13, we observe that as the percentage of asperities increases there is a slight decrease in small to medium sized events ($s < 10^3$), but an increase in the range of larger size events ($s > 10^3$). From the interevent plots, Figure 7.14, we observe an increase in the mean physical time $\bar{t}_s$ (decreased occurrence) for events of size $s > 2 \times 10^1$ compared to the homogeneous model. Furthermore, the structure models frac, lin frac, and rnd B1 are nearly identical at small magnitude ranges ($1 < s < 10^2$) but begin to deviate at greater magnitudes. The rnd B16 model behaves more similar to the previously discussed block models, where we observe a decrease in the occurrence of small size events ($s < 10^3$), but an increase in the maximum expected magnitude. All structures models require additional physical time to complete 10^6 plate updates times relative to the no asperity model ($asp = 0.00$), as shown in Table 7.3. The physical time needed to complete 10^6 plate updates is nearly identical between the frac, lin frac, and rnd B1 models, which all contain 5% asperities.

The predicted MC structure models, plotted as diamonds, are calculated as the sum of individual homogeneous MC models, see Equation 4.32. Therefore, the predicted MC models for the frac, lin frac, and rnd B1 are identical. The MC models suggest that greater percentages of asperities will decrease the seismogenic index (a-value) while maintaining a constant slope (b-value). Conversely, the CA models suggest that the underlying asperity structures influence the slope and the maximum expected magnitude. Therefore, the discrepancies between the predicted MC models and the CA models suggest that these differences originate due to the interaction between the asperities and normal cells rather than a combination of two independent systems.

Similar to the previously examined block models, we find that the internal stresses of the structure asperities are not uniformly distributed, see Figures

7.15 and 7.16. Rather, the internal stresses of the asperities are more tightly clustered around a unimodal distribution. At the next plate update time t_{pu}, the minimum stress $min(\sigma_F - \sigma_i)$ is added to the entire system and the internal stresses of the asperities shift toward the failure threshold $\sigma_{F_{asp}}$. Therefore, the origin of the clustering observed in the time series would be the results of the internals stresses of the asperities reaching the failure threshold $\sigma_{F_{asp}} = 11.0$ and sequentially failing.

Yet, the spread in internal stresses of the asperities (Fig. 7.15) does not explain how the inhomogeneities fail in such a short period of physical time, as observed in their times series (Fig. 7.12). Necessarily, once asperities beginning to fail a self-reinforcing process is initiated where asperities within the stress redistribution radius are also quickly brought to failure. This would suggest that time series clustering is influenced by the distribution of asperities, the stress transfer range and the dissipation parameter of the system. We note that although the asperities are scattered throughout the lattice their internal stresses are coordinated among each other, as shown in Figure 7.15.

From the avalanche sequences and spatial distributions of the CA structure models, Figures 7.17 and 7.18, we find that failure sequences patterns behave similar to those of the CA block models. Therefore, a failure may begin at an asperity and propagate along other asperities or normal cells. Likewise, failure may initiate at a normal cell and propagate at the boundaries of the asperities that may or may not fail. From the avalanche sequences, if an asperity cell does fail it is more likely that other asperities will subsequently fail given their close proximity. Since the asperity structures are surrounded by weaker normal cells, we find that all of the structure models avalanche sequences end within the normal cells.

For the spatial distribution of events, we find that a fractal dimension of $D \approx 2$ for radius intervals of $1 \leq r \leq 20$, see Figure 7.19. Given that the inhomogeneous structures are much less in length than the stress transfer range, the correlation dimension D effectively measures the random distribution of events due to the stress transfer range rather than the asperity structures. Lastly, Table 7.4 and Figure 7.20 suggest that some asperity structures spatially distribute themselves into a more effective barrier geometry, or stress sink, and therefore inhibit seismicity in surrounding regions. Table 7.4 would also suggest that a large deficit in the total failure of normal cells, and thus greater stress flow into the asperity cells, hardly increases the mean failures of the asperity cells.

8.2.3 Low noise and asperities

Examining the system details of both the CA block and structure models reveals that the internal stresses of the asperities are synchronized among themselves, see Figures 7.5 and 7.15. Therefore, once the majority of asperities are on the verge of failure a triggering front makes it way across the system setting off a cascade of asperities into synchronized failure. These cascading failures are the origin of the temporal clusters observed within the time series for both inhomogeneous models, see Figures 7.2 and 7.12.

The question becomes, why are the internal stresses of the asperities synchronized? To answer this question, we examine again the implementation of noise. Within our CA models, noise added to the residual stress was kept fixed at $\sigma_R \pm 0.1$ for both the normal cells and the asperity cells. Effectively, for a normal cell the noise is set to 10% of the failure threshold, whereas for an asperity cell the noise is approximately 0.9% of its failure threshold. Gu (2016) has studied the OFC models under low noise conditions and finds that noise affects the queue-jumping hypothesis and the mixing of phase space.

The principal of the queue-jumping hypothesis is as follows. At each plate update a cell with the minimum stress difference of $min(\sigma_i - \sigma_R)$ is brought to failure; therefore we can imagine that there is a certain order or queue in cell failures. After a cell's failure, the cell is re-assigned to the back of the line ($\sigma_i = \sigma_R \pm \eta$). With higher noise, the recently failed cell can jump within the queue, whereas with zero noise it must go to the back of the queue. Therefore, with very little noise η the periodicity in a cell's failure is much more constant.

The mixing of phase space refers to the total potential outcomes or configurations that a system may evolve through. Under low noise or zero noise, the dynamics of the system are restricted to evolve along a nearly identical pathway. Therefore, a low noise system does not have access to all of the probability space. Within our CA model, this would suggest that a system under very low noise will not have access to a set of avalanche sequences. This might explain the increased spread observed in the non-cumulative frequency-size distribution for the $asp = 1.00$ model relative to the other block models, see Figure 7.3.

Is low noise enough to explain the time clustering observed within the CA models? Not quite. Within a low noise environment, the periodicity in the failure of cells is greatly constrained, but not synchronized. The internal stresses may be synchronized as an initial condition. In our case, prior to simulation the internal stresses of each cell are uniformly randomly distributed between $-\eta < \sigma_i < \sigma_F$, where σ_F is the failure threshold of the normal cells ($\sigma_F = 1.0$) and not the asperity cells ($\sigma_{Fasp} = 11.0$). After the burn-in period of 2×10^6 plate updates, we observe that the internal stresses of the asperities internal may increase in spread as the system organizes itself into an equilibrium, see Figures 7.5 and 7.15.

Lastly, we have run the inhomogeneous CA structure models with low noise ($\eta \pm 0.1$), but with asperities internal stresses initialized between $-\eta < \sigma_i < \sigma_{F_{asp}}$ and find that no foreshock or aftershock sequences are observed within the time series. We also find that asperities with high noise ($\eta \pm 1.1$), but initial internal stresses of $-\eta < \sigma_i < \sigma_F$ do not produce foreshocks and aftershocks. This confirms that in order for time series clustering to occur within the inhomogeneous CA models, both low noise and a point of synchronization of the internal stresses of the asperities is required. Is it possible that an inhomogeneous model with randomly distributed internal stresses, but low noise can eventually synchronize? Perhaps with some external help, such as a catastrophic event that sweeps across the system. In nature, this would be equivalent to a large magnitude teleseismic earthquake. This concept has not been validated within our CA model.

Chapter 9

Conclusion and suggested future research

9.1 Conclusions

The cellular automaton model is a simple lattice model that is able to capture properties observed in natural fault systems. Through the dynamics of the CA model we can begin to understand the physical origins of the phenomena's observed in real earthquake faults.

The homogeneous CA models suggest that a system's ability to dissipate stress influences the observed scaling of the frequency-size distribution. A higher dissipation parameter increases both the slope, *b*-value, and the intercept, *a*-value, of the frequency-size distribution. Greater stress dissipation capabilities suppress the occurrence of larger events while increasing the occurrence of smaller events. We find that homogeneous CA models under moderate noise cannot replicate the spatiotemporal clustering within their time series. Within the homogeneous CA model, avalanche sequences show great variability within their slip histories. Once an event is induced, an avalanche sequence is controlled by areas with large concentrations of cells close to failure. Additionally, we find that the internal stress distribution of the homogeneous CA systems is approximately uniformly distributed.

Furthermore, we replicate the dynamics of the CA model with a Markov process. We construct a transition matrix by assuming an appropriate underlying stress distribution for the system. The transition matrix suggests that some transitions between states are more probable than others. Therefore, some event sizes are more likely to occur than others, thus providing insight into the origin of the spread observed at large sized events in the frequency-size distribution. Furthermore, the transition matrix allows us to calculate an analytical frequency-size probability distribution for each homogeneous model by summing the probability of outcome for every possible pathway leading up to a cumulative size of $S_{cum} = 17$. Moreover, we can repeatably simulate the Markov chains given our transition matrix to replicate the avalanche sequences, time series, frequency-size distribution, and interevent times between events.

We generally find that the MCMC model is in good agreement with the homogeneous CA models. The homogeneous CA model is shown to require less physical time to simulate as the dissipation parameter decreases, whereas the MCMC model does not. These are subtleties within the internal stress distribution of the CA models that are not captured by the MCMC model.

The role of asperities is complicated, but in general these inhomogeneities add rigidity to the system. Therefore, we find that as the percentage of asperities increases a greater amount of added stress is required to complete an equal number of plate updates. Overall, we observe a decreased occurrence of smaller sized events with an increased or extended range in the occurrence of largest sized events. We also determined that the extent of these changes is strongly influenced by the underlining heterogeneous structures. We find that asperities affect the overall shape and slope of the frequency-size relation, therefore suggesting that scaling depends on the underlying spatial distribution of heterogeneities.

Furthermore, the addition of asperities can introduce spatiotemporal clustering apparent in the physical time series and greatly contribute to increasing the range and expected maximum magnitudes. From examining the system details of inhomogeneous CA models, we conclude that necessary conditions of spatiotemporal clustering are low noise and synchronization of internal stresses between heterogeneities. This leads to a clustered internal stress distribution for the asperities, which can no longer be approximated by a uniform distribution. It follows that the predicted MC models cannot accurately predict the scaling of the inhomogeneous models.

Lastly, we find that the avalanche sequence may initiate within an asperity or a normal cell. Normal cell failures tend to be around failed asperities, as these asperities release a greater amount of stress back into the system. Moreover, avalanche sequences with the CA structure model are found to terminate within the weaker normal cells. We also find that some heterogeneous structures are more effective than others in acting as a barrier, or stress sink, and suppress the seismicity of surrounding areas. The precise role of structures is still under investigation, but the asperities size and shape appear to contribute greatly to changes in seismicity. Lastly, any future predictive models must try to capture the interaction that occurs between normal cells and inhomogeneities.

9.2 Suggested future research

The fields of cellular automata, self-organized criticality, and critical phenomena lead to many insights into complex processes such as earthquakes. Is it possible to create analytical predictions to forecast the time series, earthquake slip histories, and frequency-magnitude relation thus helping predict seismic hazard?

This thesis proposed a new statistical approach in studying the processes of the cellular automaton lattice model. In particular, it highlights the importance of knowing the distribution of stresses within a given system. Yet, predicting the expected behavior of mixed systems is more complicated as the interaction between heterogeneities are no longer negligible. Furthermore, under low noise conditions the internal stress distribution of asperities is no longer stationary. Therefore, more work is required to determine how factors such as stress transfer, stress dissipation, system noise, and spatial configurations affect the stress distribution as a function of time. Once the significance of each factor is understood, they can be implemented into a non-stationary Markov process to analyze in detail the dynamics of an evolving system.

Bibliography

Aki, K., 1984, Asperities, barriers, characteristic earthquakes and strong motion prediction: Journal of Geophysical Research: Solid Earth, **89**, 5867–5872.

Bak, P., and C. Tang, 1989, Earthquakes as a self-organized critical phenomenon: Journal of Geophysical Research: Solid Earth, **94**, 15635–15637.

Bak, P., C. Tang, and K. Wiesenfeld, 1987, Self-organized criticality: An explanation of the 1/f noise: Physical Review Letters, **59**, 381–384.

———, 1988, Self-organized criticality: Physical review A, **38**, 364.

Beyer, W. H., 1987, Chemical Rubber Compancy. CRC standard mathematical tables.

Birch, C. P., S. P. Oom, and J. A. Beecham, 2007, Rectangular and hexagonal grids used for observation, experiment and simulation in ecology: Ecological modelling, **206**, 347–359.

Brown, S. R., C. H. Scholz, and J. B. Rundle, 1991, A simplified spring-block model of earthquakes: Geophysical Research Letters, **18**, 215–218.

Burridge, R., and L. Knopoff, 1967, Model and theoretical seismicity: Bulletin of the seismological society of america, **57**, 341–371.

Candela, T., F. Renard, J. Schmittbuhl, M. Bouchon, and E. E. Brodsky, 2011, Fault slip distribution and fault roughness: Geophysical Journal International, **187**, 959–968.

Carlson, J., and J. Langer, 1989, Mechanical model of an earthquake fault: Physical Review A, **40**, 6470.

Carlson, J. M., J. S. Langer, B. E. Shaw, and C. Tang, 1991, Intrinsic properties of a Burridge-Knopoff model of an earthquake fault: Physical Review A, **44**, 884.

Castellaro, S., and F. Mulargia, 2001, A simple but effective cellular automaton for earthquakes: Geophysical Journal International, **144**, 609–624.

De Rubeis, V., R. Hallgass, V. Loreto, G. Paladin, L. Pietronero, and P. Tosi, 1996, Self-affine asperity model for earthquakes: Physical review letters, **76**, 2599.

Delouis, B., J.-M. Nocquet, and M. Vallée, 2010, Slip distribution of the February 27, 2010 Mw= 8.8 Maule earthquake, central Chile, from static and high-rate GPS, InSAR, and broadband teleseismic data: Geophysical Research Letters, **37**, L17305.

Dieterich, J. H., 1972a, Time-dependent friction as a possible mechanism for aftershocks: Journal of Geophysical Research, **77**, 3771–3781.

———, 1972b, Time-dependent friction in rocks: Journal of Geophysical Research, **77**, 3690–3697.

Dominguez, R., K. Tiampo, C. Serino, and W. Klein, 2013, Scaling of earthquake models with inhomogeneous stress dissipation: Physical Review E, **87**, 022809.

Fisher, M. E., 1967, The theory of equilibrium critical phenomena: Reports on progress in physics, **30**, 615.

Frohlich, C., and S. D. Davis, 1993, Teleseismic b values; or, much ado about 1.0: Journal of Geophysical Research: Solid Earth, **98**, 631–644.

Gabrielov, A., W. I. Newman, and L. Knopoff, 1994, Lattice models of failure: Sensitivity to the local dynamics: Physical Review E, **50**, 188.

Grassberger, P., and I. Procaccia, 1983, Measuring the strangeness of strange attractors: Physica D: Nonlinear Phenomena, **9**, 189–208.

Gu, X., 2016, Modified earthquake Olami-Feder-Christensen model with low noise and asperities: PhD thesis, Boston University.

Gutenberg, B., and C. Richter, 1955, Magnitude and energy of earthquakes: Nature, **176**, 795.

Gutenberg, B. U., and C. F. Richter, 1954, Seismicity of the earth and related phenomena.

Hirata, T., T. Satoh, and K. Ito, 1987, Fractal structure of spatial distribution of microfracturing in rock: Geophysical Journal International, **90**, 369–374.

Janosi, I., and J. Kertesz, 1993, Self-organized criticality with and without conservation: Physica A: Statistical Mechanics and its Applications, **200**, 179–188.

Kanamori, H., 1978, Quantification of earthquakes: Nature, **271**, 411.

———, 1981, The Nature of Seismicity Patterns Before Large Earthquakes: Earthquake Prediction: An International Review, **4**, 1–19.

Kanamori, H., and D. L. Anderson, 1975, Theoretical basis of some empirical relations in seismology: Bulletin of the seismological society of America, **65**, 1073–1095.

Kazemian, J., 2013, Spatial heterogeneities in a simple earthquake fault model: PhD thesis, University of Western Ontario.

Kazemian, J., K. Tiampo, W. Klein, and R. Dominguez, 2015, Foreshock and aftershocks in simple earthquake models: Physical review letters, **114**, 088501.

Kazemian, J., and M. van der Baan, 2015, What is the effect of pore pressure on earthquake cycles: Technical report. (unpublished).

Kemeny, J. G., and J. L. Snell, 1960, Finite markov chains: Princeton, N.J., Van Nostrand.

Klein, W., M. Anghel, C. Ferguson, J. Rundle, and J. Sá Martins, 2000, Statistical Analysis of a Model for Earthquake Faults with Long-Range Stress Transfer: Geocomplexity and the Physics of Earthquakes, **120**, 43–71.

Klein, W., H. Gould, N. Gulbahce, J. Rundle, and K. Tiampo, 2007, Structure of fluctuations near mean-field critical points and spinodals and its implication for physical processes: Physical Review E, **75**, 031114.

Klein, W., H. Gould, K. Tiampo, J. B. Silva, T. Gu, J. Kazemian, C. Serino, and J. Rundle, 2017, Statistical mechanics perspective on earthquakes, *in* Avalanches in Functional Materials and Geophysics: Springer, 1–18.

Klein, W., J. Rundle, and C. Ferguson, 1997, Scaling and nucleation in models of earthquake faults: Physical review letters, **78**, 3793.

Lay, T., H. Kanamori, and L. Ruff, 1982, The Asperity Model and the Nature of Large Subduction Zone Earthquakes: Earthquake Prediction Research, **1**, 3–71.

Monette, L., and W. Klein, 1992, Spinodal nucleation as a coalescence process: Physical review letters, **68**, 2336.

Nakanishi, H., 1990, Cellular-automaton model of earthquakes with deterministic dynamics: Physical Review A, **41**, 7086.

———, 1991, Statistical properties of the cellular-automaton model for earthquakes: Physical Review A, **43**, 6613.

Naylor, M., K. Orfanogiannaki, and D. Harte, 2010, Exploratory data analysis: Magnitude, space, and time: Community Online Resource for Statistical Seismicity Analysis, **3**, 1–42.

Olami, Z., H. J. S. Feder, and K. Christensen, 1992, Self-organized criticality in a continuous, nonconservative cellular automaton modeling earthquakes: Physical review letters, **68**, 1244.

Omori, F., 1894, On after-shocks: Seismological journal of Japan, **19**, 71–80.

Otsuka, M., 1972a, A chain-reaction-type source model as a tool to interpret the magnitude-frequency relation of earthquakes: Journal of Physics of the Earth, **20**, 35–45.

———, 1972b, A simulation of earthquake occurrence: Physics of the Earth and Planetary Interiors, **6**, 311–315.

Pacheco, J. F., C. H. Scholz, and L. R. Sykes, 1992, Changes in frequency–size relationship from small to large earthquakes: Nature, **355**, 71.

Papoulis, A., and S. U. Pillai, 2002, Probability, random variables, and stochastic processes: Tata McGraw-Hill Education.

Patel, A., 2018, Red Blob Games - Hexagonal Grids: `https://www.redblobgames.com/grids/hexagons/`. (Accessed: 2018-10-30).

Pelletier, J. D., 2000, Spring-block models of seismicity: Review and analysis of a structurally heterogeneous model coupled to a viscous asthenosphere: Geophysical monograph, **120**, 27–42.

Pishro-Nik, H., 2014, Introduction to probability, statistics, and random processes: `https://www.probabilitycourse.com`. (Accessed: 2018-10-30).

Ramos, O., E. Altshuler, and K. Måløy, 2006, Quasiperiodic Events in an Earthquake Model: Physical review letters, **96**, 098501.

Richter, C. F., 1935, An instrumental earthquake magnitude scale: Bulletin of the Seismological Society of America, **25**, 1–32.

Rundle, J., and W. Klein, 1995, Dynamical segmentation and rupture patterns in a” toy” slider-block model for earthquakes: Nonlinear Processes in

Geophysics, **2**, 61–79.

Rundle, J. B., and S. R. Brown, 1991, Origin of rate dependence in frictional sliding: Journal of statistical physics, **65**, 403–412.

Rundle, J. B., and D. D. Jackson, 1977, Numerical simulation of earthquake sequences: Bulletin of the Seismological Society of America, **67**, 1363–1377.

Rundle, J. B., and W. Klein, 1993, Scaling and critical phenomena in a cellular automaton slider-block model for earthquakes: Journal of statistical Physics, **72**, 405–412.

Serino, C., W. Klein, and J. Rundle, 2010, Cellular automaton model of damage: Physical Review E, **81**, 016105.

Serino, C., K. Tiampo, and W. Klein, 2011, New approach to Gutenberg-Richter scaling: Physical review letters, **106**, 108501.

Thirumalai, D., and R. D. Mountain, 1993, Activated dynamics, loss of ergodicity, and transport in supercooled liquids: Physical Review E, **47**, 479.

Tiampo, K., J. Rundle, W. Klein, J. Holliday, J. S. Martins, and C. Ferguson, 2007, Ergodicity in natural earthquake fault networks: Physical Review E, **75**, 066107.

Tiampo, K., J. Rundle, W. Klein, J. S. Martins, and C. Ferguson, 2003, Ergodic dynamics in a natural threshold system: Physical review letters, **91**, 238501.

Turcotte, D., 1999, Seismicity and self-organized criticality: Physics of the Earth and Planetary Interiors, **111**, 275–293.

Utsu, T., Y. Ogata, et al., 1995, The centenary of the Omori formula for a decay law of aftershock activity: Journal of Physics of the Earth, **43**, 1–33.

Von Neumann, J., and A. W. Burks, 1996, Theory of self-reproducing automata: University of Illinois Press Urbana.

Warpinski, N., S. Wolhart, C. Wright, et al., 2001, Analysis and prediction of microseismicity induced by hydraulic fracturing: Presented at the SPE Annual Technical Conference and Exhibition, Society of Petroleum Engineers.

Wolfram, S., 1983, Statistical mechanics of cellular automata: Reviews of modern physics, **55**, 601.

Xia, J., H. Gould, W. Klein, and J. Rundle, 2005, Simulation of the Burridge-Knopoff model of earthquakes with variable range stress transfer: Physical review letters, **95**, 248501.

Xia, J., H. Gould, W. Klein, and J. B. Rundle, 2008, Near-mean-field behavior in the generalized Burridge-Knopoff earthquake model with variable-range stress transfer: Physical Review E, **77**, 031132.

Yamanaka, Y., and M. Kikuchi, 2004, Asperity map along the subduction zone in northeastern Japan inferred from regional seismic data: Journal of Geophysical Research: Solid Earth, **109**, B07207.